Downconversion for Solar Cells with Lanthanide Ion Couples

Cover photograph taken by Paul Dekkers near the hut of the Iceland Glaciological Society at Jökulheimar, Iceland (64°18’35.3” north, 18°14’20.3” west).
Cover layout by Wouter Aarts.

DOWNCONVERSION FOR SOLAR CELLS WITH LANTHANIDE ION COUPLES

DOWNCONVERSIE VOOR ZONNECELLEN MET PAREN VAN LANTHANIDE IONEN

(met een samenvatting in het Nederlands)

Proefschrift

ter verkrijging van de graad van doctor aan de Universiteit Utrecht op gezag van de rector magnificus, prof.dr. J.C. Stoof, ingevolge het besluit van het college voor promoties in het openbaar te verdedigen op woensdag 11 november 2009 des middags te 12.45 uur

door

Linda Aarts

geboren op 16 september 1982 te Leiden

Promotor: Prof.dr. A. Meijerink

The work described in this thesis is part of the Joint Solar Programme (JSP) of the Stichting voor Fundamenteel Onderzoek der Materie (FOM), which is supported financially by Nederlandse Organisatie voor Wetenschappelijk Onderzoek (NWO). The JSP is cofinanced by Gebied Chemische Wetenschappen of NWO and Stichting Shell Research.

ISBN 978-90-393-5169-7

Contents

1

Introduction and theory

1.1 Introduction

Over the past decades the demand for energy has increased substantially. The rate of energy consumption is projected to double in 2050 compared to worldwide energy consumption rates in 2001 [1]. The most commonly used energy sources are fossil fuels, but there are two problems with these energy sources. On one hand the resources of oil, coal and natural gas are depleted rapidly. On the other hand the use of fossil fuels has a large effect on the environment and climate by the emission of greenhouse gasses and other pollutants. Sustainable energy sources such as geothermal power, wind turbines and solar cells are already being used. From the various sustainable energy sources solar energy seems the most promising: the sun provides the earth with more energy in one hour (43 EJ) than the present energy consumption on the planet in one year (41 EJ) [1]. The production of sustainable energy by direct conversion of energy radiated from the sun into usable forms like heat or electricity is expected to gain importance because it may be the only renewable source capable of generating sufficient energy to meet the long-term worldwide energy demand [1, 2]. Utilization of solar energy requires effective means of capture and conversion of solar radiation, and storage of the acquired energy [1].

There are several ways to harvest energy from the sun. Solar thermal systems use heat from sunlight, e.g. for making hot water. Sunlight can also be converted into electricity, either by Concentrating Solar Power (CSP) or with solar cells (photovoltaics, PV). CSP systems use lenses or mirrors and tracking systems to focus a large area of sunlight into a small beam. The concentrated light is used to heat a fluid, which is then used as a heat source for a conventional power plant. The capacity of photovoltaic cells to convert sunlight directly into electricity makes them prime candidates for the effective large-scale capture and conversion of solar energy. Solar cells are also useful in places where there is no electricity grid available and can be integrated into existing structures (e.g. on roofs of buildings and houses). At present the contribution of photovoltaic energy is limited due to its relatively high cost per kilowatt-hour [3]. A reduction in price may be achieved by either lowering the production cost or increasing the conversion efficiency.

1.2 Loss mechanisms in solar cells

State-of-the-art commercial single-junction crystalline and polycrystalline Si solar cells dominate the photovoltaic market [4, 5] and crystalline Si wafer cells typically have energy efficiencies around 15% [3]. Conventional solar cells consist of one layer

of n-type and one layer of p-type semiconductor. Upon absorbing a photon above the energy band-gap (E_g) of the absorbing semiconductor material a single electron-hole ($e-h$) pair is generated. The electrons that are excited into the conduction band flow to the n-type side, and the holes in the valence band flow in the opposite direction, eventually resulting in an electrical current in the external circuit [6]. Fig. 1.1 is a schematic diagram showing the loss mechanisms that limit the efficiency of single-junction solar cells. The most significant loss mechanisms in solar cells are those due to relaxation of 'hot' charge carriers that are created upon absorption of a high energy photon (process ① in Fig. 1.1) and transmission of photons with energies below the bandgap of the semiconductor material (process ② in Fig. 1.1). The excess energy of high energy photons is rapidly dissipated as heat by thermalization of the electron and hole to the edges of the conduction band and valence band. These losses are known as thermalization losses. Especially in solar cells based on semiconductors with a small bandgap, these losses are substantial. The transmission losses arise from the fact that photons with an energy smaller than the band-gap of silicon can not be absorbed, and are therefore not converted to electricity. Transmission losses contribute especially to the losses for wider bandgap solar cells, simply because a large part of the solar spectrum cannot be absorbed [7]. Process ③ shows recombination of $e-h$ pairs, and this loss process can be minimized through maintaining high minority carrier lifetimes in the semiconductor material. The theoretical maximum efficiency of a silicon solar cell with a band-gap of 1.1 eV was calculated to be 30% by Schockley and Queisser [8]. The largest part of the 70% energy loss is related to processes ① and ②, and is known as the spectral mismatch. The detailed balance model used by Shockley and Queisser assumes that all recombination losses are radiative (i.e., no non-radiative recombination losses), and includes the voltage drops across the contacts and p-n junction (depicted by ④ and ⑤ in Fig. 1.1).

There are two ways to reduce the losses that are caused by the spectral mismatch: adapt the solar cell to better use the solar spectrum or adapt the solar spectrum to better match the solar cell absorption. The first approach has been successfully applied in so-called multi-junction tandem solar cells for which efficiencies over 40% under concentrated solar light have been realized [10]. This is achieved by 'stacking' multiple solar cells made with different semiconductor materials having different band-gaps. Each of the cells will then absorb a different fraction of the solar spectrum [6, 11]. With an infinite number of junctions the theoretical maximum efficiency becomes 68% [12]. Tandem solar cells are costly and are only now becoming cost-competitive for terrestrial concentrated solar cell applications [11].

Other more recently proposed options for adapting solar cells to the solar spectrum include multiple exciton generation (MEG) and space-separated quantum cut-

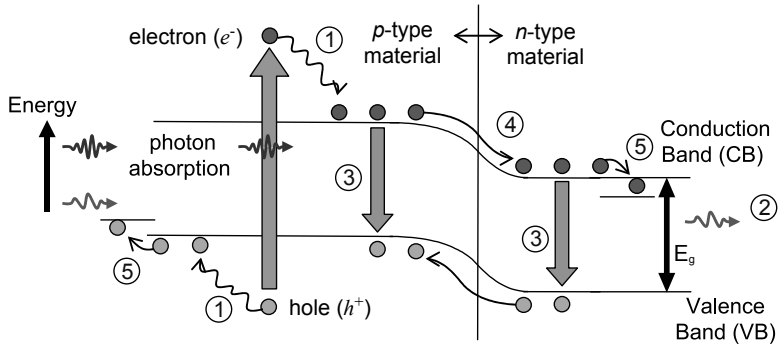

Figure 1.1: Loss processes in a single junction solar cell: ① - lattice thermalisation loss, ② - transmission loss, ③ - recombination loss, ④ - junction loss and ⑤ - contact voltage loss. E_g indicates the bandgap of the solar cell (adapted from ref [7]).

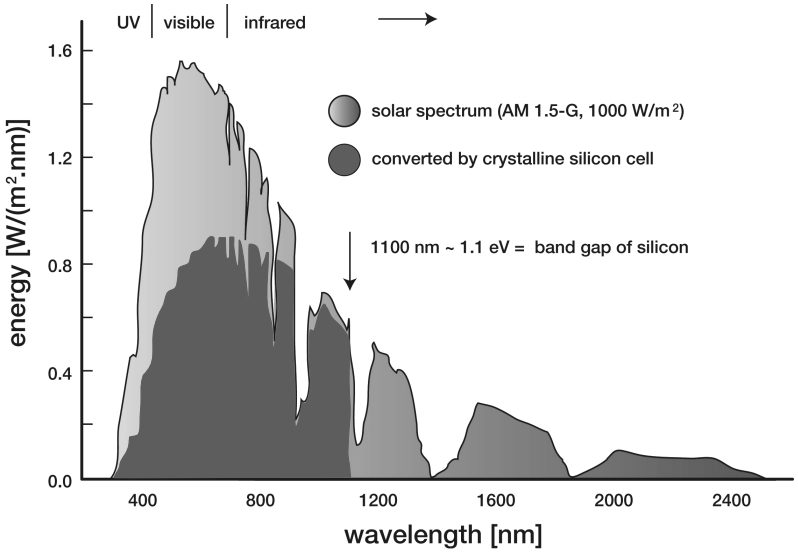

Figure 1.2: The AM1.5G terrestrial solar spectrum showing the fraction of terrestrial sunlight that is currently absorbed and effectively used by a thick crystalline silicon device [9].

ting (SSQC). In both cases multiple $e-h$ pairs are generated after absorption of one high energy photon by the solar cell. MEG has been reported in recent literature for various types of semiconductor nanocrystals ('quantum dots', e.g. CdSe, PbSe, and PbS) [13, 14]. MEG uses the excess energy of charge carriers produced by photons of energy greater than E_g to produce additional charge carriers. It has been estimated that MEG could enhance the efficiency of single junction solar cells to as much as 44% [15, 16]. However, this high gain in efficiency can only be achieved if the MEG efficiency is close to creating one extra electron hole pair for every increase by E_g in the photon energy. Even though $e-h$ pair efficiencies of 700% for photon energies of 8 E_g have been reported, more recent experiments have revealed that the actual efficiencies are much lower [17] and are in fact very similar to the well-known efficiencies for $e-h$ generation in scintillator materials and cathode ray phosphors. For these materials an additional 2.5 E_g in photon energy is required for every extra $e-h$ pair. Such efficiencies for the MEG process will lead to marginal increases in the solar cell efficiency and probably already contributes with similar efficiency in (bulk) semiconductor solar cells for the highest energy (UV) photons [17]. Another concept is space separated quantum cutting (SSQC). SSQC divides an absorbed higher energy photon into two or more lower energy photons through the interaction of two spatially separated neighbouring Si nanocrystals, and has recently been reported to occur in Si nanocrystals [18]. By creating two or more lower energy photons for an high energy photon SSQC could decrease the thermalization losses in solar cells, and multiply the number of charge carriers produced per absorbed (high energy) photon in a solar cell. Further research on SSQC is required to determine the efficiency of charge carrier generation.

The second approach to raise the theoretical efficiency beyond the Shockley-Queisser limit is to adapt the solar spectrum to the solar cell. This can be attained through upconversion (UC) or downconversion (DC). By combining solar cells with a downconverting or upconverting layer energy losses due to spectral mismatch are minimized. A comparative review of both of these methods is given by Strümpel *et al*. [19]. In the case of upconversion, two low-energy photons are 'added up' to give one higher-energy photon [20] and sub-bandgap photons, which are otherwise lost, can be converted into supra-bandgap photons, which can be absorbed [21–23]. Downconversion, which is also known as 'quantum cutting', is the opposite process. One high-energy photon is 'cut' into two lower-energy photons. This process can reduce energy losses due to thermalization of hot charge carriers after the absorption of a high-energy photon. If both lower-energy photons can be absorbed by the solar cell, current doubling is achieved for the region of the solar spectrum that consists of photons with energies exceeding 2 E_g [24, 25]. The final result is similar to MEG

and SSQC. However, in the case of MEG and SSQC multiple $e-h$ pairs are created by one photon after absorption by the solar cell, while for DC they are created by photon-doubling before absorption in the solar cell. Downshifting may also raise the efficiency of the solar cell by converting *one* higher energy photon into *one* lower energy photon that is more efficiently absorbed by the cell [26]. Various means can be used to achieve downshifting, employing quantum dots [27, 28], lanthanide ions [29], and other types of inorganic [30, 31] and organic [32] materials, but this cannot raise the efficiency beyond the Shockley-Queisser limit.

Fig. 1.2 shows the standard terrestrial solar spectrum (Air Mass coefficient AM1.5G) and the fraction of the energy that is currently used by single junction c-Si solar cells. The part that is not used, is available for upconversion and downconversion. In this spectrum, 32% (149 W/m^2) more of the solar spectrum intensity is accessible through downconversion, and 35% (164 W/m^2) of the solar spectrum intensity is acessible through upconversion [7].

For upconversion, a large body of research has already been published. However, this was primarily aimed at the conversion of the output of NIR lasers (800-1000 nm) into visible light, rather than converting longer wavelength NIR into NIR radiation that can be absorbed by crystalline-Si solar cells. An important advantage for upconversion is that an upconversion layer can be applied to the rear of a solar cell without affecting the performance of the device for photons with energies equal to or larger than E_g. Any upconversion of transmitted NIR radiation into the useful wavelength range, which can then generate an additional photocurrent, serves as real gain. By placing a suitable reflector behind the upconversion layer it can be ensured that no usable luminescence escapes out the rear of the solar cell. The major disadvantage of upconversion is that it is a non-linear process which only becomes efficient at high incident power. For an upconversion process of two steps (where two low energy photons are converted to one higher energy photon) the UC light intensity I is related to the incident light intensity I_0 by $I \propto I_0^2$. For three step upconversion, the relation is $I \propto I_0^3$. Contrary to upconversion, downconversion is a linear process and therefore the efficiency is independent of the incident power. This suggests that it will be easier to gain efficiency with downconversion when using unconcentrated sunlight as the illumination source. However, in the case of downconversion the conversion layer is applied on top of the solar cell and a fraction of the luminescence escapes out of the front top surface of the downconversion layer. For luminescent species in a host material with a refractive index of n=1.5, the fraction of the converted photons that escapes out of the conversion layer is 12.7%. Richards thus argues that with front-mounted downconversion, an external quantum efficiency (EQE) of 115% is required for the downconverter just to break even [7]. These losses may be reduced by apply-

ing an anti-reflective coating which specifically reflects the downconverted emission back into the solar cell.

1.3 Modeling of upconversion and downconversion in solar cells

To determine the potential gain in efficiency by applying upconversion or downconversion materials, extensive work has been done in the past decade. Detailed balance models of Trupke *et al.* for upconversion [23] and downconversion [24] are similar to that of Shockley and Queisser (see section 1.2), except for the addition of a spectral conversion layer. In the case of upconversion, the converting layer is mounted beneath a bifacial solar cell. The layer is assumed to be electronically isolated from the solar cell and a perfect reflector is located at the rear surface of the upconverter. The upconverter consists of a material with a band-gap that ideally equals the band-gap energy of the solar cell E_g, and has intermediate levels with an energy E_1 above the valence band edge of the upconverter. The absorption of sub-band-gap photons in the upconverter leads to the generation of $e-h$ pairs via two sequential transitions, first from the valence band into the intermediate level, and then from the intermediate level into the conduction band. The $e-h$ pairs then recombine via the emission of photons with energies at the band gap. The maximum efficiency that can be obtained with this geometry is calculated to be 47.6% for non-concentrated light, with E_g = 2 eV and E_1 = 0.9393 eV. The highest efficiency for a conventional c-Si solar cell (E_g = 1.1 eV) is about 37%. It is clear that the largest gains from upconversion can be obtained for wider bandgap energies E_g, e.g. for Grätzel or amorphous-Si cells, where a larger fraction of the solar spectrum cannot be absorbed.

In the downconversion model [24], the spectral conversion layer is located on the front surface of a conventional single junction solar cell. For each high energy photon absorbed by the spectral converter, two or more lower energy photons are created, which can be absorbed by the solar cell to each generate an $e-h$ pair. This leads to more than on $e-h$ pair being generated in the solar cell for each high energy photon absorbed by the downconverter. The downconverter consists of a material with a band gap $E_{g,converter}$ and contains an intermediate level in the center of the band gap. Radiative transitions take place between the valence band and the conduction band or between one of the bands and the intermediate level. The maximum efficiency for a front-mounted conversion layer is calculated to 38.6% for E_g = 1.1 eV, which is well above the 30.9% Shockley-Queisser limit for a conventional solar cell. The fact that the maximum efficiency for downconversion occurs around E_g = 1.1 eV

makes downconversion a promising option to boost the efficiency for silicon solar cells (E_g = 1.12 eV).

The detailed balance models described provide powerful tools for calculating the thermodynamic limits of cell performance for assumed circumstances. Further insight into the performance of practical converters can be achieved through alternative approaches, such as a recently published Monte Carlo method to model photon conversion for solar cells [33]. The approach employs iterative ray tracing for integrating the photon transport equation at optical frequencies, coupled with non-linear, first-order rate equations describing luminescence of the photon converter. The approach also distinguishes between two sources of light rays: those from the sun, and those from the absorbing luminescence centres of the photon converter. Scattering and reflection of rays by the photon converter and its interfaces are also taken into account. An advantage of the approach is that solar cell enhancement can be estimated as a function of a variety of parameters, such as the luminescent centre concentration, the range of wavelengths that is converted, the cross section for photon capture, the incident photon flux, and the lifetimes of the luminescent emission. This is illustrated through preliminary use of parameters from literature for Er^{3+} doped layers as upconverters or downconverters [33].

The use of semiconductor-like materials with band diagrams having an intermediate level at ½ E_g is not very realistic to achieve efficient up- or downconversion. Lanthanide ions provide the most efficient options for spectral conversion, since they have a multitude of energy levels in the ultraviolet, visible and infrared parts of the spectrum. The properties of the lanthanides will be introduced in sections 1.4-1.6. Recent experimental work on up- and downconversion for solar cells using these ions will be discussed in sections 1.7 and 1.8.

1.4 The lanthanides

The lanthanides are a group of elements found at the bottom of the periodic table. It is the series of elements where the $4f$ inner shell is filled with electrons. They are mostly stable in the trivalent form and the Ln^{3+}-ions have the electronic configuration $[Xe]4f^n5s^25p^6$ where n varies from 0 to 14. The partly filled $4f$ inner shell is responsible for the characteristic optical (and also magnetic) properties of the lanthanides. The number of configurations for n electrons divided over the fourteen $4f$ orbitals is large: $\binom{14}{n}$. All configurations can have different energies, giving rise to energy levels in the UV, visible and (near) infra-red part of the spectrum.

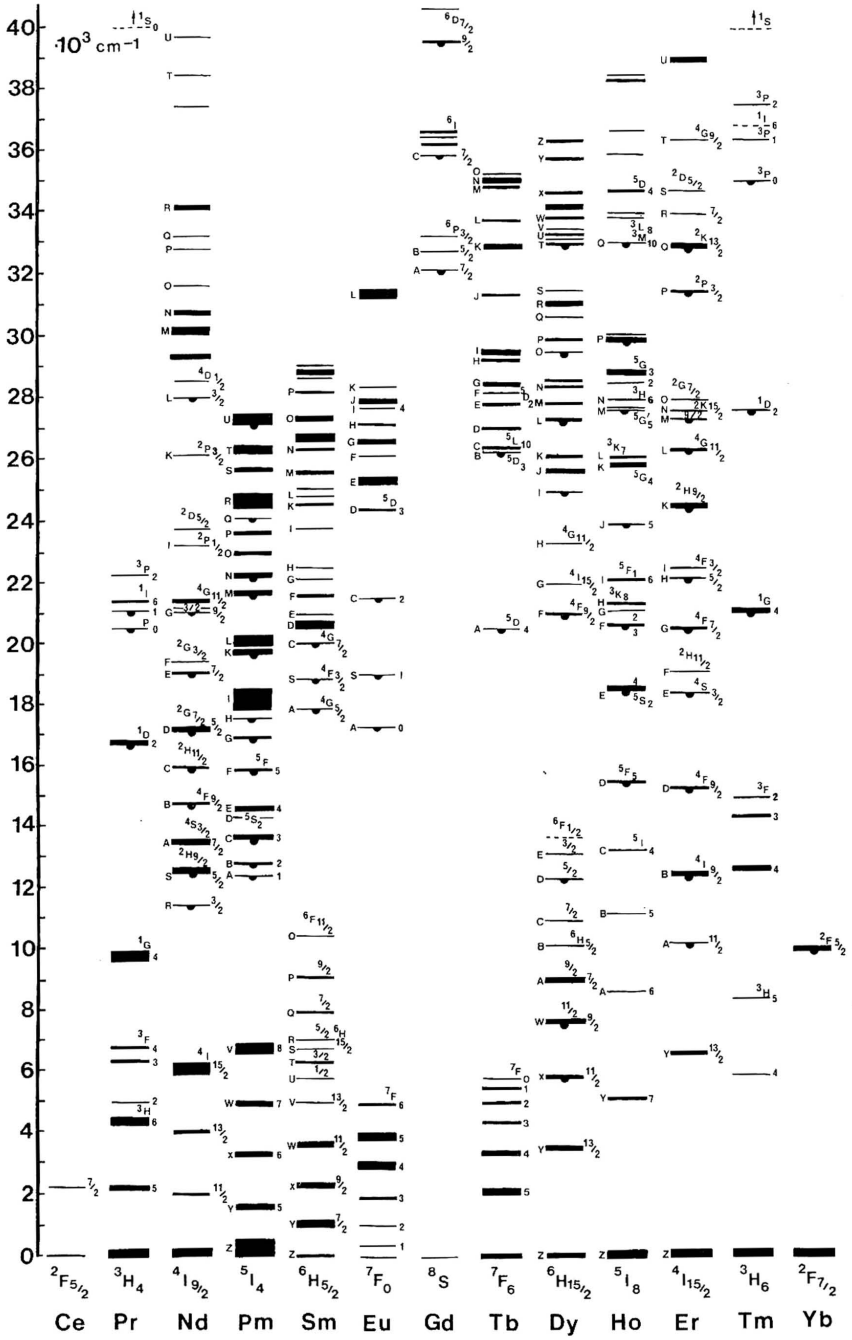

Figure 1.3: Dieke diagram of the observed energy levels of trivalent lanthanide ions [34].

For the free ion the energy levels are labelled by so-called term symbols ($^{2S+1}L_J$) [35]. Fig. 1.3 shows the energy level structure of the $4f^n$ configuration of the trivalent lanthanide ions. This diagram, often referred to as the 'Dieke diagram' (in recognition of Gerard H. Dieke who originally published the diagram) [36, 37], clearly exhibits the rich energy level structure of these ions. This energy level diagram is also representative of the $4f$ energy level structure of these ions when doped into various kinds of crystalline or glassy materials. This is due to the optically active $4f$ orbital being well-shielded from the host environment by the outer filled $5s$ and $5p$ orbitals [35]. Still, the surrounding crystal field induces small Stark splitting of the energy levels, typically of the order of $\sim 10^2$ cm^{-1} [38]. Phonons in the host material mediate non-radiative relaxation between excited energy levels [39].

The peculiar optical properties of the lanthanides were first studied by Becquerel in the beginning of the 20$^{\text{th}}$ century. He observed sharp absorption lines for lanthanide salts at low temperature [40]. This observation was explained by Becquerel, Bethe and Kramers [41–43]: the absorption lines originate from $4f$ intraconfigurational transitions. Since the $4f$ electrons do not participate in bonding, absorption (and emission) lines will be very sharp. According to selection rules intraconfigurational transitions, such as the $4f - 4f$ transitions of the lanthanides, are not allowed as electric dipole transitions since the initial and final state have the same parity. Mixing of opposite parity states into the $4f$ states partly lifts the selection rule, explaining the observed intensities of the $4f - 4f$ transitions.

1.5 Radiative and non-radiative transitions

Almost 50 years ago Judd and Ofelt independently investigated the effect of the mixing of opposite-parity states on the intraconfigurational transition probabilities and selection rules for lanthanide ions [44, 45]. Their results are nowadays known as the Judd-Ofelt theory and with this theory it is possible to calculate the intensities of transitions between the $4f^n$ multiplets. The strength S_{ed} of the electric dipole transitions between initial state a and final state b is defined as:

$$S_{ed} = e^2 \sum_{\lambda=2,4,6} \Omega_\lambda (U^{(\lambda)})^2 \tag{1.1}$$

Ω_λ are the Judd-Ofelt parameters that are host lattice dependent and are influenced by e.g. the strength and symmetry of the odd-parity crystal field. The $U^{(\lambda)}$ terms are referred to as the reduced matrix elements and are independent of the host lattice. The values of $U^{(\lambda)}$ can be calculated for each transition between multiplets. Carnall

et al. have made these calculations and tabulated the reduced matrix elements for all trivalent rare-earth ions [46]. The Judd-Ofelt parameters Ω_λ can be determined by measuring the absorption strength of several transitions from the ground state of the ion in the host lattice. If these absorption strengths have been determined they can be fit to determine Ω_2, Ω_4 and Ω_6 and used to calculate the electric dipole transitions strengths between any two levels of the ion in that specific host lattice.

Some general selection rules for electric dipole transitions between rare-earth ion $4f^n$ states can be obtained from Judd-Ofelt theory [35]. For transitions between two states with term symbol $^{2S+1}L_J$, transitions with

$$\Delta J \leq 6,\ \Delta S = 2 \text{ and } \Delta L \leq 6$$

are allowed, and for a rare earth ion with an even number of electrons

$$\begin{array}{lll} J = 0 \leftrightarrow J' = 0 & & \text{is forbidden} \\ J = 0 \leftrightarrow J' = \text{odd} & & \text{is weak} \\ J = 0 \leftrightarrow J' = 2,4,6 & & \text{is strong} \end{array}$$

Transitions between the $4f$ levels can also be non-radiative, i.e. transitions without the emission of radiation. Non-radiative and radiative transitions compete, which can significantly decrease the quantum efficiency (QE). Energy can be dissipated via the emission of phonons, which are quantized vibrational modes of the lattice surrounding the lanthanide ion. This process is known as multi-phonon emission. When the energy difference ΔE between two energy levels is smaller than 5 times the phonon energy, non-radiative relaxation will dominate over radiative decay [47]. The excitation energy can then be lost by simultaneous emission of a number of phonons. The phonon energies of the highest vibrational frequencies of several different materials are given in Table 1.1.

The temperature dependence of the non-radiative relaxation rate of transitions between the $4f^n$ levels is given by:

$$W(T) = W(0)(n+1)^p \tag{1.2}$$

$W(T)$ is the non-radiative rate at temperature T, p is the number of phonons. When ΔE is the energy difference between the levels and $\hbar\omega$ is the maximum phonon energy of the lattice, the number of phonons involved is given by $\Delta E/\hbar\omega$. The phonon occupation number n is given by:

$$n = \frac{1}{e^{\hbar\omega/kT} - 1} \tag{1.3}$$

Table 1.1: Maximum phonon energy for different types of host lattices.

Material	Phonon Energy (cm^{-1})
Borate	1400
Phosphate	1100
Silicate	1000-1100
Germanate	800-975
Tellurite	600-850
Fluoride	400-600
Oxide	400-600
Chalcogenide	200-300
Chloride	180-250
Bromide	140-190
Iodide	140

The rate $W(0)$ at 0 K is given by [48]:

$$W(0) = \beta \cdot e^{-(\Delta E - 2\hbar\nu_{max})\alpha} \tag{1.4}$$

Where α and β are constants and ν_{max} is the highest vibrational frequency (see also table 1.1) of the surrounding lattice [48].

1.6 Energy transfer

The previous sections have focused on radiative and non-radiative transitions involving single rare-earth ions. Absorption of excitation energy and emission will then occur on the same ion. Up- and downconversion processes can take place within a single type of dopant ion, but also between two or more types of ions co-doped within the same host material, via energy transfer [20, 35, 49]. This section will discuss energy transfer between two (or more) rare-earth ions. There are several different types of energy transfer processes that can occur between two ions, which can be radiative (Fig. 1.4 (a)) or non-radiative (Fig. 1.4 (b-d)). Non-radiative energy transfer can be resonant (Fig. 1.4 (b)), or be aided by emission or absorption of a number of phonons

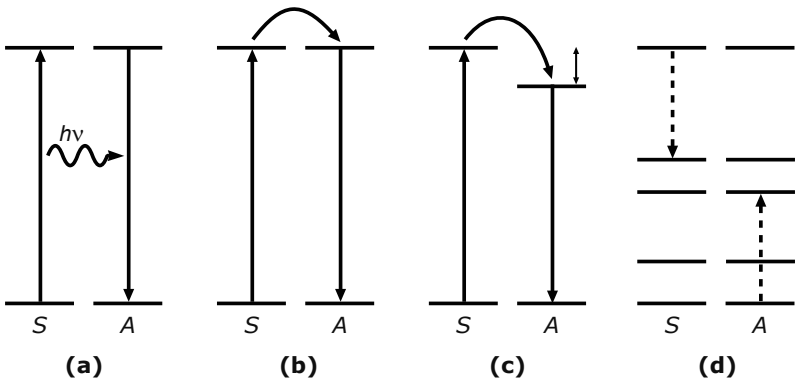

Figure 1.4: Schematic representation of several different energy transfer mechanisms. (a) Radiative energy transfer. (b) Non-radiative resonant energy transfer. (c) Phonon-assisted non-radiative energy transfer. (d) Cross-relaxation.

to compensate for an energy mismatch (Fig. 1.4 (c)), or only part of the energy can be transferred, which is referred to as cross-relaxation (Fig. 1.4 (d)).

The most efficient energy transfer processes involve resonant overlap between the emission band of the donor ion and the absorption band of the acceptor ion [35,48,50]. (Donor and acceptor ions are also referred to in literature as sensitizer and activator ions, respectively. In this thesis, we use the donor/acceptor nomenclature.) The Dieke diagram (Fig. 1.3) shows that the relative positioning of the lanthanide energy levels offers excellent opportunities for the design of materials that can take advantage of resonant energy transfer. Non-resonant energy transfer between co-doped ions is also possible, via a phonon-assisted mechanism or via cooperative or accretive processes, when a resonant intermediate level is not present [51]. Fig. 1.5 displays a sketch of cooperative and accretive forms of upconversion, and Fig. 1.6 shows an analogous sketch for downconversion. The cooperative mechanism in each case involves the mediation of a virtual energy level of the central ion (C in Figs. 1.5 and 1.6), whereas the accretive mechanism involves a virtual energy level for one of the ions with the lower energy excited state (A or B). The predominance of either of these mechanisms over the other is dependent upon the relative geometry between the three energy centres [52, 53]. From a formal theoretical point of view, the downconversion in Fig. 1.6 is the time reversal of the upconversion in Fig. 1.5, which shows *energy-pooling* between two identical donors and an acceptor.

Energy transfer can only occur when two conditions are met. First it is necessary to have spectral overlap between the donor emission and the acceptor absorption. This

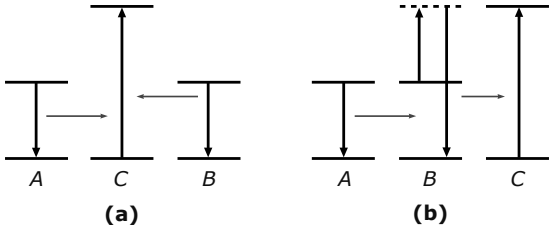

Figure 1.5: Energy level diagrams for three-centre energy pooling: (a) cooperative mechanism, (b) accretive mechanism [51].

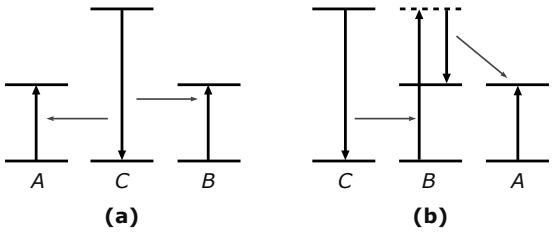

Figure 1.6: Energy level diagrams for downconversion: (a) cooperative mechanism, (b) accretive mechanism [51].

condition is known as the resonance condition. Secondly there should be an interaction between the two ions, this can either be an exchange interaction (wavefunction overlap) or a multipole-multipole interaction [48]. Exchange interaction depends on the wavefunction overlap. Because of this, transfer rates decrease exponentially with the distance. Energy transfer through exchange interaction is therefore a short range process, only active for small (<5 Å) distances between lanthanide ions. Förster discussed the transfer probability for dipole-dipole interactions [20]. He assumed that the interaction is strongest if the electric-dipole transitions for both transitions are allowed. The transfer probability P_{DA} can then be calculated to obey:

$$P_{DA} = \frac{1}{\tau_D}\left(\frac{R_0}{R}\right)^6 \tag{1.5}$$

Here τ_D is the lifetime of the donor excited state, which includes multi-phonon relaxation, and R_0 is the critical distance where transfer of excitation energy and spontaneous deactivation of the donor excited state have the same probability. Since energy transfer depends strongly on distance it is clear that for energy transfer the distance

between two ions should not be too large. To obtain a high emission efficiency of the acceptor it would then seem sensible to make the concentration of acceptors as high as possible, to make sure that each donor has many acceptor neighbors. However, in practice the emission intensity of the acceptor will start to decrease when the acceptor concentration comes above a specific value called the critical concentration. At high concentrations the probability of energy transfer between acceptor ions increases and leads to energy transfer from ion to ion (energy hopping) multiple times before the energy is emitted. During the energy transfer steps a quenching site can be reached, where the energy is lost non-radiatively. This effect is called *concentration quenching*. Generally speaking concentration quenching will start at dopant concentrations higher than a few atomic percent.

1.7 Upconversion mechanisms

As was mentioned in section 1.1, upconversion (UC) is the process where *two* photons with a smaller energy are 'added up' to obtain *one* photon with a high energy [20]. Upconversion has been particularly well-studied for lanthanide and transition metal ions doped into solids, since the discovery of upconversion by Auzel in the 1960s. A review of some of the more recent developments in upconversion spectroscopy is given by Suyver *et al*. [47]. Excellent reviews of upconversion principles have been published by Auzel [20, 54]. Fig. 1.7 gives an overview of the various upconversion mechanisms that are possible. The most efficient process is the mechanism called APTE (Addition de Photon par Transferts d'Energie) or ETU (Energy Transfer Upconversion): two ions of type *I* absorb a photon and give the energy to ion *II* in two steps via an intermediate level on ion *I* (Fig. 1.7 (a)). This can also be described as ground state absorption (GSA) followed by an energy transfer step, written as GSA/ETU. Upconversion on a single ion (Fig. 1.7 (b)) can occur when a second photon is absorbed when the ion is already in the excited state. This mechanism is know as GSA followed by excited state absorption (ESA), and is the second most efficient mechanism. For UC with these two mechanisms it is necessary that the second excitation step of ion *I* is faster than both the radiative and non-radiative decay from the intermediate level. Both of these mechanisms involve real intermediate energy levels. The other four mechanisms shown (Fig. 1.7 (c-f)) involve one or more virtual energy levels, and therefore have lower efficiencies.

Although the relative typical efficiencies of both processes are very different, 10^{-3} for ETU and 10^{-6} for the cooperative process, both processes shows the same dependance on the excitation intensity and donor concentrations [20]. The difference

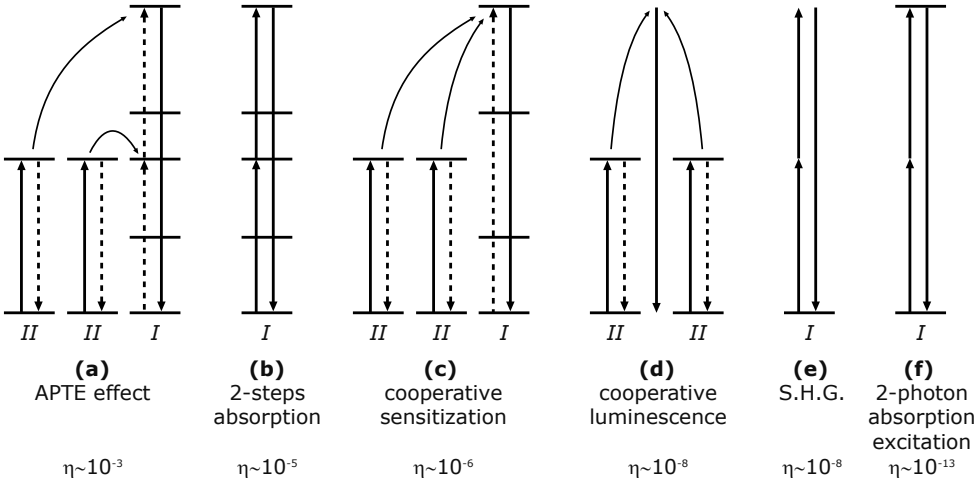

Figure 1.7: Energy level schemes for several different 2-photon upconversion mechanisms, with an indication of quantum efficiencies given in cm^2/W. Solid vertical arrows indicate radiative transitions. Arrows connecting different ions and dashed arrows indicate energy transfer between ions [54].

between these two processes is that for ETU the presence of an intermediate level on the donor ion is required, while in the cooperative process there is a virtual level (the cooperative pair state). The ETU process will be more efficient than cooperative UC, since ETU involves a real intermediate state and has the closest resemblance to the full resonant case (Fig. 1.4 (b)).

Depending on the choice of the upconverting material, UC could in principle be implemented to enhance the efficiency of solar cells with different band gap energies E_g. For crystalline silicon (c-Si), E_g is 1.12 eV (1110 nm) [19]. Amorphous forms of silicon have wider band gap energies, typically up to 1.7 eV [4]. E_g for other semiconductor materials for solar cells also fall in this range, such as Cu_2S (1.2 eV; 1033 nm), GaAs (1.4 eV; 886 nm), and CdTe (1.5 eV; 826 nm) [4, 55]. Organic solar cells may possess a diverse range of values for E_g and typically have an absorption edge not lower than 1.5 eV. The Grätzel cell is based on the use of TiO_2 (E_g = 3.0-3.2 eV; 413-387 nm) [7]. Depending on the choice of dye sensitizer, the photocurrent onset can be reduced in energy to be as low as 1.35 eV (920 nm) [56].

Proof-of-principle experiments have been reported for upconversion with excitation of Er^{3+} at ∼1500 nm in combination with c-Si solar cells, using $NaYF_4$ as a host material for Er^{3+} [21, 22]. For the β-$NaYF_4$ host material the most efficient up-

conversion has been reported to date, in the case of Yb^{3+} sensitized upconversion of excitation at 980 nm (into Yb^{3+}) when Er^{3+} is co-doped with Yb^{3+} [20, 47]. $NaYF_4$ has a low phonon energy (400 cm^{-1}) and the excitation spectrum near 1500 nm is quite broad, stretching from 1480 to 1580 nm. As mentioned above, Er^{3+} upconversion of ~1500 nm photons into NIR radiation that can be absorbed by c-Si is possible by energy transfer between two Er^{3+} neighbors excited to the $^4I_{13/2}$ level. This results in Er^{3+} excited into the higher energy $^4I_{9/2}$ level. To demonstrate the feasibility of combining this upconversion material with a c-Si solar cell, a $NaYF_4$:Er^{3+} (20 mol%) phosphor was mixed into an acrylic medium and adhered to the rear of a bifacial buried contact silicon solar cell. Reflective white paint was used as a reflector at the rear of the solar cell. External quantum efficiencies (EQE) due to upconversion of up to 2.5% were measured (with laser excitation powers of up to 5 mW at 1523 nm). The corresponding upconversion efficiency has been estimated to be up to 12.1% at 6 mW, 1523 nm excitation [21, 22]. Excitation with a quartz halogen lamp resulted in EQE due to upconversion of ~10^{-3} [21]. While this efficiency seems low, it is many orders of magnitude higher than the intrinsic absorption of silicon in this wavelength range. It is expected that improvement of the EQE can be achieved by optimizing the solar cell geometry or by more efficient upconversion materials [47]. The use of chloride host materials could be promising, since these have lower phonon energies. In this way losses in upconversion efficiency due to non-radiative relaxation can be minimized, while maintaining a spectrally wide excitation spectrum of the Er^{3+}-ion [22]. A strong enhancement of the solar cell efficiency could be attained by sensitizing the Er^{3+}-ion with a spectrally broad and efficient absorber, to solve the problem of the relatively weak absorption strength and limited spectral range of absorption of the Er^{3+} $^4I_{15/2} \rightarrow {}^4I_{13/2}$ transition. Research on sensitization in this spectral area is very limited and has not been pursued in relation to spectral upconversion for c-Si solar cells.

Yb^{3+} is often co-doped with other lanthanide ions as a sensitizer for the upconversion process, in order to increase the NIR absorption strength of upconverting lanthanide ions. The Er^{3+}–Yb^{3+} upconversion couple is a particularly famous and well-studied couple, as can be seen from the list of literature reports describing this couple in a number of different host materials [19]. More examples can be found in more recent literature [57–65]. To date, the Er^{3+}–Yb^{3+} couple doped in microcrystalline β-$NaYF_4$ is the most efficient upconversion system known [47]. Sensitized upconversion in the Er^{3+}–Yb^{3+} couple starts with absorption of photons of wavelengths around 980 nm due to the $^2F_{5/2} \rightarrow {}^2F_{7/2}$ transition of Yb^{3+}. The absorption strength for this transitions is relatively high, much higher than for the $^4I_{15/2} \rightarrow {}^4I_{11/2}$ transition of Er^{3+}. The absorbed energy is subsequently transferred to Er^{3+} which is raised to the $^4I_{11/2}$ excited state. A second energy transfer step from Yb^{3+} raises the Er^{3+} to the

$^4F_{7/2}$ level and after relaxation to the $^4S_{3/2}$ level the characteristic green $^4S_{3/2} \rightarrow {}^4I_{15/2}$ emission around 550 nm is observed. This efficiently generated visible luminescence is particularly well-suited for enhancing the efficiency of wider band-gap semiconductor and organic solar cells. The first attempt of integrating spectral conversion for a solar cell was reported by Gibart *et al*. [66], using the Er^{3+}–Yb^{3+} couple in combination with a GaAs solar cell. The upconverting couple was incorporated into vitroceramic material which was coated with a reflective gold mirror on one side, and the vitroceramic was mounted at the rear of the substrate-free solar cell. For 1 mW excitation at 1.39 eV (892 nm), an efficiency of 2.5% was reported, corresponding to the efficiency of the APTE process.

1.8 Downconversion mechanisms

Downconversion (DC) is the process where *one* photon with a high energy is 'cut' to obtain *two* photons with a lower energy (see section 1.1). The idea to obtain quantum yields above 100% by creating multiple photons through 'cutting' a single photon into two lower energy photons was first proposed by Dexter in 1957 [67]. The mechanism involved the simultaneous energy transfer from a donor to two acceptors, each accepting half the energy of the excited donor. It was not until 1974 that experimental evidence for quantum yields above 100% was given for YF_3:Pr^{3+}. The mechanism was not the one proposed by Dexter, but involved two sequential emission steps from the high energy $^1S_0$ level of Pr^{3+} ($^1S_0 \rightarrow {}^1I_6$ followed by relaxation to the $^3P_0$ level and emission of a second visible photon from $^3P_0$) [68, 69]. Later, quantum cutting via two sequential energy transfer steps in the Gd^{3+}–Eu^{3+} couple was discovered and, based on the analogy with the two-step energy transfer process leading to upconversion, it was called 'downconversion' [49]. The aim was to achieve the emission of two visible photons from a single UV photon in order to boost the efficiency of light emitting devices (such as fluorescent tubes). The potential of downconversion for increasing the efficiency of solar cells was realized soon afterwards [24]. The first experimental demonstration of downconversion for solar cells involved the Tb^{3+}–Yb^{3+} couple where quantum cutting was achieved through cooperative energy transfer from Tb^{3+} to two Yb^{3+}-ions, via the same mechanism that was suggested almost 50 years earlier by Dexter [70].

Cutting of one high energy photon to obtain two lower energy photons on a single lanthanide ion is known is cascade emission (Fig. 1.8 (a)) and has been known to occur for Pr^{3+} [69, 71], Tm^{3+} [72] and Gd^{3+} [73]. Downconversion with pairs of lanthanide ions can occur through various pathways, shown in Fig. 1.8 (b-d). For all

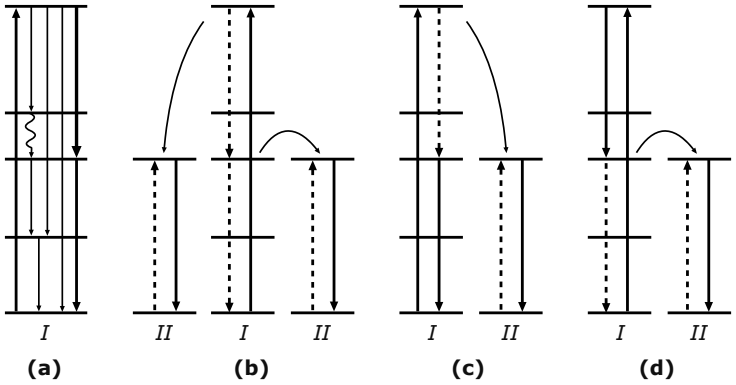

Figure 1.8: Schematic representation of several different downconversion mechanisms. Solid vertical arrows indicate radiative transitions. Arrows connecting different ions and dashed arrows indicate energy transfer between ions. (a) Quantum cutting on one ion via cascade emission. Processes (b-d) occur on two types of ions. As a first step ion *I* is excited into a high energy level. From the high energy level energy transfer will excite the high energy level of the second ion of species *II*. Subsequently two photons will be emitted by two ions *II*, after a second energy transfer step (b), or by both ion *I* and *II* (c). Downconversion can also occur via emission of a photon by ion *I*, followed by energy transfer to an ion of species *II* (d) [49].

three mechanisms ion *I* is first excited into a high energy level. Fig. 1.8 (b) shows the emission of two photons from ion pairs via cross-relaxation between ions *I* and *II* followed by energy transfer from ion *I* to ion *II* and emission from ion *II*. Fig. 1.8 (c,d) show mechanisms involving one energy transfer step between ions *I* and *II*, and emission of a photon by both ions. The downconversion process of the type in Fig. 1.8 (b) has been demonstrated for the phosphor $LiGdF_4:Eu^{3+}$. Upon VUV excitation in the ^6G_J levels of the Gd^{3+}-ion, the energy is transferred to two Eu^{3+}-ions in two energy transfer steps resulting in emission from Eu^{3+}, mainly around 612 nm, with an internal quantum efficiency of about 190% [49, 74]. Internal quantum efficiency refers to the efficiency for photons which are absorbed by the Gd^{3+}-ions. The external quantum efficiency of the system is much lower. Because of the weak absorption of the ^6G_J levels of the Gd^{3+}-ion a significant part of the VUV radiation is not absorbed by Gd^{3+} but by the $LiGdF_4$ host lattice and lost non-radiatively. The external quantum efficiency is therefore much lower and depends strongly on the presence of defect states in the host lattice. Experimental work on $LiGdF_4:Eu^{3+}$ showed external quantum yields of 32% [75]. A second example of quantum cutting through downconversion involves $LiGdF_4:Er^{3+}$, Tb^{3+}, with an internal quantum efficiency of 110% [74, 76, 77]. This system involves UV $4f - 5d$ absorption in Er^{3+}, followed by cross-relaxation with

Gd^{3+}. Subsequently Gd^{3+} transfers its energy to Tb^{3+}, resulting in green emission. The high absorption strength for the $4f^{11} \rightarrow 4f^{10}5d$ transition on Er^{3+} may yield a higher external quantum yield, but this has not been determined experimentally.

UV to VIS quantum cutting is not useful for improving solar cell efficiency, since the (V)UV excitation wavelengths involved are not (or minimally) present in the terrestrial solar spectrum. VIS to near-infrared (NIR) quantum cutting however, is very promising for c-Si solar cells (E_g = 1.12 eV). From the Dieke diagram (Fig. 1.3) it is immediately evident that the energy level structure of Yb^{3+} is ideally suited for use in the downconversion for c-Si solar cells. The Yb^{3+}-ion has a single excited state ($^2F_{5/2}$) approximately 10 000 cm^{-1} above the $^2F_{7/2}$ ground state, corresponding to an emission around 1000 nm. The absence of other energy levels allows Yb^{3+} to exclusively 'pick up' energy packages of 10 000 cm^{-1} from other co-doped lanthanide ions and emit photons at ~1000 nm, which can be absorbed by c-Si. Efficient downconversion using Yb^{3+} via resonant energy transfer requires donor ions with an energy level at about 20 000 cm^{-1} and an intermediate energy level at approximately 10 000 cm^{-1}. Examination of Fig. 1.3 reveals potential ion couples such as Er^{3+}–Yb^{3+}, Nd^{3+}–Yb^{3+}, Ho^{3+}–$Yb^{3+}$and Pr^{3+}–Yb^{3+}. In the absence of an intermediate energy level within the donor ion, cooperative or accretive non-resonant energy transfer is also possible, albeit with much lower efficiency. Inspection of the Dieke diagram shows that Tm^{3+}–Yb^{3+} and Tb^{3+}–Yb^{3+} are potential couples for cooperative or accretive downconversion mechanisms. These approaches for NIR downconversion to enhance the efficiency of c-Si solar cells will form the focus of the rest of this thesis. Based on observations for the probabilities for resonant two-step upconversion of ~10^{-3} and cooperative sensitization of ~10^{-6} [48, 78, 79], it is evident that downconversion via an intermediate level will dominate if the donor has a level around 10 000 cm^{-1} and that efficient downconversion at relatively low Yb^{3+} concentrations can be expected only for the couples Pr^{3+}–Yb^{3+}, Nd^{3+}–Yb^{3+}, Er^{3+}–Yb^{3+} and Ho^{3+}–Yb^{3+}. In this thesis results are described on the possibilities for downconversion using these ion couples.

Downconversion ion couples with Yb^{3+}

The first published experimental work on downconversion with Yb^{3+} was the previously mentioned Tb^{3+}–Yb^{3+} couple in (Y,Yb)PO_4:Tb^{3+} [70]. After excitation into the Tb^{3+} $^5D_4$ level situated around 20 000 cm^{-1}, efficient energy transfer is observed to Yb^{3+}. The Dieke diagram clearly shows that resonant one-step energy transfer is not possible as there is no intermediate level around 10 000 cm^{-1}. To provide evidence that cooperative energy transfer is the operative mechanism, the results of time-resolved luminescence experiments were compared with Monte Carlo simulations based on

theories for phonon-assisted, cooperative, and accretive energy transfer. Analysis of experimental Tb^{3+} decay curves for Yb^{3+} concentrations between 0 and 100% were shown to be in excellent agreement with decay curves from simulation models for cooperative energy transfer. This demonstrated that energy transfer from Tb^{3+} to two neighboring Yb^{3+}-ions occurs via cooperative dipole-dipole interaction. The overall energy transfer efficiency and maximum NIR quantum efficiency were estimated as a function of Yb^{3+} concentration via integration of the normalized Tb^{3+} emission decay curves. A maximum energy transfer efficiency of 88% (and a corresponding maximum NIR quantum efficiency of 188%) was measured. However, this was only achieved through 100% doping of Yb^{3+}. A doping concentration of at least 50% Yb^{3+} was needed to achieve a transfer effiency over 50%. At such high concentrations, concentration quenching of Yb^{3+} becomes very significant, so that the actual measured NIR quantum efficiency is much lower than the maximum limit.

Other reports followed of NIR quantum cutting with the Tb^{3+}–Yb^{3+} couple in several host lattices: in $GdAl_3(BO_3)_4$ [80, 81], $GdBO_3$ [82], Y_2O_3 [83], CaF_2 nanocrystals [84], and lanthanum borogermanate glass [85]. Reports of efficient quantum cutting in other ion couples simultaneously appeared, for Tm^{3+}–Yb^{3+} [81, 86–88] and Pr^{3+}–Yb^{3+} [81, 87, 89]. Estimates for the energy transfer efficiency to Yb^{3+}, and the corresponding NIR quantum efficiency from Yb^{3+} were in nearly every case based on the integration of decay curves, as described by Vergeer *et al.* [70]. This method of estimating the quantum efficiency does not account for concentration quenching of the Yb^{3+} emission. The actual NIR quantum efficiency will always be lower, but it is not trivial to determine absolute or relative quantum yields for infrared emission.

Broad-band sensitization and proof-of-principle experiments

The promising results on downconversion with lanthanides mentioned above do not mean that one can expect implementation of downconversion materials in solar cells in the near future. On the contrary, serious issues need to be addressed before downconversion materials will be applied and it is by no means clear if these problems will be solved. A major limitation in the use of transitions between $4f$ levels of trivalent lanthanide ions is that they are forbidden transitions. The oscillator strengths of $4f-4f$ transitions are typically on the order of 10^{-6}, while dipole-allowed transitions by comparison may have an oscillator strength of up to unity [90]. Therefore the absorption strength of lanthanide $4f-4f$ transitions is very weak and the absorption is limited to narrow lines, preventing absorption of the larger part of the solar spectrum. For efficient downconversion it is crucial that the major part of the high energy region ($h\nu > 2E_g$) of the solar spectrum is converted into two NIR photons. To solve the ab-

sorption problem a third ion is required: a sensitizer which efficiently absorbs all light in the UV and visible part of the spectrum up to ~500 nm and transfers the energy to the downconversion couple, e.g. the $^3P_0$ level of Pr^{3+}. The idea of sensitized lanthanide luminescence is well established and is for example used in fluorescent tubes where the green Tb^{3+} emission is sensitized through the $4f-5d$ absorption of Ce^{3+}. Potential sensitizers for downconversion couples with Yb^{3+} are Eu^{2+} and Ce^{3+} which have strongly absorbing $f-d$ transitions in the desired spectral region.

A second problem that needs to be solved is the issue of concentration quenching. High Yb^{3+} concentrations are needed to achieve complete energy transfer to the Yb^{3+} acceptor ions. At these high concentrations quenching of the emission through energy migration over the Yb^{3+} sublattice (concentration quenching) is a serious issue. A clever choice of host lattice (e.g. inducing clustering by requiring charge compensation) and optimized synthesis conditions (to reduce quenching centers which are reached through energy migration over the Yb^{3+} sublattice) may reduce concentration quenching to acceptable levels.

Finally, if an efficient downconversion couple is developed, the material needs to be incorporated in a transparant layer on top of the solar cell and losses of the emitted downconverted emission need to be reduced by matching of refractive indices of the downconversion layer and/or an anti-reflective coating for the 980 nm Yb^{3+} emission on top of the downconversion layer. Clearly, the road towards implementation is long even when efficient downconversion couples have been found.

1.9 Summary and outline

A large part (60%) of the losses that limit the maximum theoretical efficiency of solar cells to 30% (Shockley-Queisser limit) is caused by the spectral mismatch. The introduction (Chapter 1) describes the potential that lanthanide ions hold to convert photons that are radiated by the sun to more useful wavelengths. The focus is on the use of these ions in upconversion and downconversion schemes, and how these schemes can be utilized to increase solar cell efficiency. Theoretical models show that the Shockley-Queisser limit for the efficiency of a single junction solar cell can be raised from 30% to 40% (using downconversion) or even 50% (using upconversion). Practical realization of these higher efficiencies is however still far away and requires basic research.

In this thesis some lanthanide ion couples are investigated that may be capable of enhancing the efficiency of solar cells through downconversion. Yb^{3+} serves as an ideal acceptor in lanthanide ion couples for downconversion of one visible to two NIR

photons: it has a single excited state, just above the bandgap of c-Si. Examination of the Dieke diagram shows that Er^{3+}–Yb^{3+}, Nd^{3+}–Yb^{3+}, Ho^{3+}–Yb^{3+} and Pr^{3+}–Yb^{3+} are potential couples for efficient downconversion via resonant two-step energy transfer. Tm^{3+}–Yb^{3+} and Tb^{3+}–Yb^{3+} are potential couples for downconversion via cooperative or accretive mechanisms. The choice of host material has a large influence on the efficiency of downconversion, by the way the lanthanide ions are dispersed in a given lattice, as well as by the maximum phonon energy of the lattice.

Chapters 2 and 3 will discuss experiments with the Pr^{3+}–Yb^{3+} downconversion couple in the YF_3 and SrF_2 host lattice. Both in SrF_2 and YF_3 downconversion takes place with this couple. The intrinsic downconversion efficiency is high: for Yb^{3+} concentrations of 10% or higher, the downconversion efficiency is close to 200%. The actual conversion efficiency is however lower, mainly due to concentration quenching and depends on the host lattice. In SrF_2 (where the lanthanide ions form clusters) a visible to NIR conversion efficiency including losses of up to 140% can be obtained, while in YF_3 (where the lanthanide ions are randomly ditributed) the efficiency is well below 100%.

High maximum phonon energies lead to more non-radiative decay. This can be a problem for lanthanide ions that have energy levels just below the starting level for downconversion, such as Er^{3+} and Nd^{3+}. Fast non-radiative decay can prevent downconversion. One example of this is the Er^{3+}–Yb^{3+} couple. Both in fluoride (chapter 4) and chloride (chapter 5) host materials non-radiative relaxation from the starting level for downconversion ($^4F_{7/2}$) to the $^4S_{3/2}$ level via the intermediate $^2H_{11/2}$ level competes with downconversion. For the host with the lowest phonon energy ($CsCdBr_3$, chapter 5), energy transfer from the Er^{3+} $^4F_{7/2}$ level to Yb^{3+} does occur and this shows that low phonon hosts are the most promising candidates for efficient downconversion.

The subsequent chapter shows another example of the influence of the phonon energy of the host lattice on downconversion for the Nd^{3+}–Yb^{3+} couple in YF_3 and $CsCdBr_3$ (chapter 6). In YF_3 ($\hbar\omega$ ~500 cm^{-1}) downconversion is not possible due to fast multi-phonon relaxation from the $^4G_{9/2}$ level to the $^2G_{9/2}$ and $^4F_{3/2}$ levels, while in $CsCdBr_3$ ($\hbar\omega$ 180 cm^{-1}) efficient downconversion takes place.

The last chapter describes preliminary experiments for the Ho^{3+} and Yb^{3+} couple doped into a $LiYF_4$ host lattice. Yb^{3+} emission is observed at the highest (30 %) Yb^{3+} concentration. At this concentration the energy transfer efficiency from Ho^{3+} to Yb^{3+} is 94%, but the visible to NIR conversion efficiency is low.

References

[1] N. Lewis and D. Nocera, *Powering the planet: Chemical challenges in solar energy utilization*, PNAS **103**, 15729 (2006).

[2] O. Morton, *Solar energy: A new day dawning?: Silicon Valley sunrise*, Nature **443**, 19 (2006).

[3] B. van der Zwaan and A. Rabl, *Prospects for PV: a learning curve analysis*, Solar Energy **74**, 19 (2003).

[4] A. Goetzberger, C. Hebling, and H. Schock, *Photovoltaic materials, history, status and outlook*, Materials Science and Engineering: R: Reports **40**, 1 (2003).

[5] D. Bagnall and M. Boreland, *Photovoltaic technologies*, Energy Policy **36**, 4390 (2008).

[6] M. Green, *Photovoltaic principles*, Physica E: Low-dimensional Systems and Nanostructures **14**, 11 (2002).

[7] B. Richards, *Enhancing the performance of silicon solar cells via the application of passive luminescence conversion layers*, Sol. En. Mat. Sol. Cell. **90**, 2329 (2006).

[8] W. Shockley and H. Queisser, *Detailed balance limit of efficiency of p-n junction solar cells*, J. Appl. Phys. **32**, 510 (1961).

[9] http://www.vicphysics.org/documents/events/stav2005/spectrum.JPG.

[10] M. Green, K. Emery, Y. Hishikawa, and W. Warta, *Solar cell efficiency tables (version 33)*, Prog. Photovolt: Res. Appl. **17**, 85 (2009).

[11] F. Dimroth, *High-efficiency solar cells from III-V compound semiconductors*, Physica Status Solidi (c) **3**, 373 (2006).

[12] M. Green, *Third Generation Photovoltaics: Ultra-High Efficiency at Low Cost*, Springer-Verlag, Berlin, Germany, 2003.

[13] R. Schaller, V. Agranovich, and V. Klimov, *High-efficiency carrier multiplication through direct photogeneration of multi-excitons via virtual single-exciton states*, Nature Physics **1**, 189 (2005).

[14] V. Klimov, S. Ivanov, J. Nanda, M. Achermann, I. Bezel, J. McGuire, and A. Piryatinski, *Single-exciton optical gain in semiconductor nanocrystals*, Nature **447**, 441 (2007).

[15] M. Hanna and A. Nozik, *Solar conversion efficiency of photovoltaic and photoelectrolysis cells with carrier multiplication absorbers*, J. Appl. Phys. **100**, 074510 (2006).

[16] A. Nozik, *Quantum dot solar cells*, Physica E: Low-dimensional Systems and Nanostructures **14**, 115 (2002).

[17] M. Trinh, A. Houtepen, J. Schins, T. Hanrath, J. Piris, W. Knulst, A. Goossens, and L. Siebbeles, *In Spite of Recent Doubts Carrier Multiplication Does Occur in PbSe Nanocrystals*, Nano Letters **8**, 1713 (2008).

[18] D. Timmerman, I. Izeddin, P. Stallinga, I. Yassiviech, and T. Gregorkiewicz, *Space-separated quantum cutting with silicon nanocrystals for photovoltaic applications*, Nature Photonics **2**, 105 (2008).

[19] C. Strümpel, M. McCanna, G. Beaucarneb, V. Arkhipovb, A. Slaouic, V. Švrček, C. del Cañizod, and I. Tobias, *Modifying the solar spectrum to enhance silicon solar cell efficiency-An overview of available materials*, Sol. En. Mat. Sol. Cell. **91**, 238 (2007).

[20] F. Auzel, *Upconversion and anti-Stokes processes with f and d ions in solids*, Chem. Rev. **104**, 139 (2004).

[21] A. Shalav, B. Richards, T. Trupke, K. Krämer, and H. Güdel, *Application of $NaYF_4$:Er^{3+} up-converting phophors for enhanced near-infrared silicon solar cell response*, Appl. Phys. Lett. **86**, 013505 (2005).

[22] A. Shalav, B. Richards, and M. Green, *Luminescent layers for enhanced silicon solar cell performance: Up-conversion*, Sol. En. Mat. Sol. Cell. **91**, 829 (2007).

[23] T. Trupke, M. Green, and P. Würfel, *Improving solar cell efficiencies by up-conversion of sub-band-gap light*, J. Appl. Phys. **92**, 4117 (2002).

[24] T. Trupke, M. Green, and P. Würfel, *Improving solar cell efficiency by down-conversion of high-energy photons*, J. Appl. Phys. **92**, 1668 (2002).

[25] B. Richards, *Luminescent layers for enhanced silicon solar cell performance: Down-conversion*, Sol. En. Mat. Sol. Cell. **90**, 1189 (2006).

[26] B. Richards and A. Shalav, *The role of polymers in the luminescence conversion of sunlight for enhanced solar cell performance*, Synth. Met. **154**, 61 (2005).

[27] W. van Sark, A. Meijerink, R. Schropp, J. van Roosmalen, and E. Lysen, *Enhancing solar cell efficiency by using spectral converters*, Sol. En. Mat. Sol. Cell. **87**, 395 (2005).

[28] W. van Sark, *Enhancement of solar cell performance by employing planar spectral converters*, Appl. Phys. Lett. **87**, 151117 (2005).

[29] S. Ye, B. Zhu, Y. Teng, J. Chen, G. Lakshminarayana, G. Qian, and J. Qiu, *Energy transfer between silicon-oxygen-related defects and Yb^{3+} in transparent glass ceramics containing $Ba_2TiSi_2O_8$ nanocrystals*, Appl. Phys. Lett. **93**, 181110 (2008).

[30] M. Peng and L. Wondraczek, *Bismuth-doped oxide glasses as potential solar spectral converters and concentrators*, J. Mater. Chem. **19**, 627 (2009).

[31] V. Švrček, A. Slaoui, and J. Muller, *Silicon nanocrystals as light converter for solar cells*, Thin Solid Films **451-452**, 384 (2004).

[32] G. Maggioni, S. Carturan, M. Tonezzer, M. Buffa, A. Quaranta, E. Negro, and G. Mea, *Porphyrin-containing polyimide films deposited by high vacuum co-evaporation*, Eur. Polym. J. **44**, 3628 (2008).

[33] C. del Cañizo, I. Tobías, J. Pérez-Bedmar, A. Pan, and A. Luque, *Implementation of a Monte Carlo method to model photon conversion for solar cells*, Thin Solid Films , 6757.

[34] G. Dieke, *Spectra and energy levels of rare earth ions in crystals*, Interscience Publishers, New York, 1968.

[35] B. Henderson and G. Imbusch, *Optical Spectroscopy of Inorganic Solids*, Clarendon Press, Oxford, 1989.

[36] G. Dieke and H. Crosswhite, *The Spectra of the Doubly and Triply Ionized Rare Earths*, Appl. Opt. **2**, 675 (1963).

[37] R. Wegh, A. Meijerink, R. Lamminmäki, and H. Jorma, *Extending Dieke's diagram*, J. Lumin. **87-89**, 1002 (2000).

[38] G. Liu, *Spectroscopic proberties of rare earths in optical materials*, pages 1–94, Springer-Verlag, Berlin, 2005.

[39] B. Malkin, *Spectroscopic proberties of rare earths in optical materials*, pages 130–190, Springer-Verlag, Berlin, 2005.

[40] J. Becquerel, Physikalische Zeitschrift **8**, 632 (1908).

[41] J. Becquerel, *Einleitung in eine Theorie der magneto-optischen Erscheinungen in Kristallen*, Zeitschrift fur Physik **58**, 205 (1929).

[42] H. Bethe, *Zur Theorie des Zeemaneffektes an den Salzen der seltenen Erden*, Zeitschrift fur Physik **60**, 218 (1930).

[43] H. Kramers, Proc. Acad. Sci. Amsterdam **32**, 1176 (1929).

[44] B. Judd, *Optical absorption intensities of rare-earth ions*, Phys. Rev. **127**, 750 (1962).

[45] G. Ofelt, *Intensities of crystal spectra of rare-earth ions*, J. Chem. Phys. **37**, 511 (1962).

[46] W. Carnall, H. Crosswhite, and H. Crosswhite, *Energy level structure and transition probabilities of the trivalent lanthanides in LaF_3*, Argonne National Laboratory, Argonne, Illinois, 1997.

[47] J. Suyver, A. Aebischer, D. Biner, P. Gerner, J. Grimm, S. Heer, K. Krämer, C. Reinhard, and H. Güdel, *Novel materials doped with trivalent lanthanides and transition metal ions showing near-infrared to visible photon conversion*, Opt. Mat. **27**, 1111 (2005).

[48] G. Blasse and B. Grabmaier, *Luminescent Materials*, Springer-Verlag, Berlin, Germany, 1994.

[49] R. Wegh, H. Donker, K. Oskam, and A. Meijerink, *Visible quantum cutting in $LiGdF_4:Eu^{3+}$ through downconversion*, Science **283**, 663 (1999).

[50] D. Andrews, *A unified theory of radiative and radiationless molecular energy transfer*, Chem. Phys. **135**, 195 (1989).

[51] D. Andrews and R. Jenkins, *A quantum electrodynamical theory of three-center energy transfer for upconversion and downconversion in rare earth doped materials*, J. Chem. Phys. **114**, 1089 (2001).

[52] R. Jenkins and D. Andrews, *Orientation factors in three-centre energy pooling*, PCCP **2**, 2837 (2000).

[53] R. Jenkins and D. Andrews, *Three-Center Systems for Energy Pooling: Quantum Electrodynamical Theory*, J. Phys. Chem. A **102**, 10834 (1998).

[54] F. Auzel, *Upconversion processes in coupled ion systems*, J. Lumin. **45**, 341 (1990).

[55] X. Mathew, *Band gap of CdTe thin films-The dependence on temperature*, J. Mater. Sci. Lett. **21**, 529 (2002).

[56] M. Grätzel, *Dye-sensitized solar cells*, Journal of Photochemistry and Photobiology C: Photochemistry Reviews **4**, 145 (2003).

[57] M. Hehlen, N. Cockroft, T. Gosnell, and A. Bruce, *Spectroscopic properties of Er^{3+}- and Yb^{3+}-doped soda-lime silicate and aluminosilicate glasses*, Phys. Rev. B. **56**, 9302 (1997).

[58] X. Chen, Y. Nie, W. Du, and N. Sawanobori, *The comparison investigation of direct upconversion sensitization luminescence between ErYb:oxyfluoride glass and vitroceramics*, Opt. Comm. **184**, 289 (2000).

[59] T. Tsuboi, *Upconversion emission in Er^{3+}/Yb^{3+}-codoped YVO_4 crystals*, Phys. Rev. B. **62**, 4200 (2000).

[60] H. Sun, S. Xu, S. Dai, J. Zhang, L. Hu, and Z. Jiang, *Intense frequency upconversion emission of Er^{3+}/Yb^{3+}-codoped natrium-barium-strontium-lead-bismuth glasses*, Solid State Commun. **132**, 193 (2004).

[61] N. Zhuang, X. Hu, S. Gao, B. Zhao, J. Chen, and J. Chen, *Spectral properties and energy transfer of $Yb, Er:GdVO_4$ crystal*, Appl. Phys. B **82**, 607 (2006).

[62] Z. Jingcun, X. Liyan, L. Xiao, G. Kai, L. Guoqing, L. Yulin, Z.and Chao, and F. Baohua, *Spectral Properties and Upconversion Luminescence of Er^{3+}, Yb^{3+}: $BaWO_4$ Crystal*, Journal of Rare Earths **25**, 578 (2007).

[63] M. Liao, L. Hu, Y. Fang, J. Zhang, H. Sun, S. Xu, and L. Zhang, *Upconversion properties of Er3+, Yb3+ and Tm3+ codoped fluorophosphate glasses*, Spectrochim. Acta Part A: Mol. Biomol. Spectrosc. **68**, 531 (2007).

[64] G. Chen, H. Liu, H. Liang, G. Somesfalean, and Z. Zhang, *Upconversion Emission Enhancement in Yb^{3+}/Er^{3+}-Codoped Y_2O_3 Nanocrystals by Tridoping with Li^+ Ions*, J. Phys. Chem. C **112**, 12030 (2008).

[65] B. B. Díaz-Herrera, B. González-Díaz, R. Guerrero-Lemus, C. Hernández-Rodríguez, J. Méndez-Ramos, and V. Rodríguez, *Photoluminescence of porous silicon stain etched and doped with erbium and ytterbium*, Physica E: Low-dimensional Systems and Nanostructures **41**, 525 (2009).

[66] P. Gibart, F. Auzel, J. Guillaumme, and K. Zahraman, *Below band-gap IR response of substrate-free GaAs solar cells using two-photon up-conversion*, Jap. J. Appl. Phys. **35**, 4401 (1996).

[67] D. Dexter, *Possibility of luminescent quantum yields greater than unity*, Phys. Rev. **108**, 630 (1957).

[68] J. Sommerdijk, A. Bril, and A. de Jager, *Two photon luminescence with ultraviolet excitation of trivalent praseodymium*, J. Lumin. **8**, 341 (1974).

[69] W. Piper, J. DeLuca, and F. Ham, *Cascade fluorescent decay in Pr^{3+}-doped fluorides: achievement of a quantum yield greater than unity for emission of visible light*, J. Lumin. **8**, 344 (1974).

[70] P. Vergeer, T. Vlugt, M. Kox, M. den Hertog, J. van der Eerden, and A. Meijerink, *Quantum cutting by cooperative energy transfer in $Yb_xY_{1-x}PO_4:Tb^{3+}$*, Phys. Rev. B. **71**, 014119 (2005).

[71] J. Sommerdijk, A. Bril, and A. de Jager, *Luminescence of Pr^{3+}-activated fluorides*, J. Lumin. **9**, 288 (1974).

[72] R. Rappalardo, *Calculated quantum yields for photon-cascade emission (PCE) for Pr^{3+} and Tm^{3+} in fluoride hosts*, J. Lumin. **14**, 159 (1976).

[73] R. Wegh, H. Donker, A. Meijerink, R. Lamminmäki, and J. Hölsä, *Vacuum-ultraviolet spectroscopy and quantum cutting for Gd^{3+} in $LiYF_4$*, Phys. Rev. B. **56**, 13841 (1997).

[74] R. Wegh, H. Donker, E. van Loef, K. Oskam, and A. Meijerink, *Quantum cutting through down-conversion in rare-earth compounds*, J. Lumin. **87-89**, 1017 (2000).

[75] C. Feldmann, T. Jüstel, C. Ronda, and D. Wiechert, *Quantum efficiency of down-conversion phophor $LiGdF_4 : Eu$*, J. Lumin. **92**, 245 (2001).

[76] K. Oskam, R. Wegh, H. Donker, E. van Loef, and A. Meijerink, *Downconversion: a new route to visible quantum cutting*, J. Alloy Comp. **300-301**, 421 (2000).

[77] R. Wegh, E. van Loef, and A. Meijerink, *Visible quantum cutting via downconversion in $LiGdF_4:Er^{3+},Tb^{3+}$ upon Er^{3+} $4f^{11} \rightarrow 4f^{10}5d$ excitation*, J. Lumin. **90**, 111 (2000).

[78] F. Auzel, *Rare Earth Spectroscopy*, page 502, World Scientific, Singapore, 1985.

[79] F. Auzel, *Materials and devices using double-pumped-phosphors with energy transfer*, Proc. IEEE **61**, 758 (1973).

[80] Q. Zhang, C. Yang, and Y. Pan, *Cooperative quantum cutting in one-dimensional $(Yb_xGd_{1-x})Al_3(BO_3)_4:Tb^{3+}$ nanorods*, Appl. Phys. Lett. **90**, 021107 (2007).

[81] Q. Zhang, G. Yang, and Z. Jiang, *Cooperative downconversion in $GdAl_3(BO_3)_4$: RE^{3+},Yb^{3+} (RE=Pr, Tb, and Tm)*, Appl. Phys. Lett. **91**, 051903 (2007).

[82] Q. Zhang, C. Yang, Z. Jiang, and X. Ji, *Concentration-dependant near-infrared quantum cutting in $GdBO_3:Tb^{3+},Yb^{3+}$ nanophosphors*, Appl. Phys. Lett. **90**, 061914 (2007).

[83] J. Yuan, X. Zeng, J. Zhao, Z. Zhang, H. Chen, and X. Yang, *Energy transfer mechanisms in Tb^{3+},Yb^{3+} codoped Y_2O_3 downconversion phosphor*, J. Phys. D: Appl. Phys. **41**, 105406 (2008).

[84] S. Ye, B. Zhu, J. Chen, J. Luo, and J. Qiu, *Infrared quantum cutting in Tb^{3+},Yb^{3+} codoped transparent glass ceramics containing CaF_2 nanocrystals*, Appl. Phys. Lett. **92**, 141112 (2008).

[85] X. Liu, S. Ye, Y. Qiao, G. Dong, B. Zhu, D. Chen, G. Lakshminarayana, and J. Qiu, *Cooperative downconversion and near-infrared luminescence of Tb^{3+}-Yb^{3+} codoped lanthanum borogermanate glasses*, Appl. Phys. B **96**, 51 (2009).

[86] G. Lakshminarayana, H. Yang, S. Ye, Y. Liu, and J. Qiu, *Co-operative downconversion luminescence in Tm^{3+}/Yb^{3+}:SiO_2-Al_2O_3-LiF-GdF_3 glasses*, J. Phys. D: Appl. Phys. **41**, 175111 (2008).

[87] G. Lakshminarayana and J. Qiu, *Near-infrared quantum cutting in RE^{3+}/Yb^{3+}(RE = Pr, Tb, and Tm): GeO_2-B_2O_3-ZnO-LaF_3 glasses via downconversion*, J. Alloy Comp. **481**, 582 (2009).

[88] S. Ye, B. Zhu, J. Luo, J. Chen, G. Lakshminarayana, and J. Qiu, *Enhanced cooperative quantum cutting in Tm^{3+}-Yb^{3+} codoped glass ceramics containing LaF_3 nanocrystals*, Opt. Express **16**, 8989 (2008).

[89] D. Chen, Y. Wang, Y. Yu, P. Huang, and F. Weng, *Near-infrared quantum cutting in transparent nanostructured glass ceramics*, Opt. Lett. **33**, 1884 (2008).

[90] O. Malta and L. Carlos, *Intensities of $4f$-$4f$ transitions in glass materials*, Quím. Nova **26**, 889 (2003).

2

Near-infrared quantum cutting for photovoltaics through downconversion with the Pr^{3+}–Yb^{3+} couple in SrF_2

Abstract

Spectral conversion of the solar spectrum is a promising avenue to boost the energy efficiency of photovoltaic cells. Energy losses due to thermalization of hot electrons and holes can be minimized through near-infrared (NIR) quantum cutting, whereby one higher energy photon is converted into two NIR photons. Subsequent absorption of both NIR photons by the solar cell results in current doubling for the high energy part of the solar spectrum. Lanthanide ions are the prime candidates to realize efficient quantum cutting. In this chapter evidence is presented for a close to 200% quantum cutting efficiency of visible photons into NIR photons in SrF_2:Pr^{3+}, Yb^{3+} through resonant two step energy transfer. An actual conversion efficiency of visible photons into NIR photons up to 140% is found in SrF_2:Pr^{3+}(0.1%) co-doped with 5% Yb^{3+}, while higher efficiencies may be realized by reducing loss mechanisms for the NIR emission.

2.1 Introduction

Sustainable energy production based on direct conversion of the energy radiated by the sun into useable forms of energy is expected to gain importance since it may be the only source capable of generating sufficient energy to meet the long-term energy demand world-wide [1]. The capacity to convert sunlight into electricity makes photovoltaic cells prime candidates for this task but at present the contribution of photovoltaic energy is limited due to the relatively high cost per kWh [2]. A reduction in cost price can be reached by either lowering the production cost or by increasing the conversion efficiency. State-of-the-art commercial crystalline Si (c-Si) solar cells dominate the market and have energy efficiencies around 15% [2]. The main energy losses (over 70%) are related to the spectral mismatch of incident solar photon energies to the energy gap (E_g) of a solar cell [3]. Solar cells generate a single electron-hole pair upon absorbing a photon above the bandgap energy [4]. Photons with energies lower than the bandgap are not absorbed while for photons with energies exceeding the bandgap, the excess energy is lost as heat during fast thermalization of the 'hot' charge carriers. Taking these energy losses into account, the maximum energy efficiency that can be reached is known as the Shockley-Queisser limit [5]. For the solar spectrum, the limit is 30% for a solar cell with a 1.1 eV bandgap (close to that for c-Si).

To increase the efficiency beyond the Shockley-Queisser limit, two general approaches can be distinguished: adapt the solar cell or adapt the solar spectrum. A suc-

cessful (but costly) demonstration of the first approach is the tandem solar cell, where efficiencies up to 40% can be achieved by combining multiple semiconductor materials [4,6]. Other options may be efficient multiple-exciton generation (MEG), recently reported for various semiconductor nanocrystals (e.g. CdSe, PbSe and PbS) [7, 8], or space-separated quantum cutting (SSQC), recently reported for silicon nanocrystals [9].

The second approach has received less attention. Two methods are capable of reducing spectral mismatch losses by adapting the solar spectrum: upconversion and downconversion. In the case of upconversion, two low energy (infrared) photons are 'added up' to give one higher energy photon [10], thus converting sub-band-gap photons, that are otherwise lost, into supra-bandgap photons that can be absorbed [11,12]. The opposite process, downconversion, is defined as the 'cutting' of one high energy photon into two lower energy photons. This process can reduce energy losses related to thermalization of hot charge carriers after absorption of a high energy photon. By cutting one high energy photon into two low energy photons that can both be absorbed by the solar cell, current doubling is obtained for the higher energy part of the solar spectrum (consisting of photons with energies exceeding 2 E_g) [13, 14]. The result is similar to MEG and SSQC. However, rather than creating multiple excitons in the solar cell, multiple excitons are created through photon-doubling prior to absorption in the solar cell.

2.2 Concept

In this chapter the possibilities for efficient downconversion of a single visible or ultraviolet photon into two near infrared (NIR) photons using lanthanide ions are explored. The unique and rich energy level structures of these ions allow for efficient spectral conversion, including up- and downconversion processes mediated by resonant energy transfer between neighboring lanthanide ions [10, 15]. Considering the energy levels of all lanthanides, depicted in the so-called Dieke energy level diagram [16,17], it is immediately evident that the energy level structure of Yb^{3+} is ideally suited to be used in downconversion for c-Si solar cells. The Yb^{3+}-ion has a single excited state (denoted by the term symbol $^2F_{5/2}$) 10 000 cm^{-1} above the $^2F_{7/2}$ ground state, corresponding to emission around 1000 nm. The absence of other energy levels allow Yb^{3+} to exclusively 'pick up' energy packages of 10 000 cm^{-1} from other lanthanide ions and emitting ~1000 nm photons that can be absorbed by c-Si. Efficient downconversion using Yb^{3+} as acceptor requires donor ions with an energy level around 20 000 cm^{-1} and an intermediate level around 10 000 cm^{-1}. Evaluation of the Dieke di-

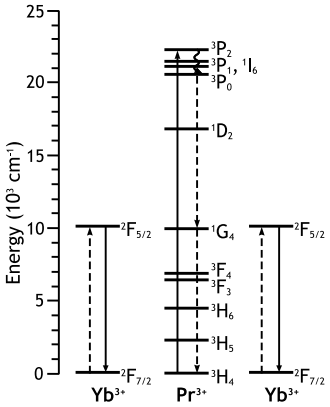

Figure 2.1: Energy levels and quantum cutting mechanism for the Pr^{3+}–Yb^{3+} couple. Two-step energy transfer occurs upon excitation into the ^3P_J (J = 0, 1, 2) and $^1I_6$ levels of Pr^{3+}. A single visible photon absorbed by these levels is thereby converted into two ∼1000 nm photons. Solid arrows are optical transitions, dotted arrows represent non-radiative energy transfer processes, while curved arrows symbolize non-radiative relaxation.

agram [16, 17] reveals that potential couples are Er^{3+}–Yb^{3+}, Nd^{3+}–Yb^{3+}, Ho^{3+}–Yb^{3+} and Pr^{3+}–Yb^{3+}. Here we will focus on the latter couple. In Fig. 2.1 the energy level schemes of Pr^{3+} and Yb^{3+} are schematically shown. Upon excitation of Pr^{3+} in the ^3P_J (J = 0, 1, 2) levels, depopulation of the $^3P_0$ excited state can occur through two sequential resonant energy transfer steps between Pr^{3+} and Yb^{3+} with $^1G_4$ as an intermediate level: Pr^{3+} ($^3P_0 \rightarrow {}^1G_4$), Yb^{3+} ($^2F_{7/2} \rightarrow {}^2F_{5/2}$) followed by Pr^{3+} ($^1G_4 \rightarrow {}^3H_4$), Yb^{3+} ($^2F_{7/2} \rightarrow {}^2F_{5/2}$), resulting in two excited Yb^{3+}-ions and the emission of two NIR photons.

To investigate if this downconversion scheme leads to efficient quantum cutting, SrF_2 was chosen as a host lattice. The choice is motivated by the low phonon energy [18] (suppressing undesired multi-phonon relaxation processes) and the knowledge that lanthanide ions form clusters in SrF_2 as a result of the need for charge compensation when divalent Sr^{2+} is substituted by trivalent Pr^{3+} or Yb^{3+} [19–22]. The clustering enhances the probability that a Pr^{3+}-ion is in close proximity to two or more Yb^{3+} neighbors (required for downconversion) over the probability based on a statistical distribution and this allows for efficient downconversion at low Yb^{3+} concentrations where long range energy transfer (leading to concentration quenching) between Yb^{3+}-ions is not yet prevalent. The tendency of lanthanide ions to cluster in alkaline earth fluorides is well known from experimental [21] and theoretical

work [22] showing that the formation of lanthanide ion clusters (from dimers to hexamers), locally charge compensated by interstitial F^--ions, is energetically favorable and already dominates at low lanthanide concentrations.

2.3 Methods

2.3.1 Synthesis

SrF_2:Pr^{3+} (0.05%, 0.1%, 0.3%), Yb^{3+} (0, 0.2, 1, 2, 3, 5, 9, 17%) crystalline powder samples were prepared by solid state techniques, either via dry mixture of the fluorides (SrF_2, PrF_3, YbF_3) or by co-precipitation of the mixed fluorides from solution using a NH_4F solution. Firing was done in a pure nitrogen atmosphere at temperatures between 750 and 1050 °C in the presence of excess NH_4F. All samples were checked by x-ray powder diffraction and found to be single phase.

2.3.2 Optical spectroscopy

Diffuse reflection spectra were recorded either on a commercial spectrophotometer (Perkin Elmer Lambda 950) with an integrating sphere for diffuse reflection spectroscopy or on a SPEX DM3000F Fluorolog spectrofluorometer using a halogen lamp and by synchronously scanning the excitation and emission monochromator. With both methods similar results were obtained for the relative absorption strengths of the $^3H_4 \rightarrow {}^3P_J$, $^1I_6$ and $^3H_4 \rightarrow {}^1D_2$ transitions. Due to the low Pr^{3+} concentration (0.3% or less) and the forbidden nature of the $f-f$ transitions on Pr^{3+}, the absorption is weak (always less than 10%) and saturation effects do not play a role and allow for a quantitative comparison of the integrated absorption strengths for different peaks. Emission spectra were recorded for excitation with a 450 W Xenon lamp and 0.22 m excitation monochromator of the same SPEX Fluorolog while the emission was detected using a Princeton Instruments 300i CCD detector coupled to a 0.3 m Acton Research monochromator. A radiometrically calibrated DH-2000 halogen lamp from Ocean Optics was used to correct the emission spectra for variation in the instrumental response to allow for an absolute comparison of photon fluxes in different spectral regions. Excitation spectra were recorded with an Edinburgh Instruments FLS920 spectrofluorometer where the infrared emission was detected with a liquid-nitrogen cooled Hamamatsu R5509-72 photomultiplier tube (PMT). Luminescence decay curves were recorded under pulsed excitation with a LPD3000 dye laser (Coumarin 120 dye, tunable between 423-462 nm) pumped by a Lambda Physik

LPX100 excimer laser (XeCl, 308 nm). The Multi Channel Scaling (MCS) option integrated in the FLS920 was used to record the luminescence decay curves, using a R928 PMT, or the IR-sensitive R5509-72 PMT.

2.4 Results

2.4.1 Emission spectra

Emission spectra were recorded upon excitation in the $^3P_2$ level of Pr^{3+} for the various samples. As an example, in Fig. 2.2 emission spectra are shown for three samples doped with 0.1% of Pr^{3+} and different Yb^{3+} concentrations. The samples are prepared and measured under identical conditions. The spectra are corrected for the instrumental response so that the areas of integrated emission peaks represent the total photon flux and can be compared quantitatively. The emission spectrum of SrF_2:Pr^{3+} (0.1%) shows the characteristic $^3P_0$ emission lines of Pr^{3+} and is in agreement with emission spectra in the literature. In the samples with 5 or 17% of Yb^{3+} the $^3P_0$ emission from Pr^{3+} is almost completely quenched, indicating efficient energy transfer to Yb^{3+}. Indeed, a strong emission around 980 nm is observed that is assigned to the $^2F_{5/2} \rightarrow {}^2F_{7/2}$ transition on Yb^{3+}. A good estimate of the conversion efficiency of visible to NIR is obtained by determining the ratio of the integrated emission intensity of the Pr^{3+} luminescence (between 470 and 800 nm) for a sample without Yb^{3+} by the integrated NIR luminescence (between 800 and 1100 nm) for a sample co-doped with Yb^{3+}. Care was taken to conduct the luminescence measurements under identical conditions. The highest conversion efficiency is obtained for samples co-doped with 5 mol% Yb^{3+} and amounts to 140%. For samples with lower Yb^{3+} concentrations, the energy transfer was observed to be incomplete (as evidenced by a significant fraction of $^3P_0$ emission from Pr^{3+}). For the sample with higher Yb^{3+} concentrations the conversion efficiency is lower (<130% for 17% Yb^{3+}) while the Pr^{3+} emission intensity is even lower. This indicates that the $Pr^{3+} \rightarrow Yb^{3+}$ energy transfer is complete at these high concentrations, but the Yb^{3+} emission intensity is reduced as a result of concentration quenching.

2.4.2 Excitation and absorption spectra

Comparison of the total emission intensities for samples doped with only Pr^{3+} and samples co-doped with Pr^{3+} and Yb^{3+} is insightful in order to observe an actual increase in the photon output due to downconversion. On the other hand, the lumines-

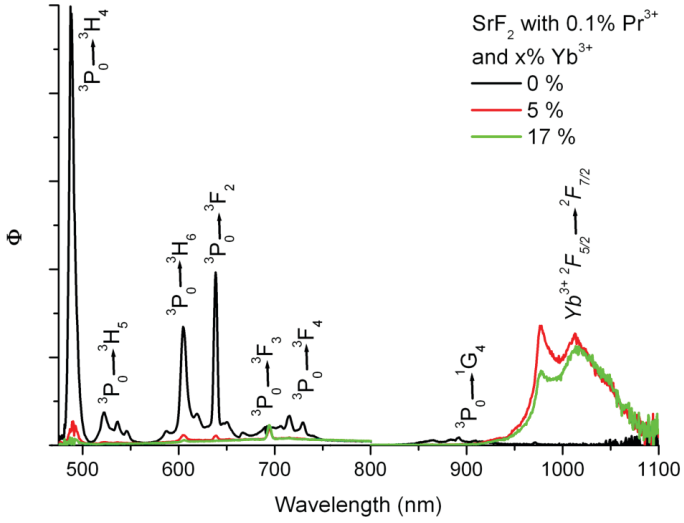

Figure 2.2: Emission spectra for SrF_2:Pr^{3+} (0.1%), Yb^{3+} (x%, x = 0, 5, 17). Emission spectra are recorded under identical conditions for excitation at 441 nm and at 300 K. The spectra are corrected for wavelength-dependent response of the detector system. Φ gives the photon flux per constant wavelength interval.

cence intensities are observed to be strongly dependent on the synthesis conditions; futher, an onset of concentration quenching, even at an Yb^{3+} concentration of 5%, reduces the NIR emission intensity and prevents a more quantitative assessment of the downconversion efficiency. To further confirm the occurrence of, and to estimate the efficiency of downconversion, excitation spectra of the Yb^{3+} emission were recorded and compared with diffuse reflection (absorption) spectra in the region of the $^3H_4 \rightarrow {}^3P_J$, $^1I_6$ (440-500 nm) and $^3H_4 \rightarrow {}^1D_2$ (580-620 nm) transitions. This provides an estimate of the relative number of Yb^{3+}-ions that is excited upon excitation in either the $^3P_0$ level or the $^1D_2$ level and is a measure for the downconversion efficiency. Note that the actual conversion efficiency is lower due to (concentration) quenching processes reducing the Yb^{3+} emission.

Energy transfer to Yb^{3+} is efficient from both the $^3P_0$ and the $^1D_2$ levels, and for samples co-doped with 5% or more Yb^{3+}, almost no Pr^{3+} emission remains. From the $^3P_0$ level a two step energy transfer as depicted in Fig. 2.1 is expected, while from the $^1D_2$ level resonant energy transfer to Yb^{3+} is possible through a one-step Pr^{3+} ($^1D_2 \rightarrow {}^3F_{3,4}$), Yb^{3+}($^2F_{7/2} \rightarrow {}^2F_{5/2}$) process. Note that in the proposed mechanisms

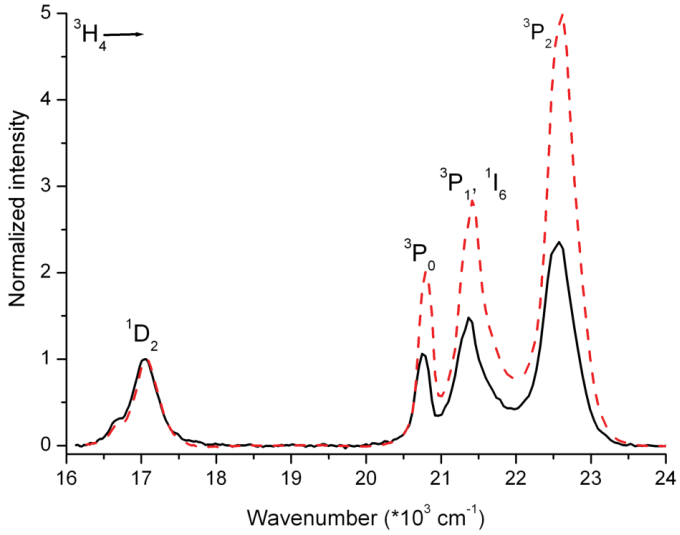

Figure 2.3: Diffuse reflectance and excitation spectra demonstrating quantum cutting. The diffuse reflectance spectrum for SrF_2:Pr^{3+}(0.3%), Yb^{3+}(5%) (solid black line) and excitation spectrum for the same sample monitoring the Yb^{3+} emission at 980 nm (dashed red line) are each normalized to the $^1D_2$ peak. The excitation spectrum has been corrected for wavelength-dependent instrumental response.

absorption of a photon in the ^3P_J or $^1I_6$ level is followed by the emission of two photons around 980 nm, while absorption in $^1D_2$ results in emission of only one 980 nm photon. By comparing the relative absorption strengths of the $^3H_4 \rightarrow {}^3P_J$, $^1I_6$ and $^3H_4 \rightarrow {}^1D_2$ transitions with the corresponding relative photon fluxes in the excitation spectrum, it is immediately clear if downconversion occurs: in case of efficient downconversion the total area of the $^3H_4 \rightarrow {}^3P_J$, $^1I_6$ peaks relative to $^3H_4 \rightarrow {}^1D_2$ peak should be twice as large in the excitation spectrum as in the corresponding diffuse reflectance spectrum.

In Fig. 2.3 the normalized excitation (in red) and absorption (in black) spectra are shown for SrF_2:Pr^{3+}(0.3%), Yb^{3+}(5%). From the diffuse reflection spectra of various samples doped with 5% or 17% Yb^{3+}, the average ratio of integrated absorption in the spectral area for the ^3P_J, $^1I_6$ transitions relative to the $^1D_2$ peak is determined to be 5.5 ± 0.8. The ratio determined for the same transitions in the excitation spectra of the Yb^{3+} emission (which have been corrected for wavelength-dependent instrumental response), again averaged for various samples with Yb^{3+} concentrations of 5 or 17%, yields a value of 9.2 ± 1.5. This ratio is, within the experimental uncertainty, twice the

value of the ratio of the absorption strengths (from diffuse reflectance) and confirms that for every photon absorbed in the ^3P_J, $^1I_6$ levels, two photons in the NIR are generated, i.e. the downconversion from the $^3P_0$ level occurs with an efficiency close to 200%.

2.4.3 Luminescence decay curves

Luminescence decay curves recorded for emission from the $^3P_0$ level provide further insight in the efficiency of the energy transfer process at different Yb^{3+} concentrations. In Fig. 2.4 the decay curves are depicted for SrF_2:Pr^{3+}(0.1%) co-doped with 0, 0.2, 1, 5, and 17% Yb^{3+}. For the SrF_2:Pr^{3+}(0.1%) sample a close to single exponential decay is observed with a decay time of 148 μs. The decay time of 148 μs is due to radiative decay from the $^3P_0$ level and is consistent with literature values for the decay time of the $^3P_0$ emission for locally F^- charge compensated Pr^{3+}-ions [19,20,23]. Addition of Yb^{3+} results in a faster and non-exponential decay which is ascribed to energy transfer from Pr^{3+} to nearby Yb^{3+}-ions. The non-exponential character arises from a variation in the distribution of Yb^{3+} acceptor ions around the Pr^{3+}-ion. This leads to a variety of energy transfer rates for different Pr^{3+}-ions. An estimate of the overall energy transfer efficiency (the fraction of $^3P_0$ excited states that relax through energy transfer rather than radiative decay) can be obtained from the integrals under the normalized decay curves as outlined in reference [24]. From the decay curves in Fig. 2.4 it can be determined that the transfer efficiencies from the $^3P_0$ level are 9% (0.2% Yb^{3+}), 28% (1% Yb^{3+}), 77% (5% Yb^{3+}) and 99% (17% Yb^{3+}).

Decay curves for $^1G_4 \rightarrow {}^3H_5$ emission at 1330 nm upon excitation at 441 nm (not shown) were also recorded for various Yb^{3+} concentrations, and demonstrate that at room temperature there is also energy transfer from the $^1G_4$ level of Pr^{3+} to the $^2F_{5/2}$ level of Yb^{3+}. This is consistent with the observation that the $^1G_4$ emission is weak and with previous work in the literature showing that the energy transfer between the $^1G_4$ state of Pr^{3+} and the $^2F_{5/2}$ state of Yb^{3+} is fast [25,26]. The Pr^{3+} ($^1G_4$) $\rightarrow$ Yb^{3+}($^2F_{5/2}$) transfer efficiency is however temperature dependent since the $^1G_4$ level is at slightly lower energy (~200 cm^{-1}).

2.5 Discussion

Efficient downconversion is observed by the Pr^{3+}–Yb^{3+} couple in SrF_2 at relatively low Yb^{3+} concentrations. Previously we demonstrated downconversion in the Tb^{3+}–Yb^{3+} couple in (Y,Yb)PO_4:Tb^{3+} but this is only efficient at high (> 50%) Yb^{3+} con-

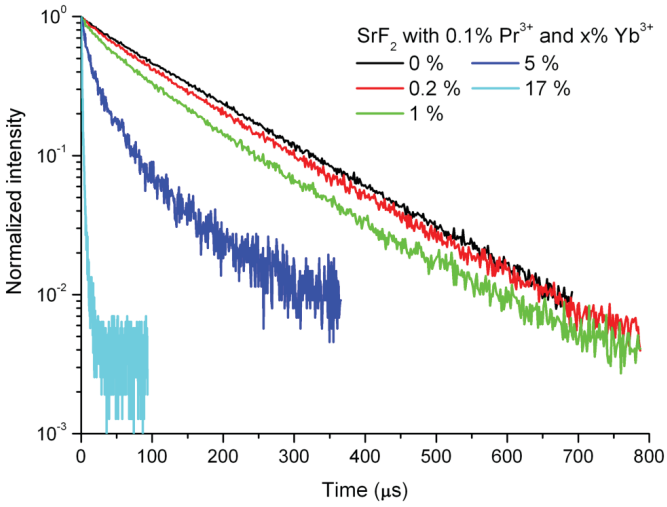

Figure 2.4: Luminescence decay curves of the $^3P_0$ emission in SrF_2:Pr^{3+}(0.1%), Yb^{3+}(x%, x = 0, 0.2, 1, 5, 17). The decay of the Pr^{3+} $^3P_0$ emission at 486 nm ($^3P_0 \rightarrow {}^3H_4$) as a function of time is shown for different Yb^{3+} concentration under pulsed laser excitation at 441 nm.

centrations. The difference is explained by the fact that the Tb^{3+} donor does not have an intermediate energy level at 10 000 cm^{-1}. As a result, energy transfer from the $^5D_4$ level of Tb^{3+} (at 20 000 cm^{-1}) to Yb^{3+} can only proceed through a second-order cooperative energy transfer process (instantaneous energy transfer from Tb^{3+} to two Yb^{3+} acceptors) which was confirmed by analysis of the decay curves [24]. Zhang *et al*. later also reported downconversion by second-order cooperative energy transfer for couples of lanthanide ions in borate host materials [27, 28]. Due to the second-order nature of the process the energy transfer probability from the donor (Tb^{3+}) is relatively low and high efficiencies are only reached at high acceptor (Yb^{3+}) concentrations where the emission intensity is strongly reduced by concentration quenching. This limits the potential for application in solar cells.

The present results show efficient quantum cutting by first order energy transfer for the Pr^{3+}–Yb^{3+} couple. Investigation of the energy level diagrams of Pr^{3+} and Yb^{3+} in Fig. 2.1 reveals that this is not unexpected. The only first order resonant energy transfer process from the $^3P_0$ level of Pr^{3+} to Yb^{3+} is the one depicted in Fig. 2.1. In view of the much higher (typically a factor 10^3) probability of first order energy transfer processes in comparison to second order energy transfer the down-conversion process depicted in Fig. 2.1 will dominate [10]. This explains that for the

Pr^{3+}–Yb^{3+} couple, downconversion of visible photons to NIR photons occurs with an efficiency close to 200% for Yb^{3+} concentrations as low as 5%. Significant concentration quenching is still observed to occur at this level of Yb^{3+} concentration, however. A further complication may arise from the $^1G_4$ level of Pr^{3+} being located at slightly lower energy (~200 cm^{-1}) than the $^2F_{5/2}$ level of Yb^{3+} so that it can effectively trap energy from Yb^{3+} at temperatures below 200 K. Only at elevated temperatures and for multiple Yb^{3+} neighbors can the Yb^{3+} emission dominate over $^1G_4$ emission (for which almost all fluorescence is at longer wavelengths outside the absorption range of c-Si) due to thermally activated energy transfer from $^1G_4$ of Pr^{3+} to surrounding Yb^{3+}-ions.

2.6 Conclusions

In this chapter we have demonstrated efficient quantum cutting of one visible photon into two NIR photons in SrF_2:Pr^{3+}, Yb^{3+}. Comparison of absorption and excitation spectra provides direct evidence that the downconversion efficiency is close to 200%, in agreement with a two-step energy transfer process that can be expected based on the energy level diagrams of Pr^{3+} and Yb^{3+}. This first order energy transfer process is effective at relatively low Yb^{3+} concentrations (5%), where concentration quenching of the Yb^{3+} emission is limited. Comparison of emission spectra, corrected for the instrumental response, for SrF_2:Pr^{3+} (0.1%) and SrF_2:Pr^{3+}(0.1%), Yb^{3+}(5%), reveal an actual conversion efficiency of 140%. Optimization of the synthesis conditions is expected to improve this efficiency by reducing losses due to energy transfer to quenching sites. The next step towards the conversion of the short wavelength part of the solar spectrum will involve the inclusion of a sensitizer for the $^3P_0$ level of Pr^{3+} which is able to absorb efficiently over a broad wavelength range (300-500 nm) and transfer energy to the $^3P_0$ level of Pr^{3+}. In principle, such sensitization can be realized in an efficient and cost-effective manner by the inclusion of a sensitizer ion. The $4f-5d$ luminescence of Ce^{3+}, for example, is often used to sensitize the Tb^{3+} luminescence in phosphors for fluorescent tubes [29]. It has been calculated that (ideal) spectral downconversion can increase the Shockley-Queisser limit for p-n semiconductor solar cells up to 40% for an (optimum) bandgap of 1.05 eV, very close to the bandgap of c-Si [13, 14]. The present results demonstrate the potential of spectral downconversion by lanthanide ions for reducing energy losses in photovoltaic devices and increasing the efficiency of c-Si solar cells to make them more cost-effective.

References

[1] O. Morton, *Solar energy: A new day dawning?: Silicon Valley sunrise*, Nature **443**, 19 (2006).

[2] B. van der Zwaan and A. Rabl, *Prospects for PV: a learning curve analysis*, Solar Energy **74**, 19 (2003).

[3] B. Richards, *Enhancing the performance of silicon solar cells via the application of passive luminescence conversion layers*, Sol. En. Mat. Sol. Cell. **90**, 2329 (2006).

[4] M. Green, *Photovoltaic principles*, Physica E: Low-dimensional Systems and Nanostructures **14**, 11 (2002).

[5] W. Shockley and H. Queisser, *Detailed balance limit of efficiency of p-n junction solar cells*, J. Appl. Phys. **32**, 510 (1961).

[6] S. Kurtz, D. Friedman, J. Geisz, and W. McMahon, *Using MOVPE growth to generate tomorrow's solar electricity*, J. Cryst. Growth **298**, 748 (2007).

[7] R. Schaller, V. Agranovich, and V. Klimov, *High-efficiency carrier multiplication through direct photogeneration of multi-excitons via virtual single-exciton states*, Nature Physics **1**, 189 (2005).

[8] V. Klimov, S. Ivanov, J. Nanda, M. Achermann, I. Bezel, J. McGuire, and A. Piryatinski, *Single-exciton optical gain in semiconductor nanocrystals*, Nature **447**, 441 (2007).

[9] D. Timmerman, I. Izeddin, P. Stallinga, I. Yassiviech, and T. Gregorkiewicz, *Space-separated quantum cutting with silicon nanocrystals for photovoltaic applications*, Nature Photonics **2**, 105 (2008).

[10] F. Auzel, *Upconversion and anti-Stokes processes with f and d ions in solids*, Chem. Rev. **104**, 139 (2004).

[11] A. Shalav, B. Richards, T. Trupke, K. Krämer, and H. Güdel, *Application of $NaYF_4:Er^{3+}$ up-converting phophors for enhanced near-infrared silicon solar cell response*, Appl. Phys. Lett. **86**, 013505 (2005).

[12] T. Trupke, M. Green, and P. Würfel, *Improving solar cell efficiencies by up-conversion of sub-band-gap light*, J. Appl. Phys. **92**, 4117 (2002).

[13] T. Trupke, M. Green, and P. Würfel, *Improving solar cell efficiency by down-conversion of high-energy photons*, J. Appl. Phys. **92**, 1668 (2002).

[14] B. Richards, *Luminescent layers for enhanced silicon solar cell performance: Down-conversion*, Sol. En. Mat. Sol. Cell. **90**, 1189 (2006).

[15] R. Wegh, H. Donker, K. Oskam, and A. Meijerink, *Visible quantum cutting in $LiGdF_4:Eu^{3+}$ through downconversion*, Science **283**, 663 (1999).

[16] G. Dieke, *Spectra and energy levels of rare earth ions in crystals*, Interscience Publishers, New York, 1968.

[17] R. Wegh, A. Meijerink, R. Lamminmäki, and H. Jorma, *Extending Dieke's diagram*, J. Lumin. **87-89**, 1002 (2000).

[18] P. Denham, G. Field, P. Morse, and G. Wilkinson, *Optical and dielectric properties and lattice dynamics of some fluorite structure ionic crystals*, Proc. Roy. Soc. Lond. A **317**, 55 (1970).

[19] R. Reeves, G. Jones, and R. Syme, *Site-selective laser spectroscopy of Pr^{3+} C_{4v} symmetry centers in hydrogenated $CaF_2:Pr^{3+}$ and $SrF_2:Pr^{3+}$ crystals*, Phys. Rev. B. **46**, 5939 (1992).

[20] M. Falin, K. Gerasimov, V. Latypov, and A. Leushin, *Electron paramagnetic resonance and optical spectroscopy of Yb^{3+} ions in SrF_2 and BaF_2; an analysis of distortions of the crystal lattice near Yb^{3+}*, J. Phys. Condens. Matter **15**, 2833 (2003).

[21] P. Bendall, C. Catlow, J. Corish, and P. Jacobs, *Defect aggregation in anion-excess fluorites II. Clusters containing more than two impurity atoms*, J. Solid State Chem. **51**, 159 (1984).

[22] D. Tallant, D. Moore, and J. Wright, *Defect equilibria in fluorite structure crystals*, J. Chem. Phys. **67**, 2897 (1977).

[23] S. Jamison and R. Reeves, *Optical depolarization in CaF_2:RE^{3+} and SrF_2:RE^{3+} C_{4v} centers due to dipole reorientation*, J. Lumin. **66-67**, 169 (1996).

[24] P. Vergeer, T. Vlugt, M. Kox, M. den Hertog, J. van der Eerden, and A. Meijerink, *Quantum cutting by cooperative energy transfer in $Yb_xY_{1-x}PO_4$:Tb^{3+}*, Phys. Rev. B. **71**, 014119 (2005).

[25] Y. Ohishi, T. Kanamari, J. Temmyo, M. Wada, M. Yamada, M. Shimizu, K. Yashino, H. Hanafusa, M. Horiguchi, and S. Takahashi, *Laser diode pumped Pr^{3+}-doped and Pr^{3+}-Yb^{3+}-codoped fluoride fiber amplifiers operating at 1.3 μm*, Electron. Lett. **27**, 1995 (1991).

[26] S. Tanabe, T. Kouda, and T. Hanada, *Excited energy migration and fluorescence decay in Yb-doped and Yb/Pr-codoped tellurite glasses*, Opt. Mat. **12**, 35 (1999).

[27] Q. Zhang, G. Yang, and Z. Jiang, *Cooperative downconversion in $GdAl_3(BO_3)_4$: RE^{3+}, Yb^{3+} (RE=Pr, Tb, and Tm)*, Appl. Phys. Lett. **91**, 051903 (2007).

[28] Q. Zhang, C. Yang, Z. Jiang, and X. Ji, *Concentration-dependant near-infrared quantum cutting in $GdBO_3$:Tb^{3+}, Yb^{3+} nanophosphors*, Appl. Phys. Lett. **90**, 061914 (2007).

[29] G. Blasse and B. Grabmaier, *Luminescent Materials*, Springer-Verlag, Berlin, Germany, 1994.

3

Downconversion for solar cells in $YF_3:Pr^{3+}, Yb^{3+}$

Abstract

Energy losses in solar cells caused by the spectral mismatch can be reduced by adapting the solar spectrum using a downconversion material where one higher energy visible photon is 'cut' into two lower energy near-infrared photons that both can be absorbed by the solar cell. Downconversion with the Pr^{3+}–Yb^{3+} couple in YF_3 is investigated. Based on analysis of luminescence and diffuse reflectance spectra it is evident that two-step energy transfer takes place from the $^3P_0$ level of Pr^{3+} (around 490 nm) exciting two Yb^{3+}-ions to the $^2F_{5/2}$ level giving emission around 980 nm. The transfer efficiency increases with Yb^{3+} concentration and is 86% for YF_3 doped with 0.5% Pr^{3+} and 30% Yb^{3+}. Due to concentration quenching the intensity of emission from Yb^{3+} is strongly reduced and the $^2F_{5/2}$ emission intensity reaches a maximum for the sample with 0.5% Pr^{3+} and 2-5% Yb^{3+} at 300 K. Temperature dependent measurements reveal the role of the Pr^{3+} $^1G_4$ level in the energy transfer between Pr^{3+} and Yb^{3+}. Back-transfer of excitation energy from the Yb^{3+} $^2F_{5/2}$ level to the $^1G_4$ level of Pr^{3+} occurs and quenches the Yb^{3+} emission. The quenching is shown to become more efficient between 4 and 50 K due to faster phonon-assisted energy transfer between the Yb^{3+} donors. Upon raising the temperature from 50 to 300 K, the luminescence lifetime of the Yb^{3+} emission increases again because the small energy difference between the Pr^{3+} $^1G_4$ level and the Yb^{3+} $^2F_{5/2}$ level (~300 cm^{-1}) makes the $^1G_4$ less efficient as a trap for the excitation energy. The present results give insight into factors involved in the concentration quenching in downconversion materials based on the Pr^{3+}–Yb^{3+} couple.

3.1 Introduction

The theoretical maximum energy conversion efficiency of solar cells is 30%; this is known as the Shockley-Queisser limit [1]. The major part of the losses is related to the spectral mismatch: photons with an energy smaller than the bandgap (E_g) cannot be absorbed (sub-bandgap transmission) and a large part of the energy of photons with an energy larger than the bandgap is lost as heat (thermalization losses). The energy losses related to the spectral mismatch can be reduced in two ways. Either the solar cell can be adapted to use the solar spectrum more efficiently, or the solar spectrum can be adapted before it is absorbed by the solar cell. Solar cells can be adapted to make better use of the spectrum by combining multiple semiconductor materials with different bandgaps, each converting a different part of the solar spectrum with high efficiency. This approach has been successfully applied in tandem solar cells and energy efficiencies over 40% have been reported [2].

Alternatively, the solar spectrum can be adapted before it is absorbed by the solar cell. A first option is to add two lower-energy photons (that are otherwise transmitted) to obtain one photon with an energy large enough so that it can be absorbed by the solar cell. This process is known as upconversion (UC) and is well suited for solar cells with a large band-gap where transmission losses dominate. A second option is to split one higher energy photon to obtain two photons with a smaller energy. Each of these photons can subsequently be absorbed by the solar cell and can generate an electron-hole pair. This is known as downconversion (DC) and is most beneficial for solar cells with a smaller band-gap where thermalization losses are the major loss factor. This process is also known as quantum cutting because one photon is 'cut' into two smaller energy photons. Lanthanide ions are very well suited to use for DC or UC because they have a rich energy level structure that allows for efficient spectral conversion. There are many examples of efficient up- and downconversion using lanthanides, either with one type of lanthanide ion or with pairs of lanthanide ions [3,4].

Initial work on downconversion materials was aimed at the conversion of one vacuum UV photon in two visible photons to increase the light yield of VUV phosphors used in plasma display panels and mercury free fluorescent tubes [4–6]. The Gd^{3+}–Eu^{3+} couple in a $LiGdF_4$ host lattice shows efficient VUV to VIS downconversion (internal quantum efficiency of approximately 190%) and Er^{3+}, Gd^{3+} and Tb^{3+} in the same host lattice have an efficiency of 130% [4–6].

The realization that the downconversion concept can also be used to boost the efficiency in solar cells, triggered research on downconversion in lanthanide doped materials. Downconversion of visible photons into NIR photons has been first demonstrated in (Y, Yb)PO_4:Tb^{3+} [7]. After excitation into the $^5D_4$ state of the Tb^{3+}-ion two neighboring Yb^{3+}-ions are excited through a cooperative energy transfer process. The $^5D_4$ level of Tb^{3+}-ions is found at about twice the energy of the Yb^{3+} $^2F_{5/2}$ level and after energy transfer Yb^{3+} emission is observed around 1000 nm. This is just above the band gap of crystalline silicon which makes Yb^{3+} an attractive candidate for DC materials to be used in combination with c-Si solar cells. More recently, cooperative downconversion has also been reported for Tb^{3+}–Yb^{3+} [8,9] and other lanthanide couples, viz. Pr^{3+}–Yb^{3+} [10] and Tm^{3+}–Yb^{3+} [11]. However, it is not clear that the second-order cooperative energy transfer process is the operative mechanism in the Pr^{3+}–Yb^{3+} system as also first-order energy transfer processes are possible and are expected to dominate [12]. Second-order cooperative energy transfer processes have a lower efficiency, making them only efficient at very high Yb^{3+} concentrations where the Yb^{3+} emission is largely quenched through concentration quenching. For more efficient energy transfer, an intermediate level on the donor ion should be used in order

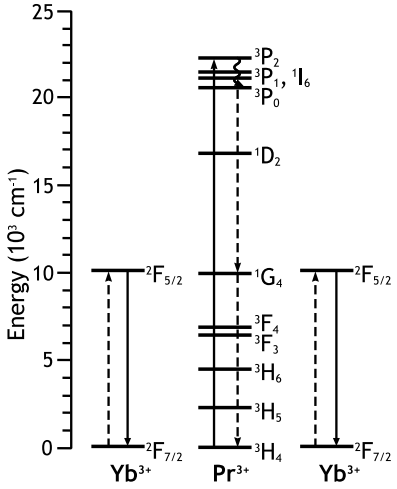

Figure 3.1: Schematic representation of the downconversion mechanism for the Pr^{3+}–Yb^{3+} couple. Pr^{3+} is excited into the ^3P_J state. Part of the energy is donated to Yb^{3+} via cross relaxation: Pr^{3+} ($^3P_0 \rightarrow {}^1G_4$), Yb^{3+} ($^2F_{7/2} \rightarrow {}^2F_{5/2}$), populating the $^2F_{5/2}$ level of Yb^{3+}. In the second step the remaining energy can be transferred to a second Yb^{3+}-ion from the $^1G_4$ level of Pr^{3+}. Both Yb^{3+}-ions can then emit a photon of approximately 1000 nm.

to obtain downconversion through two resonant energy transfer steps.

In chapter 2 evidence for efficient downconversion with the Pr^{3+}–Yb^{3+} couple in SrF_2 was presented (see also Ref. [12]). Fig. 3.1 shows the downconversion scheme via sequential two-step energy transfer. When Pr^{3+} is excited into the $^3P_0$ state part of the energy is donated to Yb^{3+} via cross relaxation: Pr^{3+} ($^3P_0 \rightarrow {}^1G_4$), Yb^{3+} ($^2F_{7/2} \rightarrow {}^2F_{5/2}$), populating the $^2F_{5/2}$ level of Yb^{3+}. In a second step the remaining energy can be transferred to a second Yb^{3+}-ion which can then emit a photon. In SrF_2 the lanthanide ions form clusters [13, 14] due to the need for charge compensation (Pr^{3+} or Yb^{3+} replaces Sr^{2+}). The clustering will influence the energy transfer between Pr^{3+} and Yb^{3+}. In the YF_3 host lattice the lanthanides replace the chemically similar Y^{3+} ions and will therefore be randomly distributed through the lattice. In this chapter we investigate if efficient downconversion is also possible with the Pr^{3+}–Yb^{3+} couple in the YF_3 host lattice and detailed studies on the temperature dependence of the energy transfer processes are reported to gain further insight in the mechanism and kinetics of the energy transfer processes influencing the downconversion efficiency.

3.2 Methods

3.2.1 Synthesis

Crystalline powder samples of YF_3 doped with Pr^{3+} and Yb^{3+} were synthesized via co-precipitation. The samples were prepared by mixing stoichiometric amounts of Y_2O_3, Pr_2O_3 and Yb_2O_3 (purity at least 4N). The powder mixture was dissolved in dilute hydrochloric acid. After adding a solution with an excess of NH_4F (98+%) a fluoride precipitate was formed, which was centrifuge-washed and then dried. The blend was put into an alumina crucible and fired in an oven together with an excess of NH_4F under a nitrogen flow. The samples were first heated to 300°C for two hours (to remove adsorbed water molecules) and then to the reaction temperature of 1000°C for three hours. After the samples had cooled sufficiently they were crushed with a pestle and mortar and x-ray diffraction measurements were performed to check for phase purity.

3.2.2 Measurements

Diffuse reflectance spectra were measured with a Perkin-Elmer Lambda 950 UV/VIS/IR absorption spectrometer. Emission and excitation measurements were performed using an Edinburgh Instruments FLS920 fluorescence spectrometer with a 450 W Xe lamp as excitation source, a 0.3 m excitation double monochromator and two emission monochromators to record emission spectra in the wavelength range 250-800 nm (with a Hamamatsu R928 photomultiplier tube) or in the wavelength range 800-1700 nm (with a liquid nitrogen-cooled Hamamatsu R5509-72 PMT). The Edinburgh fluorescence spectrometer is equipped with an Oxford helium flow cryostat for low temperature measurements. The spectra were not corrected for the instrumental response, unless otherwise indicated.

Luminescence decay curves were recorded using a Lambda Physik LPD3000 tunable dye laser using a Coumarin 120 dye solution (tunable between 423-462 nm) or a Stryryl 14 dye solution (tunable between 904-992 nm). The laser is pumped by a Lambda Physik LPX100 excimer (XeCl) laser. The typical pulse width for the setup is ~20 ns and the repetition rate is 10 Hz. The laser excitation is steered into the sample chamber of the Edinburgh fluorescence spectrometer using a pair of prisms and decay curves are recorded with a multi-channel scaling card.

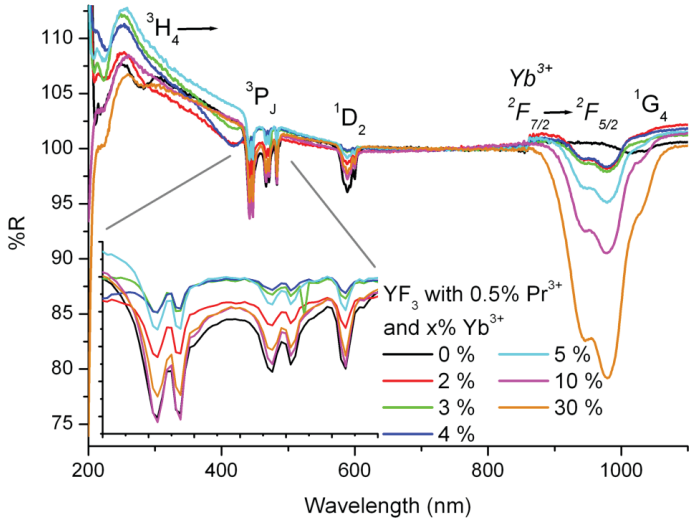

Figure 3.2: Diffuse reflection spectra of YF_3 doped with 0.5% Pr^{3+} and up to 30% Yb^{3+} recorded at 300 K.

3.3 Results and discussion

3.3.1 Characterization

Samples of YF_3 doped with 0.5% Pr^{3+} and 0, 2, 3, 4, 5, 10 and 30% Yb^{3+} and one sample doped with 5% Yb^{3+} and no Pr^{3+} were synthesized. X-ray diffraction measurements for all samples are consistent with the orthorhombic structure of YF_3.

Diffuse reflectance spectra were recorded to confirm if Pr^{3+} and Yb^{3+} were incorporated into the host-lattice. From the diffuse reflectance spectra (Fig. 3.2) it can be concluded that both Pr^{3+} and Yb^{3+} are present in the samples. The absorption strengths for the peaks corresponding to Pr^{3+} absorptions (e.g. the $^3H_4 \rightarrow {}^3P_J$ transitions between 440 and 490 nm) differ from sample to sample, even though in the starting mixture the same amount of Pr^{3+} (0.5 mol%) was present. This shows that the incorporation of Pr^{3+} varied between samples, probably related to the larger ionic radius of Pr^{3+} in comparison to Yb^{3+}. The peak for the Yb^{3+} absorption ($^2F_{7/2} \rightarrow {}^2F_{5/2}$ transition) around 1000 nm does vary in good agreement with the Yb^{3+} concentration.

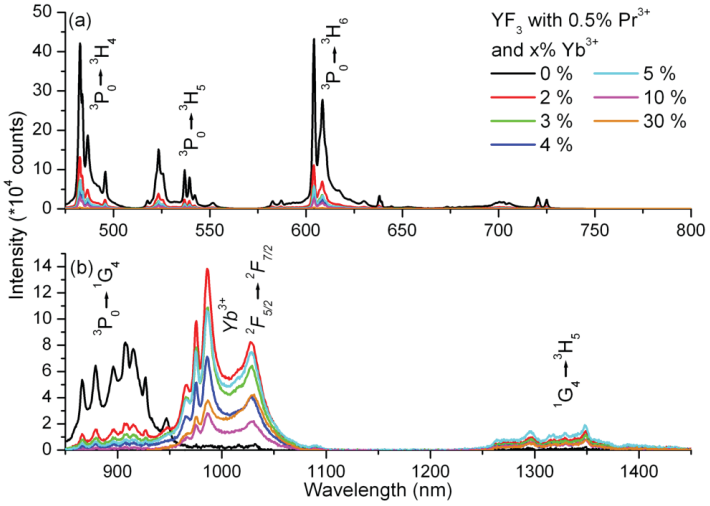

Figure 3.3: Room temperature emission spectra for the visible (a) and infrared (b) part of the spectrum for YF_3:Pr^{3+}(0.5%), Yb^{3+}(0, 2, 3, 4, 5, 10 and 30%). The intensity for the visible and IR part of the spectrum cannot be compared since these were measured with different detectors. The excitation wavelength is 446 nm ($^3P_2$ level).

3.3.2 Room temperature luminescence

In Fig. 3.3 emission spectra are shown for YF_3 doped with 0.5% Pr^{3+} and between 0 and 30 mol% Yb^{3+} after excitation into the Pr^{3+} $^3P_2$ state (446 nm). When no Yb^{3+} is present only emission from the $^3P_0$ level (e.g. $^3P_0 \rightarrow {}^3H_4$ emission at 482 nm and $^3P_0 \rightarrow {}^3H_6$ emission at 604 nm) is observed. The spectrum is similar to previously reported emission spectra for Pr^{3+} in YF_3. Upon excitation in the $^3P_2$ level, fast relaxation to the $^3P_0$ level takes place followed by emission to the various lower energy levels of Pr^{3+}. There is no evidence for $^1D_2$ emission, consistent with the relatively large energy gap between $^3P_0$ and $^1D_2$ (3500 cm^{-1}) and the low maximum phonon energy in YF_3 (500 cm^{-1}) [15] which makes multi-phonon relaxation from $^3P_0$ to $^1D_2$ a very slow process (7 or more phonon emission).

In the infrared region several Pr^{3+} emission bands are observed. The emission band around 900 nm is assigned to the $^3P_0 \rightarrow {}^1G_4$ transition. This populates the $^1G_4$ level and emission from the $^1G_4$ level is observed around 1030 nm (very weak) due to the $^1G_4 \rightarrow {}^3H_4$ transition and around 1320 nm due to the $^1G_4 \rightarrow {}^3H_5$ transition. Note that the reverse transition $^3H_4 \rightarrow {}^1G_4$ can be observed as weak absorption lines around 1020 nm in Fig. 3.2. To understand the intensity distribution for the emission from

Table 3.1: Reduced matrix elements $U^{(\lambda)}$ for transition starting from the Pr^{3+} $^1G_4$ level. The percentages in the bottom row give the $U^{(\lambda)}$ strength for the $^1G_4 \rightarrow {}^3H_4$ transitions relative to the sum of all $U^{(\lambda)}$ values for a given value of λ.

Transition	$U^{(2)}$	$U^{(6)}$	$U^{(6)}$
$^1G_4 \rightarrow {}^3H_4$	0.0014057	0.0063472	0.0220573
$^1G_4 \rightarrow {}^3H_5$	0.0373948	0.0961461	0.4131407
$^1G_4 \rightarrow {}^3H_6$	0.2522574	0.2533723	0.2368336
$^1G_4 \rightarrow {}^3F_2$	0.0000444	0.0158022	0.0058714
$^1G_4 \rightarrow {}^3F_3$	0.0038088	0.0053068	0.0517313
$^1G_4 \rightarrow {}^3F_4$	0.0781891	0.1427101	0.3441897
Sum	0.3731002	0.5196847	1.0738240
Percentage ($^1G_4 \rightarrow {}^3H_4$)	0.38	1.2	2.1

the $^1G_4$ level, Table 3.1 gives the squared reduced matrix elements for the various transitions originating from the $^1G_4$ level. Transition probabilities from the $^1G_4$ level can be determined using the Judd-Ofelt theory [16, 17]. The transition strength S is given by

$$S = \sum_{\lambda=2,4,6} \Omega_\lambda |\langle aJ|U^{(\lambda)}|bJ'\rangle|^2 \tag{3.1}$$

where Ω_λ are the Judd-Ofelt intensity parameters that depend on the host-lattice and the doubly reduced matrix elements of the unit tensor operator $U^{(\lambda)}$ can be calculated for transitions between different multiplets (indicated by aJ and bJ' in Eq. 3.1). In Table 3.1 the squared reduced matrix elements $|\langle aJ|U^{(\lambda)}|bJ'\rangle|$ (abbreviated as $U^{(\lambda)}$) are given for transitions from the $^1G_4$ level of Pr^{3+}. The table shows that, compared to the total $^1G_4$ emission intensity, the contribution of the $^1G_4 \rightarrow {}^3H_4$ transition is 0.38% for $U^{(2)}$, 1.2% for $U^{(4)}$ and 2.1% for $U^{(6)}$. The emission from the $^1G_4$ level will be dominated by transitions to the $^3H_5$, $^3H_6$ and $^3F_4$ levels and the $^1G_4 \rightarrow {}^3H_4$ emission will be weak, for any set of Judd-Ofelt parameters. Note that the two-step emission from the $^3P_0$ level via the $^1G_4$ level is in fact a viable route for quantum cutting of one blue/green photon into two infrared photons, but the efficiency for generating 1000 nm photons is very low. Especially for the second step, the percentage of useful (for c-Si solar cells) IR photons around 1000 nm is low, around 1%, while 99% of the photons will be emitted at wavelengths that are too long to be absorbed by c-Si.

When Yb^{3+} is added as a co-dopant, the intensity of the Pr^{3+} $^3P_0$ emission decreases. Already for 2% of Yb^{3+} a significant drop is observed. Around 1000 nm new emission peaks appear which are assigned to $^2F_{5/2} \rightarrow {}^2F_{7/2}$ transitions on Yb^{3+}. In addition, emission around 1320 nm is present which is assigned to the Pr^{3+} $^1G_4 \rightarrow {}^3H_5$ transition. This shows that there is efficient energy transfer from Pr^{3+} to Yb^{3+}, consistent with the first energy transfer step depicted in Fig. 3.1 resulting in population of the $^2F_{5/2}$ level of Yb^{3+} and the $^1G_4$ level of Pr^{3+}. As the Yb^{3+} concentration is increased the Pr^{3+} $^3P_0$ emission continues to decrease, and it has almost completely disappeared for the sample co-doped with 0.5% Pr^{3+} and 30% Yb^{3+}. Based on the emission spectra shown in Fig. 3.3(b) and diffuse reflectance spectra in Fig. 3.2, it is not surprising that energy transfer is efficient: there is good spectral overlap between the $^3P_0 \rightarrow {}^1G_4$ emission, which extends beyond 950 nm, and the Yb^{3+} absorption band (Fig. 3.2). The intensity of the Yb^{3+} emission reaches a maximum for the sample co-doped with 0.5% Pr^{3+} and 2-5% Yb^{3+} and then starts to decrease. The strong decrease of the Yb^{3+} emission intensity in the samples co-doped with 10 and 30% Yb^{3+} is ascribed to concentration quenching. This commonly observed for concentrated lanthanide compounds. Energy transfer between neighboring Yb^{3+}-ions leads to energy migration to traps and quenching centers and explains the lower Yb^{3+} emission intensity in the compounds with high Yb^{3+} concentrations.

To gain further insight in the energy transfer process between Pr^{3+} and Yb^{3+}, luminescence decay curves were recorded for the $^3P_0$ emission from Pr^{3+} and the $^2F_{5/2}$ emission from Yb^{3+} upon excitation into the Pr^{3+} ^3P_J levels. Fig. 3.4 and 3.5 show room temperature luminescence decay curves of these emissions for YF_3 doped with 0.5% Pr^{3+} and co-doped with 0 to 30% Yb^{3+} for Pr^{3+} $^3P_0$ emission at 604 nm and Yb^{3+} $^2F_{5/2}$ emission at 986 nm. Apart from a small deviation in the beginning of the curve, probably due to energy transfer to defects, a single exponential decay is observed for Pr^{3+} $^3P_0$ emission in YF_3:Pr^{3+}(0.5%) with a decay time of 25 μs (Fig. 3.4). This value is consistent with radiative life times reported for the $^3P_0$ emission in this and similar (fluoride) host lattices [18, 19]. Addition of Yb^{3+} results in a decrease of the lifetime and the decay becomes non-exponential, due to energy transfer from Pr^{3+} to Yb^{3+}. The decay curves recorded for the Pr^{3+} emission for the different concentrations show a clear decrease in the luminescence decay time upon raising the Yb^{3+} concentration. Especially for the highest concentrations (10 and 30% Yb^{3+}) a fast decay is observed, consistent with the large intensity drop observed for these concentrations. The non-exponential character of the decay curves reflects the different distributions of Yb^{3+} acceptor ions around a Pr^{3+}-ion, leading to a variety of energy transfer rates for different Pr^{3+}-ions. Even though the luminescence decay curves of the co-doped samples are not two-exponential, they can be fitted with a two-exponential function

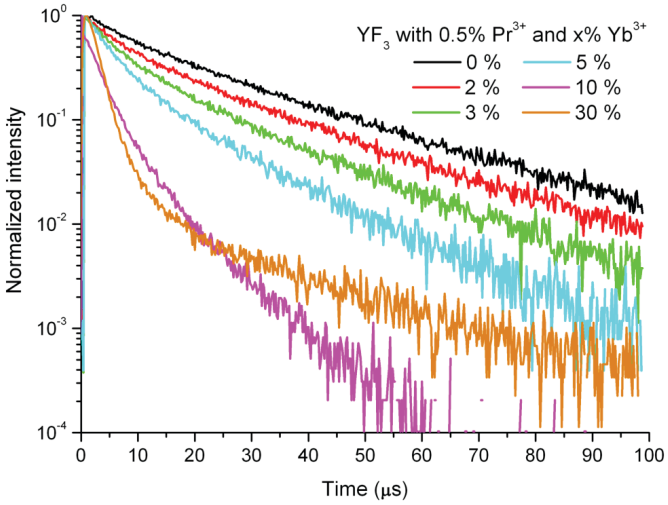

Figure 3.4: Room temperature luminescence decay measurements of the Pr^{3+} $^3P_0$ emission (604 nm) in YF_3:Pr^{3+}(0.5%), Yb^{3+}(0, 2, 3, 5, 10 and 30%) after pulsed excitation into the Pr^{3+} $^3P_2$ level (442 nm).

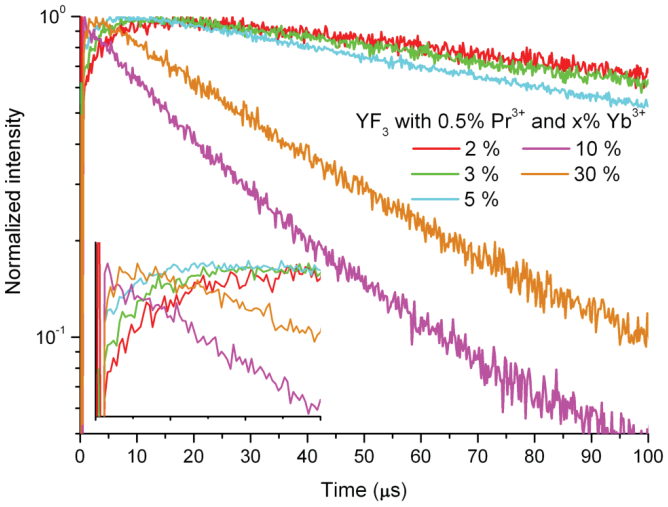

Figure 3.5: Room temperature luminescence decay measurements of Yb^{3+} $^2F_{5/2}$ emission (986 nm) in YF_3:Pr^{3+}(0.5%), Yb^{3+}(2, 3, 5, 10 and 30%) after excitation into the Pr^{3+} $^3P_2$ level (442 nm). The inset shows the build-up in the first 15 μs of the decay curve.

to obtain an estimate of the lifetime of Pr^{3+} $^3P_0$ emission and the efficiency of the energy transfer processes as a function of the Yb^{3+} concentration. The lifetime τ determined for the slower component decreases from 25 μs for the sample without Yb^{3+} to 11 μs for the sample with the highest Yb^{3+} concentration. The decay times determined for the faster component decrease from 6.0 μs for the sample co-doped with 2% Yb^{3+} to 2.6 μs when 30% Yb^{3+} is present in the sample, indicating that energy transfer becomes more efficient at higher Yb^{3+} concentrations. The overall energy transfer efficiency, i.e. the fraction of Pr^{3+}-ions that relax through energy transfer instead of radiative decay, can be obtained from the integrals under the normalized decay curves [7]. From the decay curves in Fig. 3.4 the energy transfer efficiency from the $^3P_0$ level was estimated to be 25, 44, 59, 85 and 86% for co-doping with 2, 3, 5, 10 and 30% Yb^{3+}, respectively. This shows that downconversion is efficient already at relatively low Yb^{3+} concentrations. In comparison with SrF_2:Pr^{3+}, Yb^{3+} the efficiency is however lower: at 5% Yb^{3+} the transfer efficiency was already 77% and at 17% Yb^{3+} a 99% transfer efficiency was observed [12]. The higher transfer efficiency in SrF_2:Pr^{3+}, Yb^{3+} is explained by clustering of the lanthanides

The luminescence decay curves for Yb^{3+} $^2F_{5/2}$ emission in Fig. 3.5 were fitted to a two-exponential function with a feeding term (with characteristic time τ_1) and a decay term (with a decay time τ_2). In this case τ_1 represents the build-up that is visible in the first 15 μs of the decay, and τ_2 is the lifetime of the Yb^{3+} $^2F_{5/2}$ emission. The build-up is caused by feeding of the Yb^{3+} $^2F_{5/2}$ emission by energy transfer from Pr^{3+}. The build-up becomes faster as more Yb^{3+} is added to the sample, decreasing from 5.4 μs for 2% Yb^{3+} to 1.0 μs for 30% Yb^{3+}. These numbers are consistent with the fast lifetime component of the $^3P_0$ emission and confirm that the build-up is due to feeding of Yb^{3+} $^2F_{5/2}$ level by energy transfer from the $^3P_0$ level with transfer rates up to 10^6 s^{-1} for the highest Yb^{3+} concentrations. The lifetime of the Yb^{3+} $^2F_{5/2}$ emission is given by the decay term and decreases from 147 μs to 36 μs when the Yb^{3+} concentration is increased from 2 to 30%. At higher Yb^{3+} concentrations concentration quenching leads to a shorter emission lifetime. The effect of concentration quenching is also observed in emission spectra (Fig. 3.3).

Convincing evidence for the occurrence of downconversion can be obtained from excitation and reflectance spectra. By comparing diffuse reflectance and excitation spectra which are corrected for the instrumental response (Fig. 3.6) the downconversion efficiency can be estimated as outlined in Ref. [12]. The method relies on the fact that downconversion from the $^3P_0$ level leads to excitation of two Yb^{3+}-ions while one-step energy transfer from the $^1D_2$ feeds only one Yb^{3+}-ion. As a result, the ratio of the $^3P_J/^1D_2$ lines is expected to be two times higher in the excitation spectrum in comparison to the diffuse reflection spectrum. Since the energy transfer is complete at

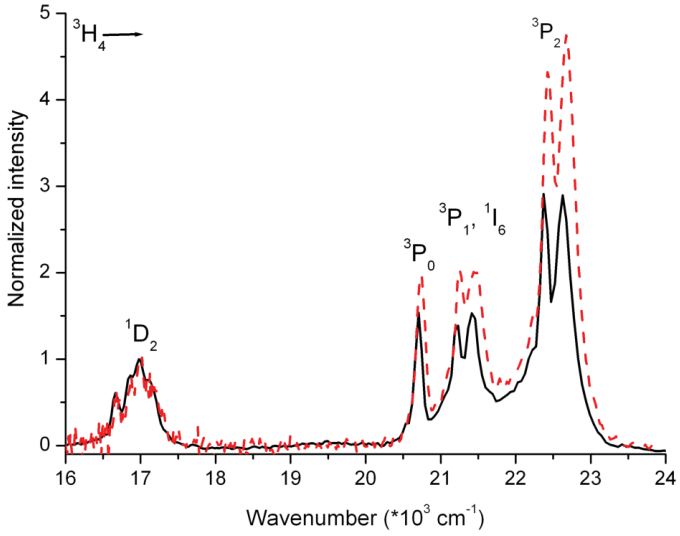

Figure 3.6: Diffuse reflectance (solid black line) and excitation (dotted red line) spectra for YF_3:Pr^{3+}(0.5%), Yb^{3+}(30%), demonstrating that quantum cutting takes place. Both spectra are normalized at the peak of the $^1D_2$ emission (17 000 cm^{-1}). The excitation spectrum monitored Yb^{3+} emission at 980 nm, and was corrected for wavelength-dependent instrument response.

an Yb^{3+} concentration of 30%, this sample was selected for a comparison of the diffuse reflectance and excitation spectra. From the diffuse reflectance spectrum the ratio of the total absorption (integrated spectral area) of the $^3H_4 \rightarrow {}^3P_J$ and $^3H_4 \rightarrow {}^1I_6$ transitions relative to that of the $^3H_4 \rightarrow {}^1D_2$ transition was determined to be 5.5. After correcting the excitation spectrum for wavelength-dependent instrumental response the ratio for the same transitions in the excitation spectrum of the Yb^{3+}emission was 8.9. This ratio is close to twice the value of that of the ratio found from diffuse reflectance, confirming that absorption of a photon into the ^3P_J and $^1I_6$ levels results in excitation of two Yb^{3+}-ions.

3.3.3 Temperature dependent measurements

To obtain a better insight in the energy transfer processes involved in downconversion and concentration quenching in the Pr^{3+}–Yb^{3+} system, temperature dependent luminescence measurements and lifetime measurements were performed between 4 and 300 K. Energy losses related to concentration quenching reduce the overall downcon-

version efficiency and insight in the energy transfer processes can aid in optimizing the luminescence efficiency. An important aspect in the case of the Pr^{3+}–Yb^{3+} downconversion couple is that the Pr^{3+}-ions not only acts as donor (energy transfer from the $^3P_0$ level of Pr^{3+}) but can also trap the excitation energy from Yb^{3+}-ions in the excited $^2F_{5/2}$ state as the lowest energy $^1G_4$ crystal field (CF) component is some 300 cm^{-1} lower in energy than the lowest energy CF component of the $^2F_{5/2}$ state. As discussed above, the reduced matrix elements for the various transitions (Table 3.1) show that the strongest emissions from the $^1G_4$ state are not to the $^3H_4$ ground state, but to the $^3H_5$, $^3H_6$ and $^3F_3$ levels giving emission around 1320, 1840 and 2900 nm, respectively. Clearly, these emissions are not useful for c-Si solar cells. To study the influence of concentration quenching, emission spectra were recorded as a function of temperature under direct excitation into the $^2F_{5/2}$ excited state of Yb^{3+} (986 nm). The emission spectra for some representative temperatures are shown in Fig. 3.7. At 4 K relatively strong and narrow emission lines are observed. Between 4 and 20 K the intensity drops rapidly. Above 50 K the intensity recovers and at room temperature the intensity is similar to that at 4 K. At all temperatures (weak) emission due to the Pr^{3+} $^1G_4 \rightarrow {}^3H_5$ transition can be observed around 1350 nm in addition to the Yb^{3+} emission around 1000 nm, showing that energy back-transfer from Yb^{3+} $^2F_{5/2}$ to the Pr^{3+} $^1G_4$ level takes place. In addition, line broadening is observed due fast phonon-induced dephasing processes at elevated temperatures.

The peculiar temperature dependence can be explained by considering the two temperature regimes (4-50 K and 50-300 K). Upon raising the temperature from 4 to 50 K the energy transfer between neighboring Yb^{3+}-ions increases. Due to small energy differences between the local environment of lanthanide ions, the energy levels are at slightly different energies and resonant energy transfer is not possible. This hampers energy migration and as a result concentration quenching is reduced at 4 K and the $^2F_{5/2}$ emission is relatively strong. Upon raising the temperature, phonon-assisted energy transfer becomes possible and rapid energy migration to traps (including the $^1G_4$ level of Pr^{3+}) occurs, efficiently quenching the $^2F_{5/2}$ emission. When the temperature is raised further, thermally activated back-transfer from the $^1G_4$ level of Pr^{3+} becomes possible and as the temperature is raised, the back-transfer probability increases. The temperature regime where the increase in the Yb^{3+} emission is observed, is consistent with the energy difference between $^1G_4$ and $^2F_{5/2}$ (~300 cm^{-1}).

Support for the explanation for the temperature dependence of the emission intensities comes from temperature dependent luminescence decay curves. Energy migration and transfer of excitation energy from Yb^{3+} to the Pr^{3+} $^1G_4$ level also has an effect on the lifetimes of the Yb^{3+} $^2F_{5/2}$ emission. In Fig. 3.8 luminescence decay curves are shown at various temperatures between 4 and 300 K. The tail of the decay

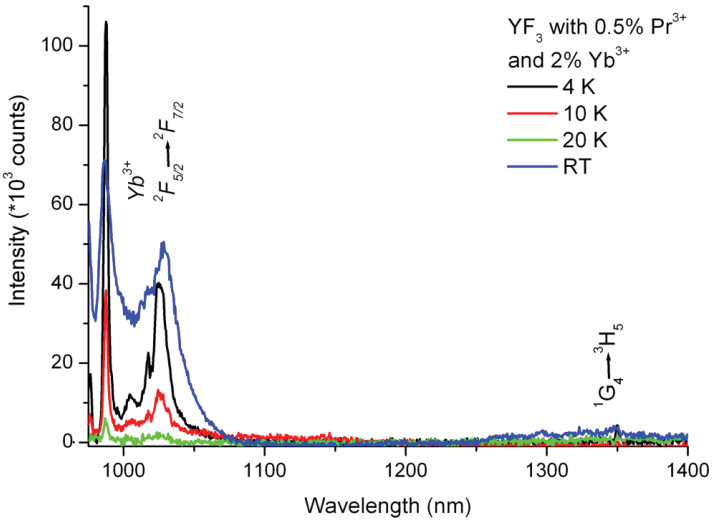

Figure 3.7: Temperature dependent emission spectra for YF_3:Pr^{3+}(0.5%), Yb^{3+}(2%) for excitation into the Yb^{3+} $^2F_{5/2}$ level (950 nm).

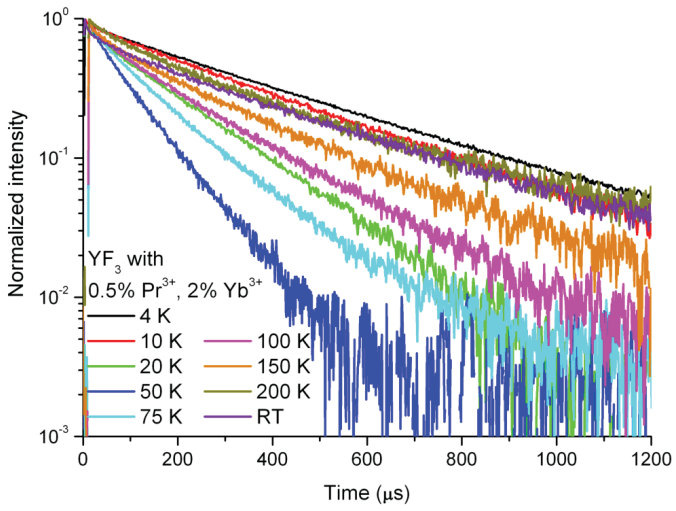

Figure 3.8: Temperature dependent luminescence decay measurements for the Yb^{3+} $^2F_{5/2}$ emission (986 nm) in YF_3:Pr^{3+}(0.5%), Yb^{3+}(2%) after pulsed excitation into the Yb^{3+} $^2F_{5/2}$ level (950 nm).

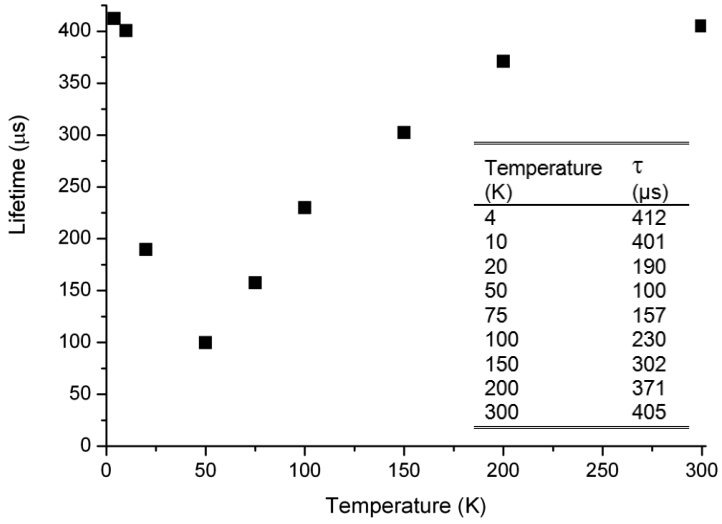

Temperature (K)	τ (μs)
4	412
10	401
20	190
50	100
75	157
100	230
150	302
200	371
300	405

Figure 3.9: Temperature dependence of the luminescence lifetimes deduced from single exponential fitting of the decay measurements of Yb^{3+} $^2F_{5/2}$ emission (986 nm) in $YF_3:Pr^{3+}$(0.5%), Yb^{3+}(2%) after excitation into the Yb^{3+} $^2F_{5/2}$ level (shown in Fig. 3.8).

curves was fitted with a single exponential function and an average lifetime τ was determined for the Yb^{3+} $^2F_{5/2}$ emission and plotted as a function of temperature in Fig. 3.9. The luminescence lifetime at 4 K is approximately 410 μs and decreases to 100 μs as the temperature is increased to 50 K. When the temperature is increased further the lifetime starts to increase again, and at room temperature the lifetime is 405 μs, only slightly shorter than the lifetime at 4 K. The same trend was also observed for the sample doped with 0.5% Pr^{3+} and 5% Yb^{3+}. These results are consistent with the temperature dependence of the luminescence intensities and are explained by the temperature dependent energy transfer between the Yb^{3+} $^2F_{5/2}$ level and the Pr^{3+} $^1G_4$ level. As the temperature is raised from 4 to 50 K energy migration from Yb^{3+} to the Pr^{3+} $^1G_4$ level becomes more efficient, leading to a shortening of the lifetime for the Yb^{3+} $^2F_{5/2}$ emission. The Pr^{3+} $^1G_4$ level is some 300 cm^{-1} lower in energy than the Yb^{3+} $^2F_{5/2}$ level and is an efficient trap. The thermal energy at temperatures below 50 K is not sufficient to allow energy transfer from the Pr^{3+} $^1G_4$ level back to the Yb^{3+} $^2F_{5/2}$ level. At temperatures above 50 K thermally activated back-transfer starts to play a role and thermally activated transfer from Pr^{3+} $^1G_4$ to Yb^{3+} $^2F_{5/2}$ occurs. This process becomes more efficient at higher temperatures, leading to increasing lifetimes and higher intensity for the Yb^{3+} $^2F_{5/2}$ emission as the temperature is increased from

50 K to room temperature. The results on the temperature dependent luminescence and decay of the $^2F_{5/2}$ emission show that trapping of the excitation energy in the $^1G_4$ level of Pr^{3+} contributes to concentration quenching and can be reduced by raising the temperature and the Yb^{3+} concentration, promoting back-transfer to the $^2F_{5/2}$ level of Yb^{3+}. On the other hand, raising the Yb^{3+} concentration also induces faster energy migration to (other) traps which lowers the Yb^{3+} emission intensity. Optimization for the highest 1000 nm emission intensity will require optimizing the Pr^{3+} and Yb^{3+} concentration, as well as reducing the concentration of quenching centers by optimized synthesis procedures.

3.4 Conclusions

Downconversion of one blue-green photon to two NIR photons has been demonstrated in YF_3:Pr^{3+},Yb^{3+} and takes place through two-step energy transfer from Pr^{3+} to Yb^{3+}. Room temperature emission and luminescence decay measurements show that the energy transfer efficiency increases with Yb^{3+} concentration, up to 86% for YF_3 doped with 0.5% Pr^{3+} and 30% Yb^{3+}. Comparison of the relative intensities for the $^3H_4 \rightarrow {}^3P_J$ and $^3H_4 \rightarrow {}^1D_2$ absorption/excitation lines in diffuse reflectance/excitation spectra confirms that downconversion is efficient for this lanthanide couple. Concentration quenching of the Yb^{3+} $^2F_{5/2}$ emission reduces the NIR output for Yb^{3+} concentrations which are needed to achieve efficient downconversion. Low temperature emission and luminescence decay measurements show that the Pr^{3+} $^1G_4$ level plays an important role in the energy transfer between Pr^{3+} and Yb^{3+} and the concentration quenching. Not only does energy transfer from Pr^{3+} to Yb^{3+} take place, but transfer of excitation energy from the Yb^{3+} $^2F_{5/2}$ level to the $^1G_4$ level of Pr^{3+} is also possible. This back-transfer quenches the Yb^{3+} emission around 1000 nm especially at low temperatures. Concentration quenching can be reduced by optimized synthesis conditions (to reduce the concentration of quenching centers related to defects or impurities), varying the concentration of Yb^{3+} and Pr^{3+} and choosing a system where the energy difference between the lowest $^1G_4$ crystal field component of Pr^{3+} and the $^2F_{5/2}$ level of Yb^{3+} is as small as possible to reduce the trapping efficiency of the Pr^{3+} $^1G_4$ level.

References

[1] W. Shockley and H. Queisser, *Detailed balance limit of efficiency of p-n junction solar cells*, J. Appl. Phys. **32**, 510 (1961).

[2] M. Green, K. Emery, Y. Hishikawa, and W. Warta, *Solar cell efficiency tables (version 33)*, Prog. Photovolt: Res. Appl. **17**, 85 (2009).

[3] F. Auzel, *Upconversion and anti-Stokes processes with f and d ions in solids*, Chem. Rev. **104**, 139 (2004).

[4] R. Wegh, H. Donker, K. Oskam, and A. Meijerink, *Visible quantum cutting in $LiGdF_4$:Eu^{3+} through downconversion*, Science **283**, 663 (1999).

[5] K. Oskam, R. Wegh, H. Donker, E. van Loef, and A. Meijerink, *Downconversion: a new route to visible quantum cutting*, J. Alloy Comp. **300-301**, 421 (2000).

[6] R. Wegh, E. van Loef, and A. Meijerink, *Visible quantum cutting via downconversion in $LiGdF_4$:Er^{3+},Tb^{3+} upon Er^{3+} $4f^{11} \rightarrow 4f^{10}5d$ excitation*, J. Lumin. **90**, 111 (2000).

[7] P. Vergeer, T. Vlugt, M. Kox, M. den Hertog, J. van der Eerden, and A. Meijerink, *Quantum cutting by cooperative energy transfer in $Yb_xY_{1-x}PO_4$:Tb^{3+}*, Phys. Rev. B. **71**, 014119 (2005).

[8] Q. Zhang, G. Yang, and Z. Jiang, *Cooperative downconversion in $GdAl_3(BO_3)_4$: RE^{3+},Yb^{3+} (RE=Pr, Tb, and Tm)*, Appl. Phys. Lett. **91**, 051903 (2007).

[9] J. Yuan, X. Zeng, J. Zhao, Z. Zhang, H. Chen, and X. Yang, *Energy transfer mechanisms in Tb^{3+},Yb^{3+} codoped Y_2O_3 downconversion phosphor*, J. Phys. D: Appl. Phys. **41**, 105406 (2008).

[10] G. Lakshminarayana, H. Yang, S. Ye, Y. Liu, and J. Qiu, *Cooperative downconversion luminescence in Pr^{3+}/Yb^{3+}:SiO_2-Al_2O_3-BaF_2-GdF_3 glasses*, J. Mater. Res. **23**, 3090 (2008).

[11] G. Lakshminarayana, H. Yang, S. Ye, Y. Liu, and J. Qiu, *Co-operative downconversion luminescence in Tm^{3+}/Yb^{3+}:SiO_2-Al_2O_3-LiF-GdF_3 glasses*, J. Phys. D: Appl. Phys. **41**, 175111 (2008).

[12] B. van der Ende, L. Aarts, and A. Meijerink, *Near-infrared quantum cutting for photovoltaics*, Adv. Mat. **21**, 3073 (2009).

[13] P. Bendall, C. Catlow, J. Corish, and P. Jacobs, *Defect aggregation in anion-excess fluorites II. Clusters containing more than two impurity atoms*, J. Solid State Chem. **51**, 159 (1984).

[14] D. Tallant, D. Moore, and J. Wright, *Defect equilibria in fluorite structure crystals*, J. Chem. Phys. **67**, 2897 (1977).

[15] H. Rast, H. Caspers, and S. Miller, *Lattice vibrations and infrared properties of yttriumfluoride*, Phys. Rev. **180**, 890 (1969).

[16] B. Judd, *Optical absorption intensities of rare-earth ions*, Phys. Rev. **127**, 750 (1962).

[17] G. Ofelt, *Intensities of crystal spectra of rare-earth ions*, J. Chem. Phys. **37**, 511 (1962).

[18] C. De Mello Donegá, G. Dirksen, H. Folkerts, A. Meijerink, and G. Blasse, *The vibronic spectroscopy and luminescence concentration quenching of the Pr^{3+} ion in La_2O_3, LaOF and $LiYF_4$*, J. Phys. Chem. Solids **56**, 267 (1995).

[19] M. Malinowski, M. Joubert, and B. Jacquier, *Dynamics of the IR-to-blue wavelength upconversion in Pr^{3+}-doped yttrium aluminium garnet and $LiYF_4$ crystals*, Phys. Rev. B. **50**, 12367 (1994).

4

Downconversion in $NaYF_4$ doped with Er^{3+} and Yb^{3+}

Abstract

Downconversion is a promising avenue to boost the efficiency of solar cells by absorbing one higher energy visible photon and emitting two lower energy near-infrared photons. Here the efficiency of downconversion for the Er^{3+}–Yb^{3+} couple is investigated in $NaYF_4$, a well-known host lattice for efficient upconversion with Er^{3+}–Yb^{3+}. Analysis of the excitation and emission spectra for $NaYF_4$ doped with 1% Er^{3+} and co-doped with 0, 5, 10 or 30% Yb^{3+} shows that visible to NIR downconversion is inefficient. Downconversion by the scheme based on the reverse of the upconversion process is hampered by fast multi-phonon relaxation from the $^4F_{7/2}$ level (the starting level for downconversion) to the $^4S_{3/2}$ level. Energy transfer from the $^4S_{3/2}$ level of Er^{3+} to Yb^{3+} is shown to be inefficient. Efficient downconversion from the $^4G_{11/2}$ of Er^{3+} level is observed, resulting in emission of two photons (one around 980 nm and one around 650 nm) after absorption of a single 380 nm photon.

4.1 Introduction

A large part of the energy losses that limit the conversion efficiency of solar cells to 30% is related to the spectral mismatch [1]. Photons with an energy smaller than the band-gap (E_g) will not be absorbed (sub-band-gap transmission) and a large part of the energy of photons with an energy larger than the band-gap is lost as heat (thermalization losses). The energy losses related to the spectral mismatch can be reduced by adapting the solar cell by combining multiple semiconductor materials with different bandgaps, each converting a different part of the solar spectrum with high efficiency. This approach has been successfully applied and energy efficiencies over 40% have been reported [2]. An alternative way to reduce the spectral mismatch losses is through adapting the solar spectrum so that the solar cell can use it more efficiently.

There are two options to adapt the solar spectrum. The first option is to add two lower-energy photons (that are transmitted) to obtain one higher energy photon that can be absorbed by the solar cell. This process is known as upconversion (UC) and is especially useful for solar cells with a large band-gap where transmission losses dominate. The second way to adapt the solar spectrum is to split one higher energy photon to obtain two photons with a smaller energy. Each of these photons can subsequently be absorbed by the solar cell and generate an electron-hole pair. This is known as downconversion (DC) and is most beneficial for solar cells with a smaller band-gap where thermalization losses are the major loss factor. Because one photon is 'cut' into two smaller energy photons this process is also known as quantum cutting.

Lanthanide ions are very well suited to use for DC or UC because they have a rich energy level structure that allows for efficient spectral conversion. There are many examples of efficient up- and downconversion using lanthanides, either with one type of lanthanide ion or a pair of lanthanide ions [3, 4].

Trupke *et al.* have performed extensive calculations to determine the effect of using either up- or downconversion materials in combination with solar cells [5–7]. With an ideal downconverter material (splitting every photon above 2 E_g into two photons that both can be absorbed) a limit of efficiency of 40% is possible for a solar cell with a band gap of 1.1 eV [5]. Combining a ~2 eV solar cell with an ideal upconverter can raise the upper limit of the conversion efficiency to 50% [6, 7]. An important issue in the case of UC materials is that UC is a nonlinear process: for the two step UC process (where two photons are added to obtain one photon with a larger energy) the UC light intensity I_{UC} is proportional to square of the incident light intensity I_i. Therefore high conversion efficiencies are only obtained at sufficiently high excitation density which can be easily realized using lasers, but will require strong concentration of sunlight. The most efficient UC is realized using lanthanide ions [3]. An example of a particularly efficient upconverting couple is Er^{3+}–Yb^{3+}. Under high power laser excitation an efficiency of around 50% has been reported for the conversion of NIR (~1000 nm) to visible light in $NaYF_4$:Er^{3+}, Yb^{3+} [8]. Another example is NIR upconversion by $NaYF_4$ doped with Er^{3+}, which was applied to the rear of a silicon solar cell and shown to convert 1400-1500 nm NIR to photons that can be absorbed by the c-Si solar cell [7, 9].

Contrary to UC, DC is a linear process. This makes it possible to obtain high conversion efficiencies, independent of the incident power and allows for the use of non-concentrated sunlight. Compared to UC materials, demonstrations of efficient DC materials are limited. The Gd^{3+}–Eu^{3+} couple in a $LiGdF_4$ host lattice shows efficient DC (internal quantum efficiency of approximately 190%) and Er^{3+}, Gd^{3+} and Tb^{3+} in the same host lattice have an efficiency of 130% [4, 10, 11]. Both of these are examples of systems where downconversion of VUV photons into two visible photons take place.

Downconversion of UV or visible photons into NIR photons was first demonstrated in (Y, Yb)PO_4:Tb^{3+} [12]. After excitation into the $^5D_4$ state of the Tb^{3+}-ion two neighboring Yb^{3+}-ions are excited through a cooperative energy transfer process. The $^5D_4$ level of Tb^{3+} is situated at about twice the energy of the Yb^{3+} $^2F_{7/2}$ level, and after energy transfer Yb^{3+} emission is observed around 1000 nm. This is just above the band gap of crystalline silicon which makes Yb^{3+} an attractive candidate for DC materials to be used in combination with c-Si solar cells. More recently, cooperative downconversion has also been reported for Tb^{3+}–Yb^{3+} [13, 14] and other lanthanide

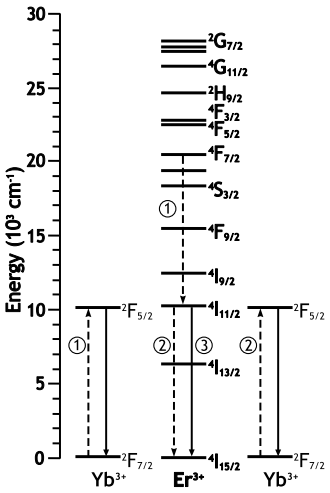

Figure 4.1: Energy level scheme of the Er^{3+} ($4f^{11}$) and Yb^{3+} ($4f^{13}$) couple showing two possible mechanisms for downconversion. First energy is transferred from Er^{3+} to one Yb^{3+} neighbor (① - Er^{3+} ($^4F_{7/2} \rightarrow {}^4I_{11/2}$), Yb^{3+} ($^2F_{7/2} \rightarrow {}^2F_{5/2}$)) followed by emission of an infrared photon by Yb^{3+} ($^2F_{5/2} \rightarrow {}^2F_{7/2}$). The remaining energy can either be transferred to a second Yb^{3+} neighbor (② - Er^{3+} ($^4I_{11/2} \rightarrow {}^4I_{15/2}$), Yb^{3+} ($^2F_{7/2} \rightarrow {}^2F_{5/2}$)), or emitted by Er^{3+} (③ - $^4I_{11/2} \rightarrow {}^4I_{15/2}$).

couples, viz. Pr^{3+}–Yb^{3+} [15] and Tm^{3+}–Yb^{3+} [16]. However, it is not clear that the second-order cooperative energy transfer process is the operative mechanism in the Pr^{3+}–Yb^{3+} system, as first-order energy transfer processes are also possible, and are expected to dominate [17]. The lower efficiency of second-order cooperative energy transfer process makes it only efficient at very high Yb^{3+} concentrations where the Yb^{3+} emission is largely quenched through concentration quenching. To achieve more efficient energy transfer, an intermediate level on the donor ion should be used in order to obtain downconversion through two resonant energy transfer steps.

In this chapter we investigate if efficient downconversion is possible with the Er^{3+}–Yb^{3+} couple. In the past it has been shown that Er^{3+} and Yb^{3+} is a particularly efficient upconverting couple [8]. We have chosen $NaYF_4$ as a host lattice to study downconversion since this host is well known for efficient upconversion by Yb^{3+}–Er^{3+} and the host lattice has a small phonon energy (maximum phonon energy 400 cm^{-1}). A low phonon energy is crucial: in Fig. 4.1 the downconversion scheme for the Er^{3+}–Yb^{3+} couple is shown. It is the reverse of the well-known upconversion scheme. In the first step energy transfer from the $^4F_{7/2}$ level of Er^{3+} occurs: Er^{3+}

($^4F_{7/2} \rightarrow {}^4I_{11/2}$), Yb^{3+} ($^2F_{7/2} \rightarrow {}^2F_{5/2}$) thus populating the $^2F_{5/2}$ level of Yb^{3+}. In the second step energy transfer to a second Yb^{3+}-ion can occur from the $^4I_{11/2}$ level of Er^{3+} while it is also possible that Er^{3+} emits a photon around 1000 nm from the $^4I_{11/2}$ level. In order to have efficient downconversion it is crucial to prevent (fast) non-radiative decay from the $^4F_{7/2}$ level to the $^4S_{3/2}$ level since downconversion from the $^4S_{3/2}$ level is not possible. Since non-radiative relaxation from the $^4F_{7/2}$ level is determined by multi-phonon relaxation, a low phonon energy is required to reduce the multi-phonon relaxation rate. In this chapter we will show that downconversion from the $^4F_{7/2}$ level cannot compete with multi-phonon relaxation from this level and that host lattices with a lower phonon energy are required. However, from the higher energy $^4G_{11/2}$ level, downconversion is observed.

4.2 Methods

Powder samples of $NaYF_4$ doped with Er^{3+} and Yb^{3+} were prepared by a dry mixture method. NaF (Merck, p.a., 5% excess) was mixed with YF_3 (Chempur, 5N), ErF_3 (Highways, 3N) and YbF_3 (Chempur, 4N). The blend was then put into an alumina crucible and fired in an oven together with an excess of NH_4F (Sigma-Aldrich, 98+%) under a nitrogen flow. The samples were first heated to 300°C for two hours and then to 550°C for three hours. After the samples had cooled sufficiently they were crushed with a pestle and mortar and x-ray diffraction measurements were performed to check for phase purity.

Diffuse reflectance spectra were measured with a Perkin-Elmer Lambda 950 UV/VIS/IR absorption spectrometer. Emission and excitation spectra were measured with a SPEX DM3000F spectrofluorometer with a 450 W Xe lamp as the excitation source. Excitation and emission wavelengths were selected with a double-grating 0.220 m SPEX 1680 monochromator (1200 l/mm) blazed at 300 nm. Emission spectra were recorded by focusing the emitted light on a fiber guiding the light to a 0.3 m monochromator (Scientific Spectra Pro, Princeton Instruments) where the emission light is dispersed by a 150 l/mm grating or a 1200 l/mm grating, both blazed at 500 nm. The dispersed light was detected with a Princeton Instruments 300i charge coupled device (CCD). The SPEX spectrofluorometer is equipped with an Oxford helium flow cryostat for low temperature measurements. The spectra were not corrected for the instrumental response.

Lifetime measurements with an excitation wavelength of 380 nm were performed with a Lambda Physik LPD3000 tunable dye laser using a BIBUQ dye solution (tunable between 367-405 nm). The dye laser is pumped by a Lambda Physik LPX100

excimer (XeCl) laser. The typical pulse width for the setup is ~20 ns and the repetition rate is 10 Hz.

4.3 Results and discussion

4.3.1 Characterization

Samples of $NaYF_4$ doped with 1 mol% Er^{3+} and 0, 5, 10, and 30 mol% Yb^{3+} and one sample doped with 5mol% Yb^{3+} and no Er^{3+} were synthesized. X-ray diffraction measurements gave similar results for all five samples. They consist mostly of the hexagonal β crystal phase, although trace amounts of the cubic α phase of $NaYF_4$ are also present. The hexagonal β crystal phase has been shown to be the more efficient of the two crystal phases for upconversion [18].

In the diffuse reflectance spectra (Fig. 4.2) it can be seen that the absorption strengths for the peaks corresponding to Er^{3+} transitions (e.g. the $^4I_{15/2} \rightarrow {}^4F_{7/2}$ transition around 500 nm and the $^4I_{15/2} \rightarrow {}^4I_{13/2}$ transition around 1550 nm) are the same for all samples that were doped with Er^{3+}. This means that the Er^{3+} concentration incorporated in the various samples is similar, as expected on the same amounts of Er^{3+} (1 mol%) present in the starting mixture. The absorption strength of the peak for the Yb^{3+} absorption around 1000 nm varies according to the Yb^{3+} concentration present in the starting mixtures. In the UV range an absorption band between 200 and 400 nm is observed which is probably related to defects, possibly involving oxygen impurities. The band is strongest for the sample co-doped with 1% Er^{3+} and 5% Yb^{3+}.

4.3.2 Emission spectra

In Fig. 4.3 the emission spectra of $NaYF_4$:Er^{3+}(1%), Yb^{3+}(0, 5, 10, 30%) are shown. The spectra were measured under identical conditions so that the intensities of the emissions may be compared. In the sample doped with Er^{3+} only, excitation in the Er^{3+} $^4F_{5/2}$ (451 nm) level yields emission from the $^4S_{3/2}$, $^4F_{9/2}$ and $^4I_{11/2}$ levels, but no emission from the $^4F_{7/2}$ level is observed. This shows that non-radiative relaxation from the $^4F_{7/2}$ to the next lower level ($^2H_{11/2}$) is fast and radiative decay from the $^4F_{7/2}$ level cannot compete with non-radiative relaxation. The intensity of the Er^{3+} emission decreases upon increasing Yb^{3+} concentration but this does not lead to a strong increase of the Yb^{3+} emission. In all samples the Yb^{3+} emission around 980 nm is weak which shows that after energy transfer from Er^{3+} to Yb^{3+}, the Yb^{3+} luminescence is quenched, probably due to concentration quenching. The present results

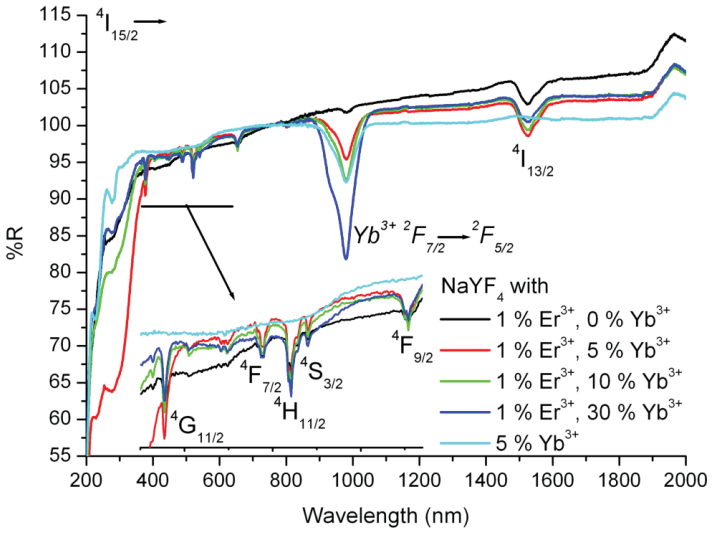

Figure 4.2: Diffuse reflectance spectra for $NaYF_4$:Er^{3+}(1%), Yb^{3+}(0, 5, 10, 30%) and $NaYF_4$:Yb^{3+}(5%).

show that non-radiative relaxation from the $^4F_{7/2}$ level is too fast in $NaYF_4$ and down-conversion of one visible into two NIR photons as shown schematically in Fig. 4.1 is not possible with the Er^{3+}–Yb^{3+} couple in this host lattice. The energy difference between the $^4F_{7/2}$ level and the $^2H_{11/2}$ level is typically around 1300 cm^{-1} [19–21]. The maximum phonon energy in the $NaYF_4$ lattice is some 400 cm^{-1} which means that the energy gap can be bridged by ~3 phonons. Based on the energy gap law and experimental results a rule of thumb predicts that radiative decay and multi-phonon relaxation can compete when the gap is five times the phonon energy [8]. For a smaller gap multi-phonon relaxation dominates in agreement with the present observations. After fast multi-phonon relaxation to the $^2H_{11/2}$ level, further relaxation to the $^4S_{3/2}$ level occurs. Emission from the $^4S_{3/2}$ level is observed to be partly quenched by Yb^{3+}. The quenching is however not very efficient. Even for Yb^{3+} concentrations as high as 30% the remaining Er^{3+} ($^4S_{3/2}$) emission intensity is more than $^1/_3$ of the intensity for the sample without Yb^{3+} even though almost every Er^{3+}-ion has one or more nearest Yb^{3+} neighbors. If we consider the energy level diagrams of Er^{3+} and Yb^{3+} we can understand the relatively low efficiency of the cross-relaxation process from the $^4S_{3/2}$ level of Er^{3+}. There are two possibilities for cross-relaxation: Er^{3+} ($^4S_{3/2} \rightarrow {}^4I_{11/2}$), Yb^{3+} ($^2F_{7/2} \rightarrow {}^2F_{5/2}$) or Er^{3+} ($^4S_{3/2} \rightarrow {}^4I_{13/2}$), Yb^{3+} ($^2F_{7/2} \rightarrow {}^2F_{5/2}$). The energy for the transition on Yb^{3+} is around 10 200 cm^{-1}. There is a large energy mismatch

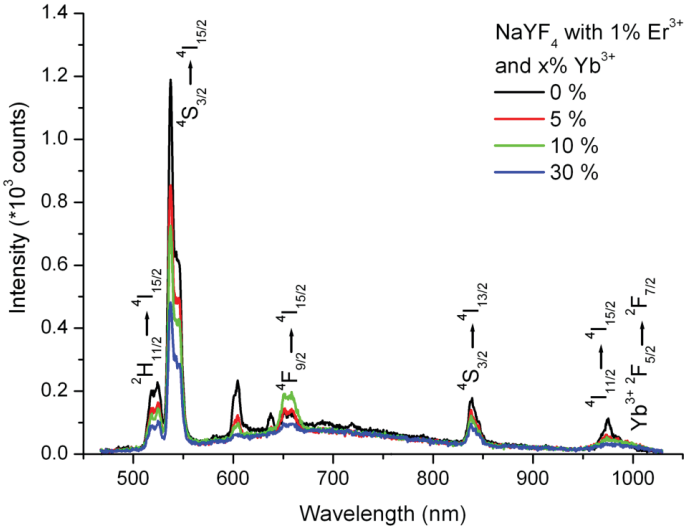

Figure 4.3: Room temperature emission spectra of $NaYF_4:Er^{3+}$(1%), Yb^{3+}(0, 5, 10, 30%). The excitation wavelength is 451 nm ($^4F_{5/2}$ level).

for both cross-relaxation processes. The $^4S_{3/2} \rightarrow {}^4I_{11/2}$ energy difference is around 8500 cm^{-1} and the cross-relaxation process would involve a 1700 cm^{-1} thermal activation energy (four phonon absorption). This will have a very low probability at 300 K. The energy mismatch for the second cross-relaxation process is similar but now the energy difference can be made up by emission of four phonons which is possible, albeit with low probability, also at low temperatures. The observed energy transfer from the $^4S_{3/2}$ state of Er^{3+} to Yb^{3+} is therefore assigned to a four-phonon assisted cross-relaxation process Er^{3+} ($^4S_{3/2} \rightarrow {}^4I_{13/2}$), Yb^{3+} ($^2F_{7/2} \rightarrow {}^2F_{5/2}$).

Fig. 4.4 shows the room temperature emission spectra for excitation in the Er^{3+} $^4G_{11/2}$ level (380 nm) for samples doped with 1% Er^{3+} and 0, 5, 10 and 30% Yb^{3+}. The emission spectra show the same Er^{3+} emissions as for excitation in the $^4F_{7/2}$ level, but with different relative intensities. For the samples co-doped with Yb^{3+} the $^2F_{5/2} \rightarrow {}^2F_{7/2}$ emission is observed, indicating that there is energy transfer from Er^{3+} to Yb^{3+}. Emission from the Er^{3+} $^4I_{11/2} \rightarrow {}^4I_{15/2}$ transition is observed at slightly shorter wavelength than the $^2F_{5/2} \rightarrow {}^2F_{7/2}$ transition of Yb^{3+}. Upon raising the Yb^{3+} concentration, the $^4S_{3/2}$ emission intensity decreases. However, the intensity of emission from the $^4F_{9/2} \rightarrow {}^4I_{15/2}$ transition increases, contrary to the situation for excitation in the $^4F_{5/2}$ level where all Er^{3+} emission are observed to decrease upon rais-

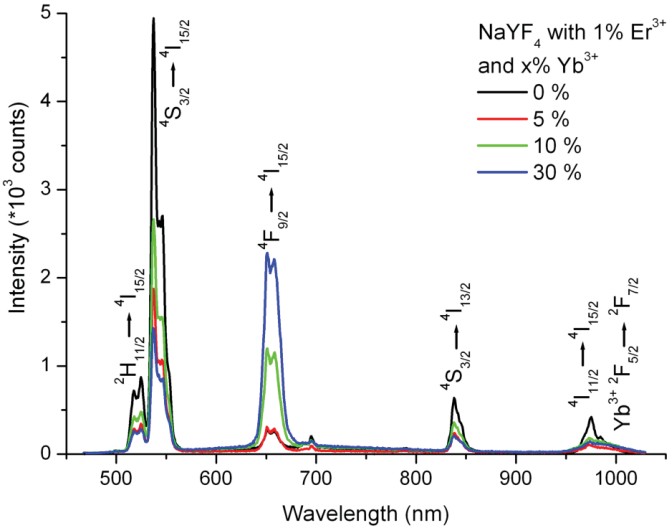

Figure 4.4: Room temperature emission spectra of $NaYF_4$:Er^{3+}(1%), Yb^{3+}(0, 5, 10, 30%) for excitation at 380 nm ($^4G_{11/2}$ level).

ing the Yb^{3+} concentration (*vide supra*). The increase of the $^4F_{9/2}$ emission is explained by efficient cross-relaxation between Er^{3+} and Yb^{3+}: Er^{3+} ($^4G_{11/2} \rightarrow {}^4F_{9/2}$), Yb^{3+} ($^2F_{7/2} \rightarrow {}^2F_{5/2}$). The energy mismatch for this cross-relaxation process is small (~800 cm^{-1}) and can be accommodated by a two-phonon emission process. This process populates the $^4F_{9/2}$ level which yields the characteristic red emission of Er^{3+} around 660 nm (see Fig. 4.5). At the same time, Yb^{3+} is raised to the $^2F_{5/2}$ excited state. However, the $^2F_{5/2}$ emission from Yb^{3+} is weak. Both concentration quenching of the Yb^{3+} emission and the weak response of the instrument in this spectral region contribute to the low emission intensity of Yb^{3+} observed in the spectrum. The efficiency of the cross-relaxation process can be estimated from the relative intensities of the $^4S_{3/2}$ emission and the $^4F_{9/2}$ emission. For the sample co-doped with 30% Yb^{3+}, the $^4F_{9/2}$ emission dominates, indicating that more than half of the Er^{3+} show cross-relaxation. Efficient cross-relaxation from the $^4G_{11/2}$ level can be expected: the energy gap to the next lower $^4G_{9/2}$ level is typically 1800 cm^{-1} and requires five phonons to be bridged. As a result multi-phonon relaxation will be slow and cross-relaxation can compete with non-radiative multi-phonon relaxation. The efficient cross-relaxation from the $^4G_{11/2}$ level results in quantum cutting: absorption of a 380 nm photon gives the emission of a red 660 nm photon (from the $^4F_{9/2}$ level of Er^{3+}) and an infrared 980 nm photon (from the $^2F_{5/2}$ level of Yb^{3+}). For solar cell applications this quan-

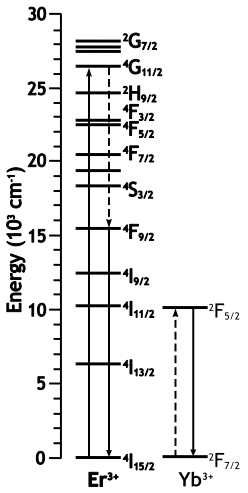

Figure 4.5: Energy level scheme of the Er^{3+} and Yb^{3+} couple showing the downconversion mechanism starting from the $^4G_{11/2}$ level.

tum cutting process is not very useful as only a small part of the solar spectrum has wavelengths shorter than 380 nm.

To study the Yb^{3+} emission spectra in more detail, higher resolution emission spectra were recorded in the spectral region around 1000 nm. In the spectra of the Yb^{3+} emission (Fig. 4.6) four peaks can be observed which can be explained by emission from the $^2F_{5/2}$ state to the four crystal field components of the $^2F_{7/2}$ ground state. The emission spectra for the three samples are very similar. A small shift in the positions of the peaks is observed upon raising the Yb^{3+} concentration, probably due to a small variation in the crystal field splitting resulting from the difference in ionic radius between Y^{3+} and Yb^{3+}. An extra peak around 982 nm is observed for the sample doped with 1% Er^{3+} and 30% Yb^{3+}. This is assigned to emission from an Yb^{3+} trap level, possibly Yb^{3+} next to an O^{2-}-ion on a F^- site. In the sample with 30% Yb^{3+} efficient energy migration over the Yb^{3+} sublattice will occur and the excitation energy can be trapped. In the samples doped with 5 or 10% Yb^{3+} energy migration is not yet efficient (the concentrations are below the percolation point) and energy transfer to the Yb^{3+} traps is much less probable.

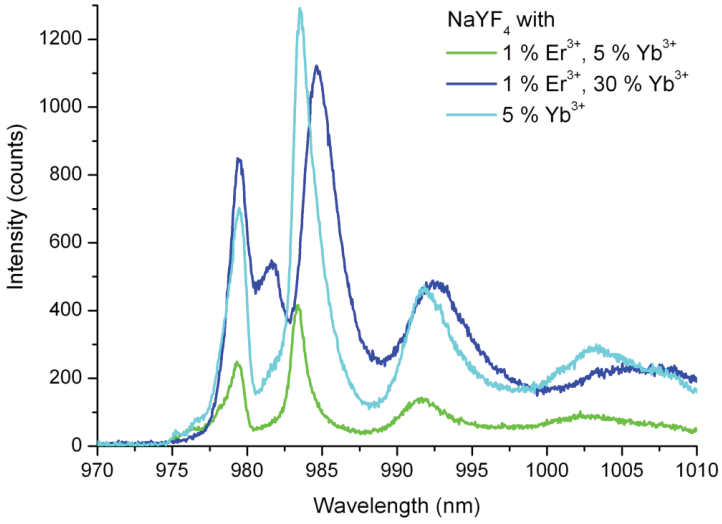

Figure 4.6: Emission spectra of the Yb^{3+} emission for $NaYF_4$:Yb^{3+}(5%) (λ_x = 954 nm), and $NaYF_4$:Er^{3+}(1%), Yb^{3+}(5, 30%) (λ_x = 380 nm) measured at 4 K.

4.3.3 Luminescence decay curves

To gain further insight in the energy transfer processes between Er^{3+} and Yb^{3+}, luminescence decay curves were recorded. Luminescence decay curves of Er^{3+} emission upon excitation in the $^4G_{11/2}$ level of Er^{3+} are shown in Figs. 4.7 and 4.8. In Fig. 4.7 luminescence decay curves are shown for the $^4F_{9/2}$ emission in samples doped with 1% Er^{3+} and between 0 and 30% Yb^{3+}. In the sample without Yb^{3+}, there is a clear build-up in the first part of the decay of the $^4F_{9/2}$ emission due to slow multi-phonon relaxation from the $^4G_{11/2}$ to the $^4F_{9/2}$ level. The very fast initial decay observed before the build-up may be due to scattered laser light reaching the detector or fast emission from Er^{3+} pairs where the $^4F_{9/2}$ level is populated by fast cross-relaxation between neighboring Er^{3+}-ions. The build-up disappears in the samples with Yb^{3+}, because the $^4F_{9/2}$ level is now efficiently populated by cross-relaxation with neighboring Yb^{3+}-ions (Er^{3+} ($^4G_{11/2} \rightarrow {}^4F_{9/2}$), Yb^{3+} ($^2F_{7/2} \rightarrow {}^2F_{5/2}$)). This observation provides additional evidence for the quantum cutting mechanism initiated by excitation in the $^4G_{11/2}$ level, as discussed in the previous section and shown in Fig. 4.5. The decay time of the $^4F_{9/2}$ emission depends only weakly on the Yb^{3+} concentration (560 μs for 5% Yb^{3+} to 440 μs for 30% Yb^{3+}) showing that energy transfer from the $^4F_{9/2}$ level of Er^{3+} to Yb^{3+} is inefficient. This is consistent with energy level scheme

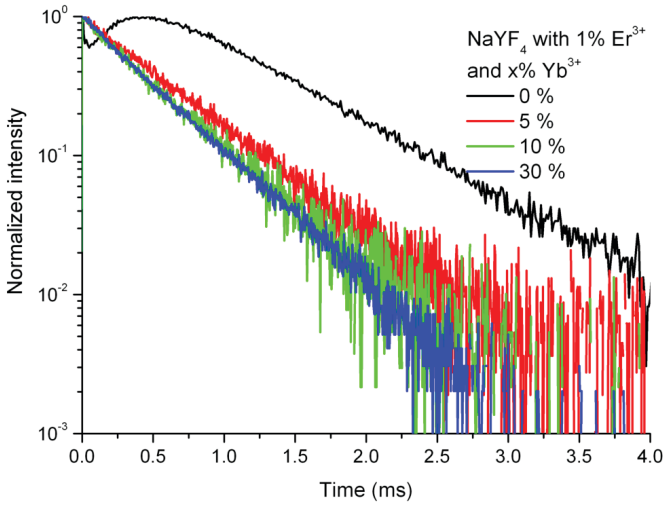

Figure 4.7: Luminescence decay curves for the $^4F_{9/2}$ emission in $NaYF_4$:Er^{3+}(1%), co-doped with 0, 5, 10 or 30% Yb^{3+} measured at room temperature. The excitation wavelength is 380 nm (into the $^4G_{11/2}$ level) and the emission wavelength is 654 nm ($^4F_{9/2} \rightarrow {}^4I_{15/2}$).

of Er^{3+}: there is no energy level 10 000 cm^{-1} below the $^4F_{9/2}$ level.

In Fig. 4.8 the decay curves of the $^4S_{3/2} \rightarrow {}^4I_{15/2}$ emission are shown upon excitation in the $^4G_{11/2}$ level. There is again a build-up in the signal, now due to relaxation from the $^4G_{11/2}$ level to the $^4S_{3/2}$ level. For the sample without Yb^{3+}, the $^4S_{3/2}$ emission decay is exponential with a decay time of 450 μs. As the Yb^{3+} concentration is increased, the decay of the $^4S_{3/2}$ emission becomes faster and non-exponential. This is due to energy transfer to neighboring Yb^{3+}-ions. The non-exponential character of the decay is explained by the fact that each Er^{3+} donor has a different distribution of Yb^{3+} acceptors around it. In the long time regime the exponential (~450 μs) decay of Er^{3+} is observed for those Er^{3+}-ions that do not have a nearest neighbor acceptor. Note that the shortening of the decay time is limited. This confirms that the energy transfer to Yb^{3+} is not efficient. The efficiency of energy transfer (the fraction of Er^{3+} that relaxes through energy transfer to Yb^{3+}, instead of through radiative decay) can be estimated from the integrals under the normalized decay curves [12]. From luminescence decay measurements energy transfer efficiencies for energy transfer from the Er^{3+} $^4S_{3/2}$ level to Yb^{3+} of 10, 11 and 28% can be estimated for the samples doped with 1% Er^{3+} and 5, 10 and 30% Yb^{3+}, respectively. Compared to the efficient energy transfer observed previously for the Pr^{3+}– Yb^{3+} [15, 17], Tm^{3+}–Yb^{3+} [16] and

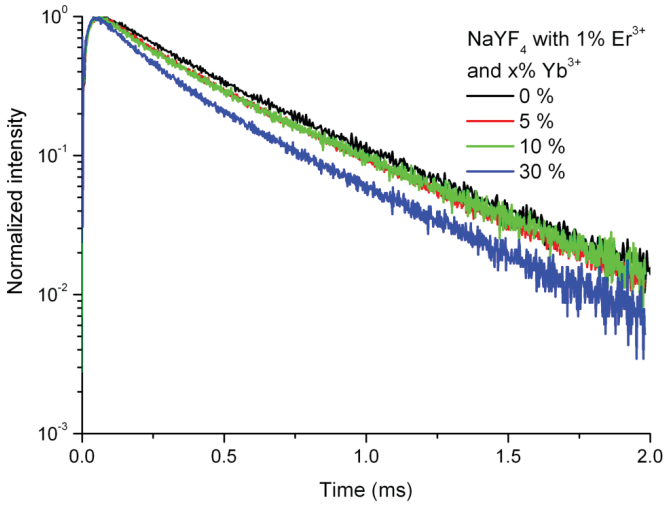

Figure 4.8: Luminescence decay curves for the $^4S_{3/2}$ emission in $NaYF_4$:Er^{3+}(1%), co-doped with 0, 5, 10 or 30% Yb^{3+} measured at room temperature. The excitation wavelength is 380 nm (into the $^4G_{11/2}$ level) and the emission wavelength is 543 nm ($^4S_{3/2} \rightarrow {}^4I_{15/2}$).

Tb^{3+}–Yb^{3+} [14, 22, 23] couples, this efficiency is low and shows that the Er^{3+}–Yb^{3+} couple is unattractive as a downconversion couple in host lattices where the relaxation from the $^4F_{7/2}$ level to the $^4S_{3/2}$ level is fast. Only in host lattices with lower phonon energies (i.e. chloride and bromide host materials) downconversion from the $^4F_{7/2}$ level may compete with multi-phonon relaxation and efficient quantum cutting may be achieved.

4.4 Conclusions

Luminescence spectra (excitation and emission) and luminescence decays curves have been recorded for $NaYF_4$:Er^{3+} 1% co-doped with 0, 5, 10, or 30% Yb^{3+} to investigate the potential of the Er^{3+}–Yb^{3+} couple for downconversion. The results show that the desired downconversion process from the $^4F_{7/2}$ level (the inverse of the efficient upconversion process) has a very low efficiency due to fast multi-phonon relaxation from the $^4F_{7/2}$ to the $^4S_{3/2}$ via the intermediate $^2H_{11/2}$ level. Based on the energy gap between the $^4F_{7/2}$ and the $^2H_{11/2}$ level (typically 1300 cm^{-1}) this is not unexpected in hosts with phonon energies over 250 cm^{-1}. In a host with a smaller phonon energies,

viz. chloride or bromide host materials, emission from the $^4F_{7/2}$ level, and therefore downconversion, may be possible.

Upon excitation in the $^4G_{11/2}$ level (around 380 nm) efficient downconversion is observed. The increase in emission from the Er^{3+} $^4F_{9/2}$ level upon raising the Yb^{3+} concentration, is due to a cross relaxation process involving the $^4G_{11/2} \rightarrow {}^4F_{9/2}$ transition of Er^{3+} and the $^2F_{7/2} \rightarrow {}^2F_{5/2}$ transition of Yb^{3+}. Cross-relaxation is followed by emission of a 650 nm photon from the Er^{3+} $^4F_{9/2}$ level and emission of a second photon (around 980 nm) by Yb^{3+}. This shows that quantum cutting of a 380 nm photon into a 650 nm photon and a 1000 nm photon is possible with the Er^{3+}–Yb^{3+}couple. Spectral conversion for solar cells using this downconversion scheme is not promising as the efficiency gain is limited due to the small fraction of the solar spectrum available in the wavelength region below 380 nm.

References

[1] W. Shockley and H. Queisser, *Detailed balance limit of efficiency of p-n junction solar cells*, J. Appl. Phys. **32**, 510 (1961).

[2] M. Green, K. Emery, Y. Hishikawa, and W. Warta, *Solar cell efficiency tables (version 33)*, Prog. Photovolt: Res. Appl. **17**, 85 (2009).

[3] F. Auzel, *Upconversion and anti-Stokes processes with f and d ions in solids*, Chem. Rev. **104**, 139 (2004).

[4] R. Wegh, H. Donker, K. Oskam, and A. Meijerink, *Visible quantum cutting in $LiGdF_4$:Eu^{3+} through downconversion*, Science **283**, 663 (1999).

[5] T. Trupke, M. Green, and P. Würfel, *Improving solar cell efficiency by down-conversion of high-energy photons*, J. Appl. Phys. **92**, 1668 (2002).

[6] T. Trupke, M. Green, and P. Würfel, *Improving solar cell efficiencies by up-conversion of sub-band-gap light*, J. Appl. Phys. **92**, 4117 (2002).

[7] T. Trupke, A. Shalav, B. Richards, P. Würfel, and M. Green, *Efficiency enhancement of solar cells by luminescent up-conversion of sunlight*, Sol. En. Mat. Sol. Cell. **90**, 3327 (2006).

[8] J. Suyver, A. Aebischer, D. Biner, P. Gerner, J. Grimm, S. Heer, K. Krämer, C. Reinhard, and H. Güdel, *Novel materials doped with trivalent lanthanides and transition metal ions showing near-infrared to visible photon conversion*, Opt. Mat. **27**, 1111 (2005).

[9] A. Shalav, B. Richards, T. Trupke, K. Krämer, and H. Güdel, *Application of $NaYF_4$:Er^{3+} up-converting phophors for enhanced near-infrared silicon solar cell response*, Appl. Phys. Lett. **86**, 013505 (2005).

[10] K. Oskam, R. Wegh, H. Donker, E. van Loef, and A. Meijerink, *Downconversion: a new route to visible quantum cutting*, J. Alloy Comp. **300-301**, 421 (2000).

[11] R. Wegh, E. van Loef, and A. Meijerink, *Visible quantum cutting via downconversion in $LiGdF_4$:Er^{3+},Tb^{3+} upon Er^{3+} $4f^{11} \rightarrow 4f^{10}5d$ excitation*, J. Lumin. **90**, 111 (2000).

[12] P. Vergeer, T. Vlugt, M. Kox, M. den Hertog, J. van der Eerden, and A. Meijerink, *Quantum cutting by cooperative energy transfer in $Yb_xY_{1-x}PO_4$:Tb^{3+}*, Phys. Rev. B. **71**, 014119 (2005).

[13] Q. Zhang, G. Yang, and Z. Jiang, *Cooperative downconversion in $GdAl_3(BO_3)_4$: RE^{3+},Yb^{3+} (RE=Pr, Tb, and Tm)*, Appl. Phys. Lett. **91**, 051903 (2007).

[14] J. Yuan, X. Zeng, J. Zhao, Z. Zhang, H. Chen, and X. Yang, *Energy transfer mechanisms in Tb^{3+},Yb^{3+} codoped Y_2O_3 downconversion phosphor*, J. Phys. D: Appl. Phys. **41**, 105406 (2008).

[15] G. Lakshminarayana, H. Yang, S. Ye, Y. Liu, and J. Qiu, *Cooperative downconversion luminescence in Pr^{3+}/Yb^{3+}:SiO_2-Al_2O_3-BaF_2-GdF_3 glasses*, J. Mater. Res. **23**, 3090 (2008).

[16] G. Lakshminarayana, H. Yang, S. Ye, Y. Liu, and J. Qiu, *Co-operative downconversion luminescence in Tm^{3+}/Yb^{3+}:SiO_2-Al_2O_3-LiF-GdF_3 glasses*, J. Phys. D: Appl. Phys. **41**, 175111 (2008).

[17] B. van der Ende, L. Aarts, and A. Meijerink, *Near-infrared quantum cutting for photovoltaics*, Adv. Mat. **21**, 3073 (2009).

[18] K. Krämer, D. Biner, G. Frei, H. Güdel, M. Hehlen, and S. Lüthi, *Hexagonal sodium yttrium fluoride based green and blue emitting upconversion phosphors*, Chem. Mat. **16**, 1244 (2004).

[19] X. Zhou, P. Tanner, and D. Faucher, *Electronic spectra and crystal field analysis of Er^{3+} in Cs_2NaErF_6*, J. Phys. Chem. C **111**, 683 (2007).

[20] A. Tkachuk, S. Ivanova, L. Isaenko, A. Yellisseyev, M. Joubert, F. Guyot, and S. Payne, *Spectroscopic studies of erbium-doped potassium-lead double chloride crystals of KPb_2Cl_5:Er^{3+}: 1. Optical spectra and relaxation of excited states of the erbium ion in potassium-lead double chloride crystals*, Opt. Spectro. **95**, 722 (2003).

[21] U. Hömmerich, E. Nyein, and S. Trivedi, *Crystal growth, upconversion, and infrared emission properties of Er^{3+}-doped KPb_2Br_5*, J. Lumin. **113**, 100 (2005).

[22] Q. Zhang, C. Yang, and Y. Pan, *Cooperative quantum cutting in one-dimensional $(Yb_xGd_{1-x})Al_3(BO_3)_4$:$Tb^{3+}$ nanorods*, Appl. Phys. Lett. **90**, 021107 (2007).

[23] X. Huang and Q. Zhang, *Efficient near-infrared down conversion in Zn_2SiO_4:Tb^{3+},Yb^{3+} thin-films*, J. Appl. Phys. **105**, 053521 (2009).

5

Downconversion for the Er^{3+}–Yb^{3+} couple in low-phonon frequency host materials

Abstract

Downconversion of a single blue/green photon into two near-infrared photons offers a promising route to increase the efficiency of photovoltaic cells. Here we report on downconversion for the well-known upconversion couple Er^{3+}–Yb^{3+}doped into hosts with a low maximum phonon energy. An important energy level in both the upconversion and downconversion process is the $^4F_{7/2}$ level of Er^{3+} around 490 nm. While fast multi-phonon relaxation to the lower energy $^2H_{11/2}$/$^4S_{3/2}$ levels is beneficial for upconversion, it prevents efficient downconversion. To reduce multi-phonon relaxation, low phonon energy hosts were doped with Er^{3+} and a varying amount of Yb^{3+} co-dopant. The results show that downconversion from the $^4F_{7/2}$ level occurs, exciting two neighboring Yb^{3+}-ions to the $^2F_{5/2}$ level. However, in KPb_2Cl_5 the efficiency is low due to multi-phonon relaxation from the $^4F_{7/2}$ to the $^4S_{3/2}$ level via the intermediate $^2H_{11/2}$ level. Preliminary results for the Er^{3+}–Yb^{3+} couple in a host with an even lower phonon energy ($CsCdBr_3$) show that energy transfer from the Er^{3+} $^4F_{7/2}$ level to Yb^{3+} is more efficient in $CsCdBr_3$. A Cl^--Yb^{3+} charge transfer absorption band is observed between 300 and 400 nm for KPb_2Cl_5:Er^{3+}, Yb^{3+}. Excitation in this band results in two broad emission bands centered around 430 and 700 nm at temperatures below 30 K which are assigned to Cl^--Yb^{3+} charge transfer emission.

5.1 Introduction

The relatively low maximum efficiency (30%) for the conversion of solar energy into electricity for single junction solar cells is related to the spectral mismatch [1]. Low energy infrared (IR) photons cannot be absorbed and for high energy photons a large part of the energy is lost by thermalization of highly excited charge carriers. To increase the solar efficiency one can 'add' *two* IR photons to obtain *one* photon with a higher energy (upconversion, UC) or 'cut' a single high energy photon into two lower energies photons (downconversion, DC) that can both be absorbed by the solar cell. Lanthanide ions are promising candidates for efficient spectral conversion and there are various examples of efficient up- and downconversion using lanthanides, either with one type of lanthanide ion or a pair of lanthanide ions [2, 3].

Downconversion of *one* UV or visible photon into *two* NIR photons was first demonstrated in (Y,Yb)PO_4:Tb^{3+} [4] and later for other couples of lanthanides, viz. Pr^{3+}–Yb^{3+} [5] and Tm^{3+}–Yb^{3+} [6]. The choice for Yb^{3+} as the emitting acceptor ion was inspired by the favorable energy of the $^2F_{5/2}$ excited state (emitting around 1000 nm, just above the band gap of crystalline silicon) and the fact that the Yb^{3+}-

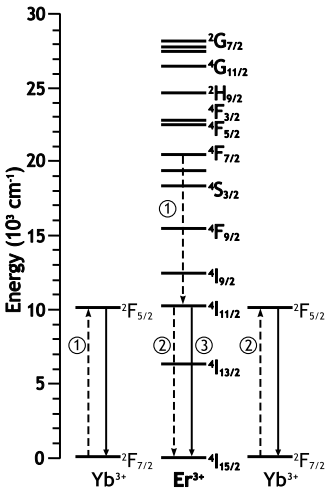

Figure 5.1: Energy level schemes of the Er^{3+} ($4f^{11}$) and Yb^{3+} ($4f^{13}$) couple showing two possible mechanisms for downconversion. First energy is transferred from Er^{3+} to one Yb^{3+} neighbor (① - Er^{3+} ($^4F_{7/2} \rightarrow {}^4I_{11/2}$), Yb^{3+} ($^2F_{7/2} \rightarrow {}^2F_{5/2}$)) followed by emission of an infrared photon by Yb^{3+} ($^2F_{5/2} \rightarrow {}^2F_{7/2}$)). The remaining energy can either be transferred to a second Yb^{3+} neighbor (② - Er^{3+} ($^4I_{11/2} \rightarrow {}^4I_{15/2}$), Yb^{3+} ($^2F_{7/2} \rightarrow {}^2F_{5/2}$)), or emitted by Er^{3+} (③ - $^4I_{11/2} \rightarrow {}^4I_{15/2}$).

ion has no other $4f$ excited states that can interfere with the downconversion process. This makes Yb^{3+} an attractive candidate for DC materials to be used in combination with c-Si solar cells. An obvious choice for a downconversion couple is the well-known upconversion couple Er^{3+}–Yb^{3+}. Efficient upconversion has been reported for this couple in many host lattices and it is used for the efficient detection of ~1000 nm IR radiation. The mechanism for upconversion has been well studied since the discovery of this couple by Auzel [7–9]. After excitation into the $^2F_{5/2}$ level of Yb^{3+} two sequential energy transfer steps excite the Er^{3+}-ion from the $^4I_{15/2}$ ground state to the $^4I_{11/2}$ excited state and from the $^4I_{11/2}$ excited state to the higher energy $^4F_{7/2}$ excited state (see Fig. 5.1 for the positions of the energy levels for Er^{3+} and Yb^{3+}). Visible emission may be observed from the $^4F_{7/2}$ state or, after relaxation, from the lower energy $^2H_{11/2}$ and $^4S_{3/2}$ states.

In a recent study [10] we investigated downconversion with the Er^{3+}–Yb^{3+}couple in $NaYF_4$, which is a well-known host for efficient upconversion with this couple [11–13]. In Fig. 5.1 the downconversion scheme for the Er^{3+}–Yb^{3+} couple is shown. In the first step energy transfer from the $^4F_{7/2}$ level of Er^{3+} occurs: Er^{3+} ($^4F_{7/2} \rightarrow {}^4I_{11/2}$),

Yb^{3+} ($^2F_{7/2} \rightarrow {}^2F_{5/2}$), thus populating the $^2F_{5/2}$ level of Yb^{3+}. In the second step energy transfer to a second Yb^{3+}-ion can occur from the $^4I_{11/2}$ level of Er^{3+} while it is also possible that Er^{3+} emits a photon around 1000 nm from the $^4I_{11/2}$ level. In order to realize efficient downconversion it is crucial to prevent (fast) non-radiative decay from the $^4F_{7/2}$ level to the $^4S_{3/2}$ level since downconversion from the $^4S_{3/2}$ level is not possible. Non-radiative relaxation from the $^4F_{7/2}$ level is reduced in a low phonon energy host lattice. The study on downconversion for the Er^{3+}–Yb^{3+} couple in $NaYF_4$ showed that the phonon energy in this fluoride (~400 cm^{-1}) is too high and fast multi-phonon relaxation prevents downconversion. Therefore we have chosen KPb_2Cl_5 and $CsCdBr_3$ as host lattices to study downconversion in Er^{3+}, Yb^{3+}. KPb_2Cl_5 has a small phonon energy (maximum phonon energy ~200 cm^{-1} [14,15]). In addition, it is one of the few chlorides that is not hygroscopic which is an important advantage for potential applications. In a comprehensive study by Tkachuk *et al.* [14] the energy levels and relaxation rates have been studied in detail for Er^{3+} in KPb_2Cl_5. $CsCdBr_3$ has an even lower phonon energy ($\hbar\omega$ ~180 cm^{-1}). A further advantage of this host lattice is that three doubly charged Cd will be replaced by two triply charged lanthanide ions. Therefore the lanthanide ions will form pairs in this host lattice, which facilitates efficient energy transfer between the ions.

The energy difference between the Er^{3+} $^4F_{7/2}$ level and the next lower level ($^2H_{11/2}$) is typically around 1300 cm^{-1} [14, 16, 17]. Based on the energy gap law and experimental results a rule of thumb predicts that radiative decay and multi-phonon relaxation can compete when the gap is five times the phonon energy [12]. For KPb_2Cl_5 and $CsCdBr_3$ 6 to 7 phonons are needed to bridge the energy gap, making non-radiative relaxation unlikely. Therefore DC with the Er^{3+}–Yb^{3+} couple should be possible in these host lattices. Here we focus on the $^4F_{7/2}$ level and energy transfer from this level to neighboring Yb^{3+}-ions in co-doped Er^{3+} in KPb_2Cl_5:Er^{3+}, $Yb^{3+}$and $CsCdBr_3$:Er^{3+}, Yb^{3+}. The results show that downconversion occurs, but multi-phonon relaxation is faster and causes the downconversion efficiency to be low in KPB_2Cl_5. For Er^{3+} in $CsCdBr_3$ $^4F_{7/2}$ emission is observed. Even though high downconversion efficiencies were not obtained in the preliminary studies on $CsCdBr_3$:Er^{3+}, Yb^{3+}, it is clear that bromides are a promising class of materials to achieve high downconversion efficiencies for the Er^{3+}–Yb^{3+} couple.

5.2 Methods

5.2.1 Synthesis

KPb_2Cl_5

Crystalline samples of KPb_2Cl_5 doped with Er^{3+} and Yb^{3+} were prepared in a high frequency furnace. KCl, $PbCl_2$, $ErCl_3$ and $YbCl_3$ were mixed in stoichiometric amounts. The blend was put into a quartz ampoule which was then evacuated and sealed to keep out air and moisture during synthesis. The ampoules were put into a high frequency furnace and first heated to 200°C for 2 hours, and then kept at 900°C for 1 hour to melt the starting materials. Subsequently the sample was cooled to 380°C over 96 hours and then kept at that temperature for 10 hours. The samples were left to slowly cool to room temperature over a period of 36 hours. During the slow cooling steps the samples are annealed to reduce the amount of lattice defects and increase long range order. The samples were crushed with a pestle and mortar and x-ray diffraction measurements were performed to check for phase purity.

$CsCdBr_3$

$CsCdBr_3$ doped with Er^{3+} and $Yb^{3+}$was synthesized via a dry-mixture method. The samples were prepared by mixing stoichiometric amounts of dried CsBr, $CdBr_2$, $YbCl_3$ and $ErCl_3$. The powder mixture was put into a quartz ampoule, which was then evacuated and sealed. The ampoule was put into a high frequency furnace and heated to 650°C in 4 hours and kept at that temperature for 4 hours. The sample was then cooled down slowly to 400°C in 10 hours to anneal the sample. The samples that were used for the luminescence measurements were left in the ampoules since $CsCdBr_3$ is slightly hygroscopic. One additional sample was synthesized and removed from the ampoule for x-ray diffraction measurements. The results showed that the samples were single phase. Even though the crystallinity was good, the synthesis method used is not able to exclude all oxygen from the sample and probably some oxygen contamination (O^{2-} on a Br^- site) is present and may locally charge compensate Er^{3+} or Yb^{3+} on a Cd^{2+} site.

5.2.2 Measurements

Diffuse reflectance spectra were measured with a Perkin-Elmer Lambda 950 UV/VIS/IR spectrometer. Emission and excitation spectra were measured with a

SPEX DM3000F spectrofluorometer with a 450 W Xe lamp as the excitation source. Excitation and emission wavelengths were selected with double-grating 0.220 m SPEX 1680 monochromators (1200 l/mm) blazed at 300 and 500 nm, respectively. Emission spectra were also recorded by focusing the emitted light on a fiber guiding the light to a 0.3 m monochromator (Acton Research, Spectra Pro) where the emission light is dispersed by a 150 l/mm grating blazed at 500 nm. The dispersed light was detected with a Princeton Instruments 300i charge coupled device (CCD). Emission and excitation measurements, particularly for the infrared region, were performed using an Edinburgh Instruments FLS920 fluorescence spectrometer. In this spectrofluorometer, the NIR emission (800-1700 nm) is detected with a liquid nitrogen-cooled Hamamatsu R5509-72 PMT. Both the SPEX and Edinburgh fluorescence spectrometers are equipped with an Oxford helium flow cryostat for low temperature measurements. The spectra were not corrected for the instrumental response, unless otherwise indicated. In those cases a radiometrically calibrated DH-2000 halogen lamp from Ocean Optics was used to correct emission spectra for variation in the instrumental response to allow for an absolute comparison of photon fluxes in different spectral regions. Luminescence lifetime measurements with excitation wavelengths between 487-490 nm were performed with the use of a Lambda Physik LPX100 excimer (XeCl) / LPD3000 tunable dye laser system filled with Coumarin 102 dye solution (tunable between 460-510 nm) and a Tektronix 2430 digital oscilloscope. The typical pulse width for the setup is ~20 ns and the repetition rate is 10 Hz. The laser excitation is steered into the sample chamber of the Edinburgh fluorescence spectrometer using a pair of prisms.

5.3 Results and discussion KPb_2Cl_5

5.3.1 Characterization

Samples of KPb_2Cl_5 doped with 1 mol% Er^{3+} and 0, 2, 4, 5, 6 and 10 mol% Yb^{3+} were synthesized. X-ray diffraction measurements gave similar results for all five samples and are consistent with the monoclinic crystal structure of KPb_2Cl_5 [18]. Diffuse reflectance spectra were recorded to confirm if Er^{3+} and Yb^{3+} were incorporated into the host-lattice. From the diffuse reflectance spectra (Fig. 5.2) it can be concluded that both Er^{3+} and Yb^{3+} are present in the samples. However, the absorption strengths for the peaks corresponding to Er^{3+} absorptions (e.g. the $^4I_{15/2} \rightarrow {}^4F_{9/2}$ transition around 600 nm and the $^4I_{15/2} \rightarrow {}^4I_{13/2}$ transition around 1550 nm) differ from sample to sample, even though in the starting mixture the same amount of Er^{3+} (1 mol%) was present. This shows that the Er^{3+} was not built into the lattice equally well for all samples. Furthermore the absorption strength of Er^{3+} varied in diffuse reflectance

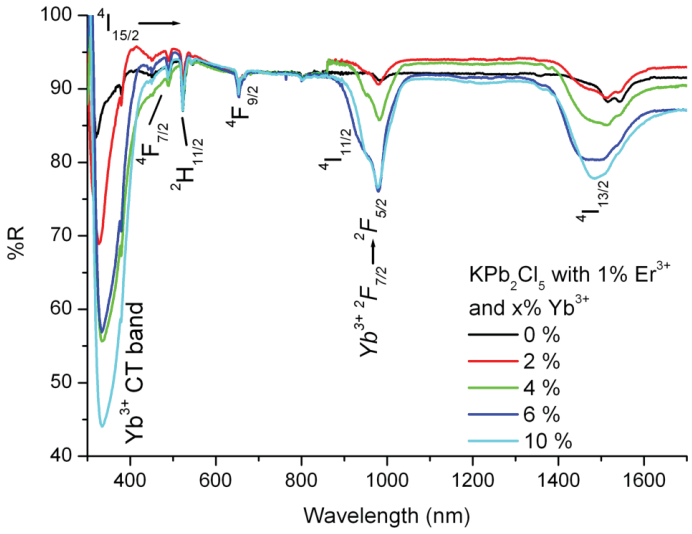

Figure 5.2: Diffuse reflectance spectra for KPb_2Cl_5:Er^{3+}(1%), Yb^{3+}(0, 2, 4, 6 and 10%). Undoped KPb_2Cl_5 was used as a reference.

spectra that were obtained for the same sample, but for different positions in the quartz ampoule.

The strength for the Yb^{3+} absorption around 1000 nm ($^2F_{7/2} \rightarrow {}^2F_{5/2}$ transition) varies according to the Yb^{3+} concentration present in the starting mixtures, except for the sample co-doped with 10% Yb^{3+}. The intensity of the Yb^{3+} absorption around 1000 nm does not seem to increase when the Yb^{3+} concentration is raised from 6 to 10%. This is consistent with the observation by Tkachuk *et al.* that the maximum doping of lanthanide ions into KPb_2Cl_5 is 6% [14].

In the UV range a strong absorption band between 300 and 400 nm is observed which is assigned to a charge transfer (CT) transition from chlorine to Yb^{3+}. The maximum around 350 nm is at somewhat longer wavelength than previously reported for the Cl^--to-Yb^{3+} ligand to metal charge transfer band [19, 20]. As expected for an Yb^{3+} related CT transition the band is strongest for the sample with the highest Yb^{3+} concentration. For the sample without Yb^{3+} as a co-dopant, below 300 nm the onset of the strong host lattice (HL) absorption is observed. The onset of the host lattice absorption is expected around 300 nm [14, 15].

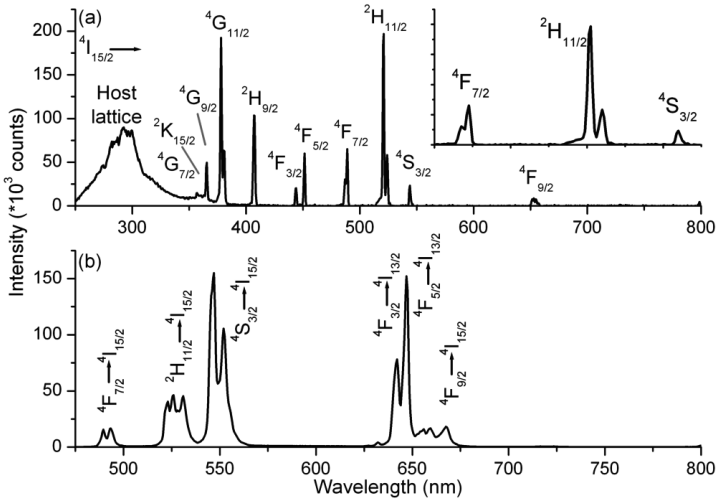

Figure 5.3: (a) High resolution excitation spectrum for KPb_2Cl_5 doped with 1% Er^{3+} and 5% Yb^{3+} for an emission wavelength of 1535 nm ($^4I_{13/2} \rightarrow {}^4I_{15/2}$ transition) measured at 5 K. The inset shows the region of interest (480-550 nm) in more detail (b) Room temperature emission spectrum of KPb_2Cl_5 doped with 1% Er^{3+}. The excitation wavelength is 452 nm ($^4F_{5/2}$ level).

5.3.2 Luminescence spectra

In Fig. 5.3 excitation and emission spectra are shown for KPb_2Cl_5:Er^{3+}, Yb^{3+}. In the low temperature excitation spectrum recorded for the Er^{3+} emission around 1535 nm, sharp excitation lines corresponding to transitions from the $^4I_{15/2}$ ground state to the various excited states of Er^{3+} can be observed. The transitions are assigned in the figure. Below 300 nm the host lattice absorption is observed, indicating that HL excitation is followed by energy transfer to Er^{3+}. The excitation spectrum is consistent with the absorption spectrum reported by Tkachuk *et al.* [14]. For the present work, the spectral region 480-550 nm is particularly relevant. In the inset in Fig. 5.3(a) this region is shown in more detail. Transitions to various crystal field (CF) components of the $^4F_{7/2}$, $^2H_{11/2}$ and $^4S_{3/2}$ levels are observed. The energy difference between the lowest energy $^4F_{7/2}$ CF component and the highest energy $^2H_{11/2}$ CF component is the energy gap that is important for multi-phonon relaxation from the $^4F_{7/2}$ level. Based on the excitation spectrum, the gap is determined to be $\sim$1200 cm^{-1}, which can be bridged by 6 phonons. For a six phonon process, the radiative decay from the $^4F_{7/2}$ level is expected to dominate.

Fig. 5.3(b) shows the emission spectrum for KPb_2Cl_5:Er^{3+} upon excitation in the

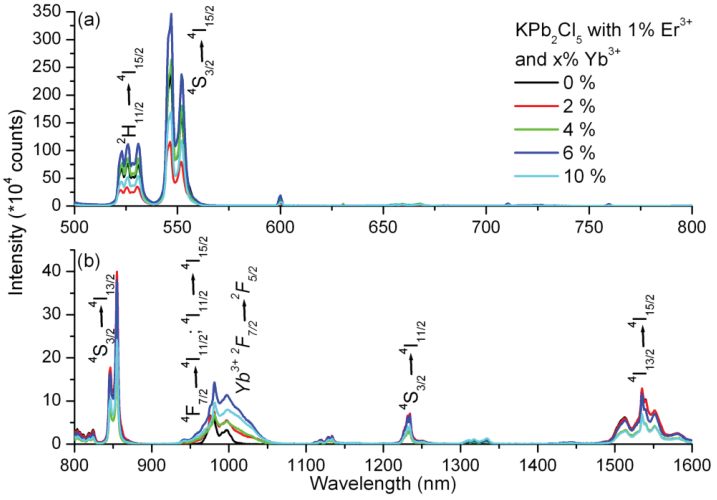

Figure 5.4: Room temperature emission spectra for the (a) visible and (b) infrared part of the spectrum for KPb_2Cl_5:Er^{3+}(1%), Yb^{3+}(0, 2, 4, 6 and 10%) after excitation into the starting level for downconversion ($^4F_{7/2}$ level, 489 nm).

$^4F_{5/2}$ level, just above the $^4F_{7/2}$ level. In the emission spectrum, emission from the $^4F_{7/2}$ level is observed around 490 nm, showing that emission from this level can be observed in this host lattice and that downconversion may be possible. The strongest emission lines originate from the $^2H_{11/2}$/$^4S_{3/2}$ levels which indicates that, in spite of the gap of ~1200 cm^{-1}, multi-phonon relaxation from $^4F_{7/2}$ to $^2H_{11/2}$ occurs and is faster than radiative decay from the $^4F_{7/2}$ level. Based on the energy gap law and experimental results, a rule of thumb predicts that radiative decay and multi-phonon relaxation can compete when the gap is five times the phonon energy, and that for a larger gap radiative decay dominates [12]. The present results indicate that for Er^{3+} in KPb_2Cl_5 the relaxation from the $^4F_{7/2}$ level over a six-phonon gap is faster than radiative decay and may limit the downconversion efficiency. The observation of fast multi-phonon relaxation is in agreement with the findings of Tkachuk *et al.*, who reported a radiative (calculated) life time of 153 μs for the $^4F_{7/2}$ level, but found the actual life time to be much shorter, ~10 μs, due to fast non-radiative relaxation.

To analyze if downconversion occurs and to gain insight in the downconversion efficiency, emission spectra were recorded under excitation in the $^4F_{7/2}$ level (489 nm). In Fig. 5.4 the emission spectra for the visible (a) and infrared (b) part of the spectrum for KPb_2Cl_5 with 1 mol% Er^{3+} and 0, 2, 4, 6 and 10 mol% Yb^{3+} after excitation into the $^4F_{7/2}$ level are shown. The spectra were measured under identical conditions so

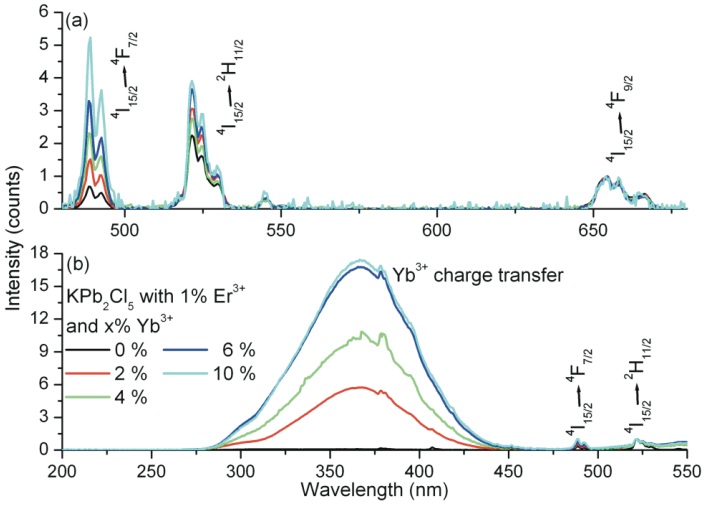

Figure 5.5: Room temperature excitation spectra for emission at 980 nm in KPb_2Cl_5:Er^{3+}(1%), Yb^{3+}(0, 2, 4, 6 and 10%) in the (a) 480-680 nm range and (b) 200-550 nm range.

that the intensities of the emissions may be compared. In the sample doped with Er^{3+} only, excitation in the Er^{3+} $^4F_{7/2}$ level yields emission from the $^2H_{11/2}$, $^4S_{3/2}$ and $^4F_{9/2}$ levels to the $^4I_{15/2}$ level in the visible and emission from the $^4S_{3/2}$, $^4F_{7/2}$ and $^4I_{13/2}$ levels to higher energy ^4I_J (J = 9/2, 11/2, 13/2) levels in the infrared. The intensity of the Er^{3+} emission decreases slightly and the Yb^{3+} emission intensity increases upon increasing Yb^{3+} concentration. However, like for the Er^{3+}–Yb^{3+}couple in a fluoride host lattice, energy transfer from the $^4S_{3/2}$ level of Er^{3+} to Yb^{3+} is inefficient [10], and even at high Yb^{3+} concentrations the (visible) Er^{3+} emission dominates while in all samples the Yb^{3+} emission around 980 nm is weak, even though it does increase with Yb^{3+} concentration. The inefficient quenching of the $^4S_{3/2}$ emission from Er^{3+} by Yb^{3+} is evident from the energy level diagram (Fig. 5.1): there is no energy level for Er^{3+} at ~10 000 cm^{-1} below the $^4S_{3/2}$ level.

Convincing evidence for the occurrence of downconversion from the $^4F_{7/2}$ level is presented in Fig. 5.5. Excitation spectra are shown for the Yb^{3+} emission around 1000 nm. At this emission wavelength also Er^{3+} emission originating from the $^4I_{11/2} \rightarrow {}^4I_{15/2}$ transition is monitored. The spectra are scaled to the $^4I_{15/2} \rightarrow {}^4F_{9/2}$ excitation line around 650 nm. Upon raising the Yb^{3+} concentration a slight increase in the relative intensity of the $^4I_{15/2} \rightarrow {}^4S_{3/2}$, $^2H_{11/2}$ lines is observed. For both the $^4S_{3/2}$/$^2H_{11/2}$ and the $^4F_{9/2}$ level there is no path for resonant energy transfer to Yb^{3+}

and thus the excitation lines remain weak upon raising the Yb^{3+} concentration. However, for the transition to the $^4F_{7/2}$ level the relative intensity rapidly increases upon raising the Yb^{3+} concentration, indicating that the $^2F_{5/2}$ level of Yb^{3+} is efficiently populated by energy transfer from this Er^{3+} level. In the sample co-doped with 10% Yb^{3+} the excitation line corresponding to the $^4I_{15/2} \rightarrow {}^4F_{7/2}$ transition becomes even stronger than the transition to the $^2H_{11/2}$ level, even though the absorption strength for the $^4I_{15/2} \rightarrow {}^2H_{11/2}$ transition is more than six times stronger (Fig. 2 of Ref. [14]). This clearly shows that energy transfer through the downconversion scheme depicted in Fig. 5.1 occurs. The low overall efficiency of Yb^{3+} emission and the strong $^4S_{3/2}$ emission from Er^{3+} even for the highest Yb^{3+} concentration (10%) reflect that the transfer efficiency from the $^4F_{7/2}$ level is low in comparison with multi-phonon relaxation. A quantitative analysis of the efficiency based on the emission intensities is difficult (due to the different set-ups used for detection of the visible and the infrared emission and the fact that the Yb^{3+} emission will be partly quenched by concentration quenching). Based on the present results an upper limit of 10% can be estimated, which shows that even though downconversion occurs, the efficiency is too low for practical application.

In Fig. 5.5(b) the higher energy part of the excitation spectrum of the Yb^{3+} emission is plotted along with the lines observed in Fig. 5.5(a). In the UV part of the spectrum a very strong excitation band is observed around 360 nm. This band is assigned to the Cl^--Yb^{3+} CT transition. Excitation in this level results in feeding of the $^2F_{5/2}$ excited state of Yb^{3+} and emission from this level. Clearly, direct excitation in the strongly absorbing CT state is the most efficient way to feed the Yb^{3+} emission in the IR but is not able to generate two NIR photons per absorbed UV photon. In Fig. 5.6(a) emission spectra for KPb_2Cl_5:Er^{3+}(1%), Yb^{3+}(4%) are plotted for different excitation wavelengths. This overview shows which emissions are most efficiently excited at these wavelengths. In Fig. 5.6(b) the dependence of the relative intensity of the 1000 nm emission (Yb^{3+} and Er^{3+} emission) is given for these six excitation wavelengths as a function of Yb^{3+} concentration. For 522 nm excitation, the increase of the 1000 nm emission intensity with increasing Yb^{3+} concentration is the weakest, consistent with the inefficient energy transfer from the $^4S_{3/2}$ level of Er^{3+} to the $^4F_{5/2}$ level of Yb^{3+}. For 489 and 452 nm excitation there is a stronger and continuous increase which is explained by an increased efficiency of energy transfer to Yb^{3+} upon excitation in the $^4F_{7/2}$ or $^4F_{5/2}$ level of Er^{3+} through downconversion. The most spectacular increase is observed for excitation in the CT band of Yb^{3+} at 407 and 379 nm. At the highest Yb^{3+} concentrations, there is a small decrease in the 1000 nm emission intensity, probably because the absorption is close to saturation and the emission is partly quenched by concentration quenching. Excitation in the host lattice, 305 nm,

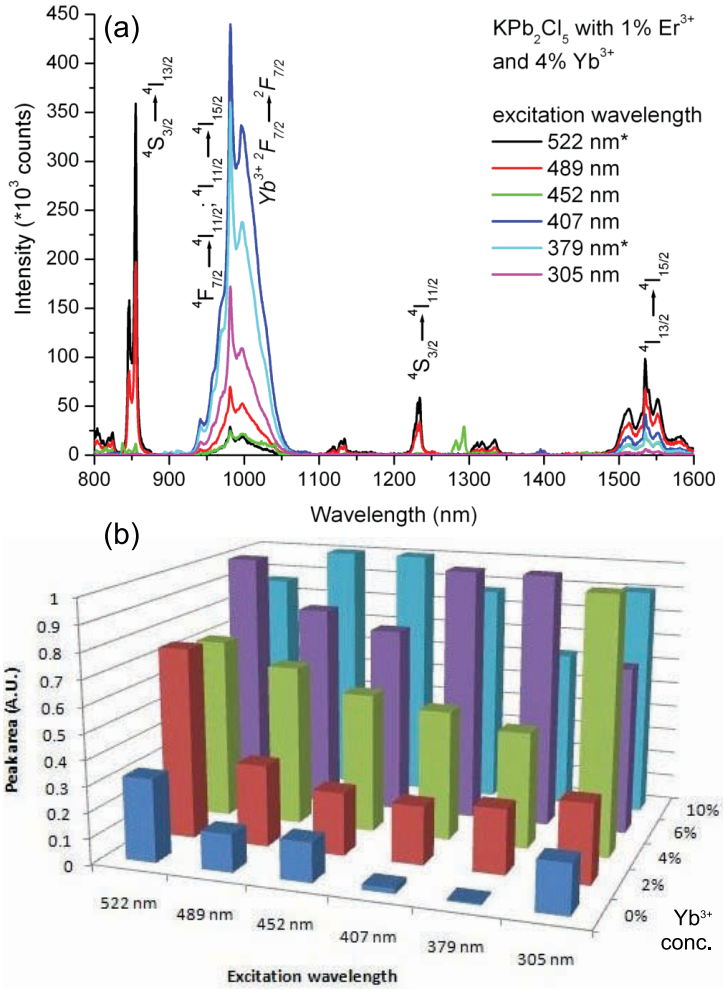

Figure 5.6: (a) Infrared emission spectra for different excitation wavelengths for KPb_2Cl_5:Er^{3+}(1%), Yb^{3+}(4%) measured at room temperature. The stars indicate measurements where the emission slit was half of that for the other measurements. (b) Bar diagram of the integrated peak area around 980 nm (Yb^{3+} $^2F_{7/2} \rightarrow {}^2F_{5/2}$ emission), for different Yb^{3+} concentrations at six different excitation wavelengths. The peak area for the 980 nm emission was divided by the integrated area of the emission peak for the Er^{3+} $^4I_{13/2} \rightarrow {}^4I_{15/2}$ emission (~1550 nm). For each excitation wavelength the largest peak area was then set to 1, to create an overview of the effect of the Yb^{3+} concentration and the excitation wavelength on the relative Yb^{3+} emission intensity.

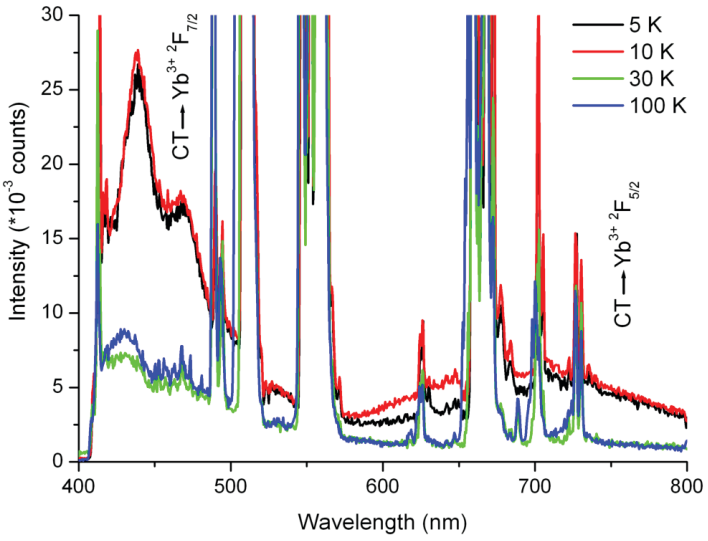

Figure 5.7: Emission spectra of KPb_2Cl_5:Er^{3+}(1%), Yb^{3+}(2%) for the visible part of the spectrum measured at different temperatures. The excitation wavelength is 379 nm and the spectra are strongly magnified to observe weak emission bands around 430 and 700 nm.

always gives rise to 1000 nm emission and the rapid increase suggests that both the $^4I_{11/2}$ level of Er^{3+} and the $^2F_{5/2}$ level of Yb^{3+} are fed by direct transfer from the host lattice to these low lying energy levels.

Finally, in Fig. 5.7 emission spectra for excitation into the CT band of Yb^{3+} are shown. At 5 K two weak emission bands are observed: a structured band around 430 nm and a band around 700 nm. Upon raising the temperature from 10 to 30 K both emission bands are quenched. The energy separation between the emission bands is ~9000 cm^{-1}. This emission is assigned to charge transfer emission from the excited CT state of Yb^{3+}-Cl^-. The energy separation between the two bands is consistent with the expected splitting of ~10 000 cm^{-1} for transitions from the CT state to both the $^2F_{5/2}$ and $^2F_{7/2}$ multiplets of Yb^{3+} and also the Stokes shift (~5000 cm^{-1}) and low quenching temperature are commonly observed for Yb^{3+} charge transfer luminescence [20]. The structure in the emission band around 430 nm arises from transitions to different crystal field components of the $^2F_{7/2}$ ground state of Yb^{3+}. As far as we are aware, this example represents the first observation of charge transfer luminescence for Yb^{3+} in a chloride.

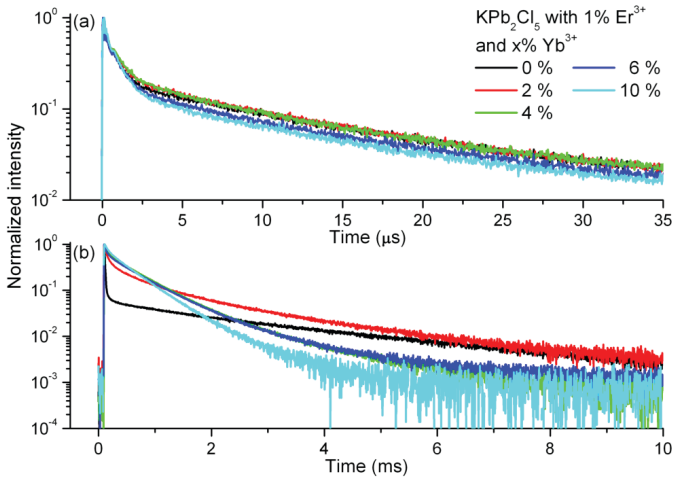

Figure 5.8: Luminescence decay curves of (a) Er^{3+} $^4F_{7/2} \rightarrow {}^4I_{15/2}$ emission (491 nm) and (b) Yb^{3+} $^2F_{7/2} \rightarrow {}^2F_{5/2}$ emission (998 nm) in KPb_2Cl_5:Er^{3+}(1%), Yb^{3+}(0, 2, 4, 6 and 10%) measured at room temperature, for excitation in the Er^{3+} $^4F_{7/2}$ level (487 nm).

5.3.3 Luminescence decay

To gain further insight in the energy transfer processes between Er^{3+} and Yb^{3+}, luminescence decay curves were recorded. Lifetime measurements for Er^{3+} $^4F_{7/2} \rightarrow {}^4I_{15/2}$ emission (λ_m = 491 nm) for KPb_2Cl_5 with 1% Er^{3+} and between 0-10% Yb^{3+} measured at room temperature upon excitation in the Er^{3+} $^4F_{7/2}$ level (487 nm) are shown in Fig. 5.8(a). Similar measurements for Yb^{3+} $^2F_{7/2} \rightarrow {}^2F_{5/2}$ emission (λ_m = 998 nm) are depicted in Fig. 5.8(b). The luminescence decay curves in Fig. 5.8(a) show a close to bi-exponential decay behavior. For the sample without Yb^{3+} co-dopant, the initial part of the decay curve yields a fast decay time of ~5.3 µs and a long time component of ~20 µs. The fast component is assigned to fast quenching of the $^4F_{7/2}$ emission in pairs of Er^{3+} through cross-relaxation. Due to the need for charge compensation (Er^{3+} on a Pb^{2+} site) pair formation may be favored. The long time component of 20 µs is close to the 10 µs reported by Tkachuk *et al.* for the life time of the $^4F_{7/2}$ level of Er^{3+} [14]. The calculated (radiative) decay time is much longer (153 µs). The difference is explained by fast multi-phonon relaxation. Based on a radiative decay time of 153 µs and an experimental decay time of 20 µs, the multi-phonon relaxation rate is $4.3 \cdot 10^4$ s^{-1}.

The average lifetime of the fast component of the $^4F_{7/2}$ emission decreases slightly

(from 5.2 to 3.7 μs) as the Yb^{3+} concentration is raised from 0 to 10%. As the concentration of Yb^{3+} is increased energy transfer becomes more likely because more Er^{3+}-ions will have Yb^{3+}-ions close enough for energy transfer, leading to a shorter lifetime. However, the weak dependence of the decay time on the Yb^{3+} concentration shows that energy transfer from the Er^{3+} $^4F_{7/2}$ level to Yb^{3+} is not very efficient. The average lifetime of the Er^{3+} $^4F_{7/2}$ emission for Er^{3+}-ions that have no Yb^{3+} neighbors close enough for energy transfer is approximately 20 μs for all samples.

The decay curves for the emission at 998 nm in Fig. 5.8(b) contain a fast component, especially clear for the sample without Yb^{3+}, and a slow component. For the sample without Yb^{3+} the fast component is ascribed to ~1000 nm emission from a higher energy level of Er^{3+} while the slow component reflects the decay time for the $^4I_{11/2} \rightarrow {}^4I_{15/2}$ emission. The lifetime of ~3 ms is in agreement with the results of Tkachuk *et al.* for the $^4I_{11/2} \rightarrow {}^4I_{15/2}$ emission. Upon raising the Yb^{3+} concentration, the decay curves become non-exponential and faster. Fitting to a two exponential decay curve yields a fast component around 500 μs that increases in relative contribution and a slow component that decreases from 3 ms to 1 ms. The fast component is assigned to $^2F_{5/2}$ emission from Yb^{3+}. For the sample co-doped with 2% Yb^{3+} the lifetime of the Yb^{3+} $^2F_{5/2}$ emission is around 590 μs. This lifetime decreases as the Yb^{3+} concentration is raised: for the sample with 10% Yb^{3+} it is around 465 μs. The decrease can be explained by concentration quenching at higher Yb^{3+} concentrations. The observation that the slow component (which is again assigned to the Er^{3+} $^4I_{11/2} \rightarrow {}^4I_{15/2}$ emission, as for the sample without Yb^{3+}) decreases from 3 to 1 ms indicates that there is energy transfer from the $^4I_{11/2}$ level of Er^{3+} to the $^2F_{5/2}$ level of Yb^{3+}.

The present results show that compared to the efficient energy transfer observed previously for the Pr^{3+}–Yb^{3+} [5, 21], Tm^{3+}–Yb^{3+} [6] and Tb^{3+}–Yb^{3+} [22–24] couples the energy transfer efficiency from Er^{3+} to Yb^{3+} is low. This is confirmed by luminescence decay measurements. For the efficient downconversion systems a rapid decrease of the luminescence decay times is observed upon raising the Yb^{3+} concentration. For the Er^{3+}–Yb^{3+}couple the life times do not decrease drastically in line with the low downconversion efficiency observed in the luminescence spectra.

5.4 Results and discussion $CsCdBr_3$

In chapter 4 the potential of the Er^{3+}–Yb^{3+} couple for downconversion was investigated in a fluoride host material and in the previous section results have been shown for the Er^{3+}–Yb^{3+} couple in KPb_2Cl_5. In both types of host lattices efficient DC

was not possible due to fast multi-phonon relaxation from the $^4F_{7/2}$ level, indicating that a host with an even smaller phonon energy is needed. $CsCdBr_3$ has a maximum phonon energy of 180 cm^{-1} and the energy difference between the Er^{3+} $^4F_{7/2}$ level and the next lower level ($^2H_{11/2}$) is typically around 1300 cm^{-1} [14, 16, 17]. Therefore, in the $CsCdBr_3$ host lattice at least 7 phonons are needed to bridge the energy gap. This makes non-radiative relaxation unlikely, so that DC with the Er^{3+}–Yb^{3+} couple should be possible in this host lattice. In this section preliminary results are presented for downconversion in $CsCdBr_3$:Er^{3+}, Yb^{3+}.

Samples of $CsCdBr_3$ doped with 1% Er^{3+} and 0, 2 and 5 mol% Yb^{3+} were synthesized. X-ray diffraction measurements gave similar results for all three samples. The crystal structure was consistent with the hexagonal structure of $CsCdBr_3$ [25, 26]. Emission spectra for $CsCdBr_3$:Er^{3+}(1%) after excitation into the Er^{3+} $^4F_{7/2}$ level (Fig. 5.9, black line) show peaks for emission from the Er^{3+} $^4F_{7/2}$ (~495 nm), $^2H_{11/2}$ (~525 nm) and $^4S_{3/2}$ (~550 nm) levels in the visible and emissions from transitions from the $^4I_{11/2}$ and $^4I_{13/2}$ levels to the $^4I_{15/2}$ ground state (~985 and ~1540 nm respectively) in the IR. The same peaks are also observed for the co-doped samples. In addition to the peaks for Er^{3+} emission there is also a peak around 1000 nm for emission from Yb^{3+} ($^2F_{7/2} \rightarrow {}^2F_{5/2}$ transition) for the co-doped samples. This indicates that there is energy transfer from Er^{3+} to Yb^{3+}, since excitation took place in the Er^{3+} $^4F_{7/2}$ level. As the Yb^{3+} concentration is increased the intensity of the Er^{3+} emission decreases: at higher Yb^{3+} concentrations more Er^{3+}-ions have Yb^{3+} neighbors, so energy transfer should be more efficient. The energy transfer efficiency is still limited by multi-phonon relaxation from the Er^{3+} $^4F_{7/2}$ to the $^4S_{3/2}$ level, since emission from the $^2H_{11/2}$ and $^4S_{3/2}$ levels is observed for the samples co-doped with 5% Yb^{3+}. The Yb^{3+} emission intensity is highest for the sample co-doped with only 2% Yb^{3+}.

Fig. 5.10 shows decay curves of Er^{3+} $^4F_{7/2}$ emission (494 nm) for $CsCdBr_3$ doped with 1% Er^{3+} and 0, 2 and 5 mol% Yb^{3+} after excitation into the Er^{3+} $^4F_{7/2}$ level (490 nm). As the Yb^{3+} concentration is increased the lifetime of the decay decreases due to energy transfer. For the samples co-doped with Yb^{3+} a non-exponential decay curve is expected: the non-exponential character of the decay curves then reflects the different distributions of Yb^{3+}-ions around different Er^{3+} ions, giving rise to a large variation in the energy transfer rates between Er^{3+} and Yb^{3+}-ions. For the sample doped with only Er^{3+} the decay curve already shows a non-exponential character, which could be due to energy transfer between neigboring Er^{3+}-ions, which are incorporated as pairs in $CsCdBr_3$. Also oxygen contamination may cause the faster initial decay for Er^{3+}-ions locally charge compensated by O^{2-} on a Br^- site. This makes further analysis of the decay curves problematic.

Fig. 5.11 shows the emission spectra for the three samples upon excitation into

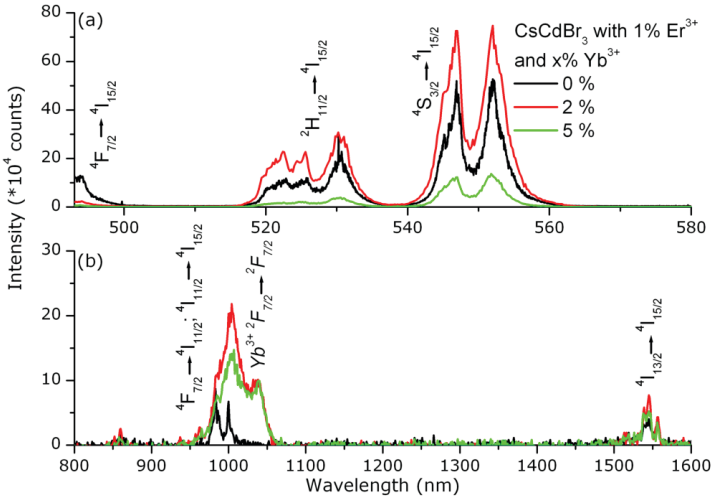

Figure 5.9: Room temperature emission spectra of $CsCdBr_3$:Er^{3+}(1%), Yb^{3+}(0, 2, 5%) in the (a) visible and (b) infrared. The excitation wavelength is 490 nm ($^4F_{7/2}$ level).

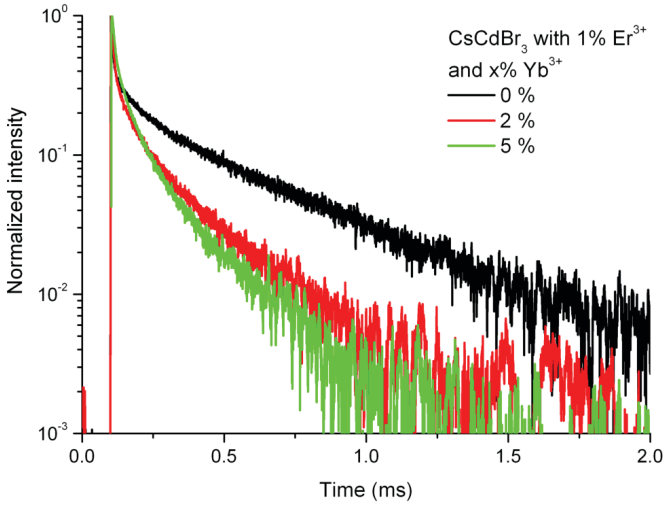

Figure 5.10: Luminescence decay curves for the $^4F_{7/2}$ emission in $CsCdBr_3$:Er^{3+}(1%), co-doped with 0, 2, or 10% Yb^{3+} measured at room temperature. The excitation wavelength is 490 nm (into the $^4F_{7/2}$ level) and the emission wavelength is 494 nm ($^4F_{7/2} \rightarrow {}^4I_{15/2}$).

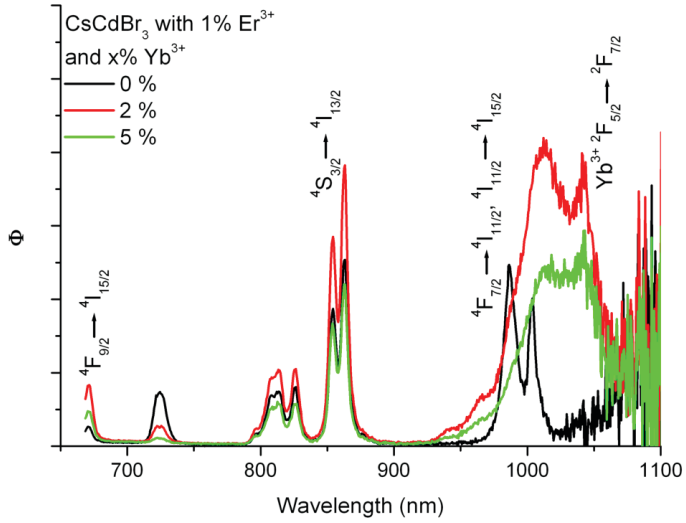

Figure 5.11: Room temperature emission spectra of $CsCdBr_3$:Er^{3+}(1%), Yb^{3+}(0, 2, 5%). The excitation wavelength is 490 nm ($^4F_{7/2}$ level). The spectra are recorded under identical conditions and corrected for instrumental response. Φ gives the photon flux per constant wavelength interval.

the Er^{3+} $^4F_{7/2}$ level (490 nm). The spectra are corrected for instrumental response so that the areas of integrated emission peaks represent the total photon flux and can be compared quantitatively. An estimate of the conversion efficiency of visible to NIR can be obtained from the ratio of the integrated emission intensity of Er^{3+} luminescence (between 500 and 800 nm) for a sample without Yb^{3+} to the integrated NIR emission intensity (between 800 and 1100 nm) for a sample co-doped with Er^{3+} and Yb^{3+}. Care was taken to conduct the luminescence measurements under identical conditions as much as possible. However, consistent alignment of the quartz ampoules containing the samples was not easy and (small) differences in alignment lead to an uncertainty in the obtained integrated emission intensities. In this way a visible to NIR conversion efficiency of 34% was obtained for the sample co-doped with 2 mol% Yb^{3+}.

In this section some preliminary results have been given for DC with the Er^{3+}–Yb^{3+} couple in $CsCdBr_3$. Further measurements are necessary to gain a better understanding of the energy transfer from Er^{3+} to Yb^{3+} in these samples. A better understanding of the decay curves could be beneficial. To achieve this Y^{3+} could be

added to the samples, so that less Er^{3+}–Er^{3+} pairs can form. This would lead to less cross relaxation between Er^{3+}-ions which simplifies the analysis of the decay curves. Also higher quality samples (single crystals grown from purified starting materials) are required to exclude the role of oxygen impurities.

5.5 Conclusions

Luminescence spectra (excitation and emission) and luminescence decays curves have been recorded for KPb_2Cl_5:Er^{3+}(1%) co-doped with 0, 2, 4, 6, and 10% Yb^{3+} to investigate the potential of the Er^{3+}–Yb^{3+}couple in a chloride host material for downconversion. The results show that the desired downconversion process from the $^4F_{7/2}$ level (the inverse of the efficient upconversion process) has a very low efficiency due to fast multi-phonon relaxation from the $^4F_{7/2}$ to the $^4S_{3/2}$ level via the intermediate $^2H_{11/2}$ level. Based on the energy gap between the $^4F_{7/2}$ and the $^2H_{11/2}$ level (~1200 cm^{-1}) this is unexpected, since this host has a phonon energy of 200 cm^{-1}. Analysis of luminescence decay curves confirms that energy transfer from Er^{3+} to Yb^{3+} is inefficient. In a host with an even lower phonon energy ($CsCdBr_3$) $^4F_{7/2}$ emission and energy transfer from the Er^{3+} $^4F_{7/2}$ level to Yb^{3+} does occur, but the visible to NIR conversion efficiency is still low. Further experiments are in progress to realize higher downconversion efficiencies for the Er^{3+}–Yb^{3+} couple in bromides.

In the diffuse reflectance spectra a broad band for excitation into the Yb^{3+}-Cl^- charge transfer band was observed between 300 and 400 nm. Excitation in this LMCT band results in two broad emission bands centered around 430 and 700 nm at temperatures below 30 K. The emission is assigned to luminescence from the Cl^--Yb^{3+} charge transfer state which can also feed the Yb^{3+} $^2F_{5/2}$ level, followed by Yb^{3+} $^2F_{5/2} \rightarrow {}^2F_{7/2}$ emission around 980 nm.

References

[1] W. Shockley and H. Queisser, *Detailed balance limit of efficiency of p-n junction solar cells*, J. Appl. Phys. **32**, 510 (1961).

[2] F. Auzel, *Upconversion and anti-Stokes processes with f and d ions in solids*, Chem. Rev. **104**, 139 (2004).

[3] R. Wegh, H. Donker, K. Oskam, and A. Meijerink, *Visible quantum cutting in $LiGdF_4$:Eu^{3+} through downconversion*, Science **283**, 663 (1999).

[4] P. Vergeer, T. Vlugt, M. Kox, M. den Hertog, J. van der Eerden, and A. Meijerink, *Quantum cutting by cooperative energy transfer in $Yb_xY_{1-x}PO_4$:Tb^{3+}*, Phys. Rev. B. **71**, 014119 (2005).

[5] G. Lakshminarayana, H. Yang, S. Ye, Y. Liu, and J. Qiu, *Cooperative downconversion luminescence in Pr^{3+}/Yb^{3+}:SiO_2-Al_2O_3-BaF_2-GdF_3 glasses*, J. Mater. Res. **23**, 3090 (2008).

[6] G. Lakshminarayana, H. Yang, S. Ye, Y. Liu, and J. Qiu, *Co-operative downconversion luminescence in Tm^{3+}/Yb^{3+}:SiO_2-Al_2O_3-LiF-GdF_3 glasses*, J. Phys. D: Appl. Phys. **41**, 175111 (2008).

[7] F. Auzel, C. R. Acad. Sci. (Paris) **262**, 1016 (1966).

[8] F. Auzel, C. R. Acad. Sci. (Paris) **263**, 819 (1966).

[9] F. Auzel, Ann. Telecom. (Paris) **24**, 363 (1969).

[10] B. M. v. d. E. L. Aarts and A. Meijerink, *Downconversion for solar cells in $NaYF_4$:Er,Yb*, J. Appl. Phys. **106**, 023522 (2009).

[11] J. Suyver, J. Grimm, K. Krämer, and H. Güdel, *Highly efficient near-infrared to visible upconversion process in $NaYF_4$:Er^{3+},Yb^{3+}*, J. Lumin. **114**, 53 (2005).

[12] J. Suyver, A. Aebischer, D. Biner, P. Gerner, J. Grimm, S. Heer, K. Krämer, C. Reinhard, and H. Güdel, *Novel materials doped with trivalent lanthanides and transition metal ions showing near-infrared to visible photon conversion*, Opt. Mat. **27**, 1111 (2005).

[13] J. Suyver, J. Grimm, M. van Veen, D. Biner, K. Krämer, and H. Güdel, *Upconversion spectroscopy and properties of $NaYF_4$ doped with Er^{3+}, Tm^{3+} and/or Yb^{3+}*, J. Lumin. **117**, 1 (2006).

[14] A. Tkachuk, S. Ivanova, L. Isaenko, A. Yellisseyev, M. Joubert, F. Guyot, and S. Payne, *Spectroscopic studies of erbium-doped potassium-lead double chloride crystals of KPb_2Cl_5:Er^{3+}: 1. Optical spectra and relaxation of excited states of the erbium ion in potassium-lead double chloride crystals*, Opt. Spectro. **95**, 722 (2003).

[15] V. Pustovarov, I. Ogorodnikov, N. Bastrikova, A. Smirnov, L. Isaenko, and A. Eliseev, *Low-temperature time-resolved spectroscopy of APb_2X_5 crystals ($A \equiv K, Rb$; $X \equiv Cl, Br$)*, Opt. Spectro. **101**, 234 (2006).

[16] X. Zhou, P. Tanner, and D. Faucher, *Electronic spectra and crystal field analysis of Er^{3+} in Cs_2NaErF_6*, J. Phys. Chem. C **111**, 683 (2007).

[17] U. Hömmerich, E. Nyein, and S. Trivedi, *Crystal growth, upconversion, and infrared emission properties of Er^{3+}-doped KPb_2Br_5*, J. Lumin. **113**, 100 (2005).

[18] A. Merkulov, L. Isaenko, V. Pashkov, V. Mazur, A. Virovets, and D. Naumov, *Crystal structure of KPb_2Cl_5 and KPb_2Br_5*, J. Struct. Chem. **46**, 103 (2005).

[19] M. Nikl, A. Yoshikawa, and T. Fukuda, *Charge transfer luminescence in Yb^{3+}-containing compounds*, Opt. Mat. **26**, 545 (2004).

[20] L. van Pieterson, M. Heeroma, E. de Heer, and A. Meijerink, *Charge transfer luminescence of Yb^{3+}*, J. Lumin. **91**, 177 (2000).

[21] B. van der Ende, L. Aarts, and A. Meijerink, *Near-infrared quantum cutting for photovoltaics*, Adv. Mat. **21**, 3073 (2009).

[22] J. Yuan, X. Zeng, J. Zhao, Z. Zhang, H. Chen, and X. Yang, *Energy transfer mechanisms in Tb^{3+},Yb^{3+} codoped Y_2O_3 downconversion phosphor*, J. Phys. D: Appl. Phys. **41**, 105406 (2008).

[23] Q. Zhang, C. Yang, and Y. Pan, *Cooperative quantum cutting in one-dimensional (Yb_xGd_{1-x})$Al_3(BO_3)_4$:Tb^{3+} nanorods*, Appl. Phys. Lett. **90**, 021107 (2007).

[24] X. Huang and Q. Zhang, *Efficient near-infrared down conversion in Zn_2SiO_4:Tb^{3+},Yb^{3+} thin-films*, J. Appl. Phys. **105**, 053521 (2009).

[25] P. Ren, J. Qin, and C. Chen, *A novel nonlinear optical crystal for the IR region: noncentrosymmetrically crystalline CsCdBr and its properties*, Inorg. Chem. **42**, 8 (2003).

[26] G. McPherson and K. Devany, *Spectroscopic properties of vanadium(II), manganese(II), and nickel(II) in crystals of cesium tribromocadmate*, Inorg. Chem. **16**, 1565 (1977).

6

Downconversion with Nd^{3+}, Yb^{3+} in YF_3 and $CsCdBr_3$

Abstract

Energy losses inherent to the conversion of sunlight to electricity in solar cells are mainly due to the so-called spectral mismatch: low energy photons are not absorbed while the energy of high energy photons is only partly used by the solar cell. The losses can be significantly reduced by adapting the solar spectrum. A promising avenue is the use of a downconversion material where one higher energy visible (blue-green) photon is 'cut' into two lower energy near-infrared photons that both can be used by the solar cell. Here the efficiency of downconversion for the Nd^{3+}–Yb^{3+} couple in YF_3 and $CsCdBr_3$ is studied to investigate if efficient two-step energy transfer occurs from the $^4G_{9/2}$ level of Nd^{3+} (situated around 21 000 cm^{-1} or 470 nm), exciting two neighboring Yb^{3+} to the $^2F_{5/2}$ level (around 10 000 cm^{-1} or 1000 nm). Optical measurements of samples co-doped with Nd^{3+} and Yb^{3+} show that there is efficient energy transfer from Nd^{3+} to Yb^{3+}. In YF_3:Nd^{3+}, Yb^{3+} downconversion from the $^4G_{9/2}$ level does not occur due to fast multi-phonon relaxation. Relaxation from this level to lower energy levels populates the $^4F_{3/2}$ level of Nd^{3+} from which efficient one-step energy transfer to Yb^{3+} occurs. Analysis of the luminescence decay curves of YF_3:Nd^{3+}co-doped with different Yb^{3+} concentrations using Monte Carlo simulations reveals a high nearest neighbor transfer rate ($3.3 \cdot 10^5$ s^{-1}) through a dipole-dipole interaction mechanism. Downconversion is observed starting from the $^4D_{3/2}$ level (situated in the UV, around 28 000 cm^{-1} or 360 nm) with an estimated quantum efficiency up to 140%. For application in solar cells this UV to 2 NIR photon downconversion will only result in a marginal reduction of spectral mismatch losses. Efficient visible to NIR conversion from the $^4G_{9/2}$ level is observed in $CsCdBr_3$ co-doped with Nd^{3+} and Yb^{3+}. The lower phonon energies in $CsCdBr_3$ suppress multi-phonon relaxation from the $^4G_{9/2}$ level and energy transfer from this level to neighboring Yb^{3+}-ions is efficient. Based on these results it is concluded that bromide materials are promising for efficient downconversion with Nd^{3+}–Yb^{3+}.

6.1 Introduction

The theoretical maximum conversion efficiency of solar cells is 30% [1]. A large part of the energy losses that limit the efficiency is related to the spectral mismatch: photons with energy smaller than the band-gap (E_g) will not be absorbed (sub-band-gap transmission) and a large part of the energy of photons with energy larger than the band-gap is lost as heat (thermalization losses). There are two ways to reduce the energy losses related to the spectral mismatch: either the solar cell can be adapted to use the solar spectrum more efficiently, or the solar spectrum can be adapted before

it is absorbed by the solar cell. Solar cells can be adapted to make better use of the spectrum by combining multiple semiconductor materials with different band-gaps, each converting a different part of the solar spectrum with high efficiency. This approach has been successfully applied in tandem solar cells, and energy efficiencies over 40% have been reported [2].

There are two ways to adapt the solar spectrum before it is absorbed by the solar cell. The first option is to add two lower-energy photons (that are otherwise transmitted) to obtain one higher energy photon that can be absorbed by the solar cell. This process is known as upconversion (UC) and is especially useful for solar cells with a large band-gap where transmission losses dominate. The second option is to split one higher energy photon to obtain two photons with a smaller energy. Each of these photons can subsequently be absorbed by the solar cell and generate an electron-hole pair. This is known as downconversion (DC) and is most beneficial for solar cells with a smaller band-gap where thermalization losses are the major loss factor. This process is also known as quantum cutting because one photon is 'cut' into two smaller energy photons. Lanthanide ions are very well suited to use for both DC and UC because they have a rich energy level structure that allows for efficient spectral conversion. There are many examples of efficient up- and downconversion using lanthanides, either with one type of lanthanide ion or a pair of lanthanide ions [3,4].

The effect of using either up- or downconversion materials in combination with solar cells has been modeled by Trupke *et al*. [5–7]. When a solar cell with a band gap of 1.1 eV is combined with an ideal downconverter material in front of the cell (splitting every photon above 2 E_g into two photons that can be absorbed and both generate an electron-hole pair), an efficiency of up to 40% is possible [5]. An upper limit of approximately 50% can be reached when a solar cell with a band-gap of ~2 eV is combined with an ideal upconverter at the rear of the cell [6, 7]. UC is a nonlinear process: for the two-step UC process (where two photons are added to obtain one photon with a larger energy) the UC light intensity I_{UC} is proportional to square of the incident light intensity I_i. As a result, high conversion efficiencies are only obtained at sufficiently high excitation density which can be easily realized using lasers, but will require strong concentration of sunlight.

The most efficient UC is realized using lanthanide ions [3]. An example of a particularly efficient upconverting couple is Er^{3+}–Yb^{3+}. Under high power laser excitation an efficiency of around 50% has been reported for the conversion of NIR (~1000 nm) to visible light in $NaYF_4$:Er^{3+}, Yb^{3+} [8]. The feasibility of upconversion for solar cells was demonstrated using NIR upconversion in $NaYF_4$ doped with Er^{3+}, which was applied to the rear of a silicon solar cell and shown to convert 1400-1500 nm NIR to photons that can be absorbed by the c-Si solar cell, albeit with low

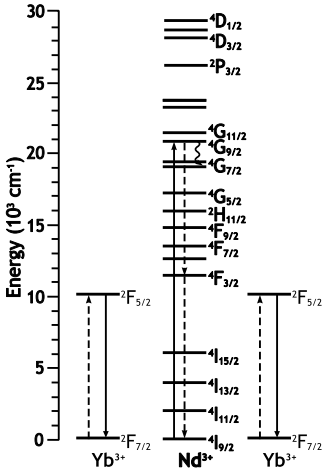

Figure 6.1: Schematic representation of the desired mechanism for downconversion with the Nd^{3+}–Yb^{3+} couple. Nd^{3+} is excited into the $^4G_{9/2}$ state. Part of the energy is transferred to Yb^{3+} via cross relaxation: Nd^{3+} ($^4G_{9/2} \rightarrow {}^4F_{3/2}$), Yb^{3+} ($^2F_{7/2} \rightarrow {}^2F_{5/2}$), populating the $^2F_{5/2}$ level of Yb^{3+}. In the second step the remaining energy can be transferred to a second Yb^{3+}-ion from the $^4F_{3/2}$ level of Nd^{3+}. Both Yb^{3+}-ions can then emit a photon of approximately 1000 nm.

efficiency [7,9].

Contrary to UC, DC is a linear process. This makes it possible to obtain high conversion efficiencies independent of the incident power and allows for the use of non-concentrated sunlight. Demonstrations of efficient DC materials are still limited (contrary to UC materials). Initially DC work focused on the conversion of a single VUV photon into two visible photons. The Gd^{3+}–Eu^{3+} couple in a $LiGdF_4$ host lattice shows efficient VUV to VIS DC (internal quantum efficiency of approximately 190%) and Er^{3+}, Gd^{3+} and Tb^{3+} in the same host lattice have an efficiency of 130% [4,10,11].

Downconversion of UV or visible photons into NIR photons was first demonstrated in (Y, Yb)PO_4:Tb^{3+} [12]. After excitation into the $^5D_4$ state of the Tb^{3+}-ion two neighboring Yb^{3+}-ions are excited through a cooperative energy transfer process. The $^5D_4$ level of Tb^{3+} is found at about twice the energy of the Yb^{3+} $^2F_{5/2}$ level, and after energy transfer Yb^{3+} emission is observed around 1000 nm. This is just above the band gap of crystalline silicon which makes Yb^{3+} an attractive candidate for DC materials to be used in combination with c-Si solar cells. More recently, cooperative downconversion has also been reported for Tb^{3+}–Yb^{3+} in other host materials [13,14]

and other lanthanide couples, viz. Pr^{3+}–Yb^{3+} [15] and Tm^{3+}–Yb^{3+} [16]. It is not clear, however, that the second-order cooperative energy transfer process is the operative mechanism in the Pr^{3+}–Yb^{3+} system, as also first-order energy transfer processes are possible and are expected to dominate [17]. Second-order cooperative energy transfer processes have a lower efficiency, making them only efficient at very high Yb^{3+} concentrations where the Yb^{3+} emission is largely quenched through concentration quenching. For more efficient energy transfer, an intermediate level on the donor ion should be used in order to obtain downconversion through two resonant energy transfer steps.

In this chapter we investigate if efficient downconversion is possible with the Nd^{3+}–Yb^{3+} couple in YF_3 and $CsCdBr_3$. We have chosen YF_3 and $CsCdBr_3$ as a host because these lattices have a low phonon energy (maximum phonon energy YF_3 ~500 cm^{-1} [18], $CsCdBr_3$ 180 cm^{-1}); a lower phonon energy minimizes multi-phonon relaxation processes between the closely spaced energy levels of Nd^{3+}, which can reduce the radiative downconversion efficiency. In Fig. 6.1 the downconversion scheme for the Nd^{3+}–Yb^{3+} couple via sequential two-step energy transfer is shown. When Nd^{3+} is excited into the $^4G_{9/2}$ state, part of the energy is transferred to Yb^{3+} via cross relaxation: Nd^{3+} ($^4G_{9/2} \rightarrow {}^4F_{3/2}$), Yb^{3+} ($^2F_{7/2} \rightarrow {}^2F_{5/2}$), populating the $^2F_{5/2}$ level of Yb^{3+}. In a second step the remaining energy can be transferred to a second Yb^{3+}-ion which can then emit a photon, or otherwise IR emission can occur from the $^4F_{3/2}$ level of Nd^{3+}.

An advantage of the $CsCdBr_3$ host lattice is that three doubly charged Cd will be replaced by two triply charged lanthanide ions, while in the YF_3 host lattice the lanthanides replace the chemically similar Y^{3+} ions (and will therefore be randomly distributed through the lattice). As a result pair formation is favored for lanthanide ions in $CsCdBr_3$, which facilitates efficient energy transfer between the ions.

6.2 Methods

6.2.1 Synthesis

YF_3

Crystalline powder samples of YF_3 doped with Nd^{3+} and Yb^{3+} were synthesized via co-precipitation. The Nd^{3+} concentration was kept constant at 0.5% while the Yb^{3+} concentration was varied (0, 2, 3, 5 or 10%). Also two samples without Nd^{3+} were synthesized containing 2 and 10% Yb^{3+}. In all cases the percentages given for the

dopants Yb^{3+} or Nd^{3+} are mol% with respect to Y^{3+}. The samples were prepared by mixing stoichiometric amounts of Y_2O_3, Nd_2O_3 and Yb_2O_3 (purity at least 4N). The powder mixture was dissolved in dilute hydrochloric or nitric acid. After adding a solution with an excess of NH_4F (98+%) a precipitate was formed, which was centrifuge-washed and then dried. The precipitate was placed in an alumina crucible and fired in an oven together with an excess of NH_4F under a nitrogen flow. The samples were first heated to 300°C for two hours (to remove adsorbed water molecules) and then to 1000°C for three hours. After the samples had cooled sufficiently they were crushed with a pestle and mortar and x-ray diffraction measurements were performed to check for phase purity.

$CsCdBr_3$

Multi-crystalline samples of $CsCdBr_3$ doped with Nd^{3+} and Yb^{3+} were synthesized via a dry-mixture method. The samples were prepared by mixing stoichiometric amounts of dried CsBr, $CdBr_2$, $YbCl_3$ and $NdCl_3$. The powder mixture was put into a quartz ampoule, which was then evacuated and sealed. The ampoule was put into a high frequency furnace and heated to 650°C in 4 hours and kept at that temperature for 4 hours. The sample was cooled down slowly to 400°C in 10 hours to anneal the sample. The samples that were used for the luminescence measurements were left in the ampoules since $CsCdBr_3$ is slightly hygroscopic. One additional sample was synthesized so that it could be removed from the ampoule and x-ray diffraction measurements could be performed to check for phase purity.

6.2.2 Measurements

Diffuse reflectance spectra were measured with a Perkin-Elmer Lambda 950 UV/VIS/IR absorption spectrometer. Emission and excitation spectra were measured with a SPEX DM3000F spectrofluorometer with a 450 W Xe lamp as the excitation source. Excitation and emission wavelengths were selected with a double-grating 0.220 m SPEX 1680 monochromator (1200 l/mm) blazed at 300 nm. Emission spectra were recorded by focusing the emitted light on a fiber guiding the light to a 0.3 m monochromator (Scientific Spectra Pro, Princeton Instruments) where the emission light is dispersed by a 150 l/mm grating or a 1200 l/mm grating, both blazed at 500 nm. The dispersed light was detected with a Princeton Instruments 300i charge coupled device (CCD). Emission and excitation measurements, particularly for the infra-red region, were performed using an Edinburgh Instruments FLS920 fluorescence spectrometer. The 0.3 m excitation double monochromator disperses light from a 450 W

Xe lamp with gratings blazed at 300, 500 or 1200 nm. UV and visible sample emission is detected with an emission monochromator with a grating blazed at 300 or 500 nm and a Hamamatsu R928 photomultiplier tube (PMT). The NIR emission is detected with another emission monochromator with a grating blazed at 1200 nm and a liquid nitrogen-cooled Hamamatsu R5509-72 PMT. The Edinburgh fluorescence spectrometer is equipped with an Oxford helium flow cryostat for low temperature measurements. The spectra were not corrected for the instrumental response, unless otherwise indicated. In those cases a radiometrically calibrated DH-2000 halogen lamp from Ocean Optics was used to correct emission spectra for variation in the instrumental response to allow for an absolute comparison of photon fluxes in different spectral regions.

Lifetime measurements upon pulsed excitation at a wavelength of 452 nm were performed with the use of a Lambda Physik LPD3000 tunable dye laser with a Coumarin 120 dye solution (tunable between 423-462 nm). Lifetime measurements with an excitation wavelength of 480 nm were performed on the same setup with a Coumarin 102 dye solution (tunable between 460-510 nm) and for an excitation wavelength of 950 nm a Styryl 14 dye solution (tunable between 904-992 nm) was used. The dye laser is pumped by a Lambda Physik LPX100 excimer (XeCl) laser. The typical pulse width for the setup is ~20 ns and the repetition rate is 10 Hz. The laser excitation is steered into the sample chamber of the Edinburgh fluorescence spectrometer using a pair of prisms.

6.3 Results and discussion YF_3

6.3.1 Characterization

For all samples of YF_3 (doped with 0.5% Nd^{3+} and 0, 2, 3, 5 and 10% Yb^{3+} and two samples doped with 2 and 10% Yb^{3+}) the X-ray diffraction patterns are consistent with the orthorhombic structure of YF_3.

To monitor the incorporation of Nd^{3+} and Yb^{3+} in YF_3, diffuse reflection spectra were recorded. In the diffuse reflectance spectra (Fig. 6.2), it can be seen that the absorption strengths for the peaks corresponding to Nd^{3+} absorptions (e.g. the $^4I_{9/2} \rightarrow {}^4F_{7/2}$ transition around 750 nm and the $^4I_{9/2} \rightarrow {}^4G_{9/2}$ transition around 500 nm) are very similar for all samples. This shows that Nd^{3+} was built into the lattice equally well for all samples, since in the starting mixture the same amount of Nd^{3+} (0.5%) was present. Furthermore, the peak for the Yb^{3+} absorption strength around 1000 nm

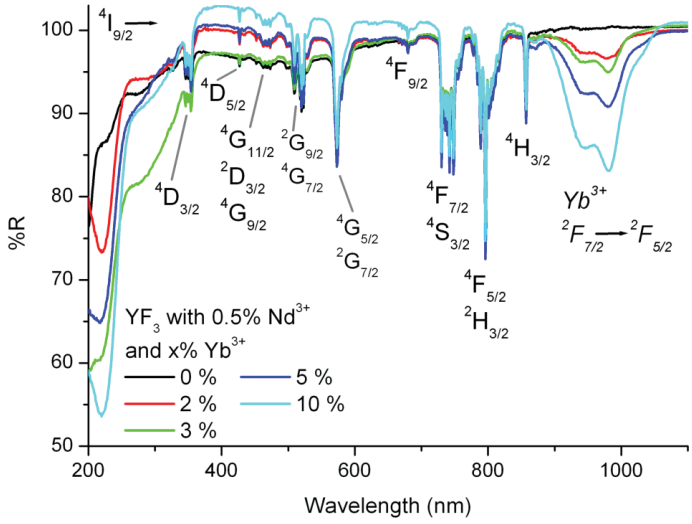

Figure 6.2: Diffuse reflectance spectra for YF_3:Nd^{3+}(0.5%), Yb^{3+}(0, 2, 3, 5 and 10%).

varies in good agreement with the Yb^{3+} concentration that was present in the starting mixture.

In the UV (between 250 and 300 nm), a strong absorption band can be observed which is probably related to defects, possibly involving oxygen impurities. The intensity for this band varies between samples, and it is strongest for the sample co-doped with 0.5% Nd^{3+} and 3% Yb^{3+}.

6.3.2 Luminescence

The energy level diagram in Fig. 6.1 shows the desired downconversion scheme: starting from the Nd^{3+} $^4G_{9/2}$ level around 21 000 cm^{-1} cross-relaxation with a neighboring Yb^{3+}-ion involves partial energy transfer, which results in Nd^{3+} in the $^4F_{3/2}$ state and Yb^{3+} in the $^2F_{5/2}$ state. In the next step (phonon-assisted) energy transfer from the $^4F_{3/2}$ level of Nd^{3+} to a second Yb^{3+}-ion results in a second excited Yb^{3+}-ion, and both ions can emit a 980 nm photon. To investigate if downconversion according to this scheme occurs, emission spectra were first recorded for YF_3:Nd^{3+} without Yb^{3+}.

For downconversion it is crucial that the starting level for downconversion ($^4G_{9/2}$) is sufficiently long-lived to allow for energy transfer to a neighboring Yb^{3+}-ion. If the

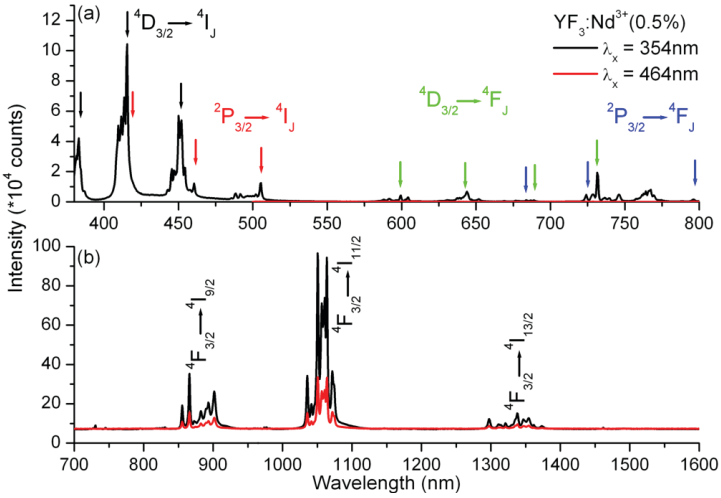

Figure 6.3: Room temperature emission spectra for the visible (a) and infrared (b) part of the spectrum for $YF_3:Nd^{3+}(0.5\%)$. The excitation wavelength is 354 nm ($^4D_{1/2}$ level).

level has a sufficiently long lifetime, emission from the level can be observed and one can expect the occurrence of downconversion. However, the energy level diagram in Fig. 6.1 shows that a competing process, multi-phonon relaxation from $^4G_{9/2}$ to the next lower level ($^2G_{9/2}$) is also possible which may prevent downconversion. If multi-phonon relaxation to the next lower level dominates, the lifetime of the level is shortened, no emission will be observed and it is unlikely that downconversion can compete with fast multi-phonon relaxation. Downconversion from higher energy levels was also investigated. The energy level diagram in Fig. 6.1 reveals relatively large energy gaps below the $^2P_{3/2}$ and the $^4D_{3/2}$ level which indicates that these states may be sufficiently long lived to give rise to downconversion.

Fig. 6.3 shows the room temperature emission spectra of YF_3 doped with 0.5% Nd^{3+} for excitation in the Nd^{3+} $^4D_{1/2}$ level (354 nm) and the $^4G_{9/2}$ level (464 nm). The results show that upon excitation at 354 nm, emission is observed from both the $^4D_{3/2}$ and the $^2P_{3/2}$ level to the ^4I_J levels. This indicates that these levels may serve as starting levels for downconversion. Upon excitation at 464 nm, only infrared emission is observed around 870 nm, 1050 nm and 1340 nm, all of which originate from $^4F_{3/2} \rightarrow {}^4I_J$ transitions. The absence of $^4G_{9/2} \rightarrow {}^4I_J$ emissions shows that the energy gap between the $^4G_{9/2}$ level and the next lower level ($^2G_{9/2}$) is bridged by fast multi-phonon relaxation and that radiative decay from the $^4G_{9/2}$ level cannot com-

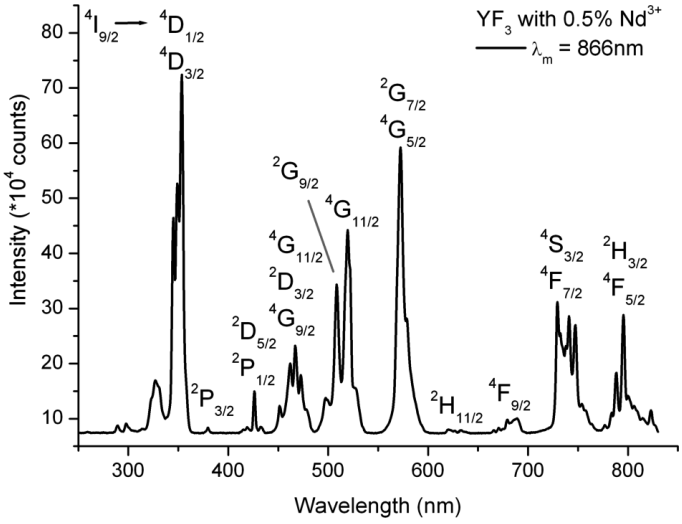

Figure 6.4: Room temperature excitation spectrum of $^4F_{3/2} \rightarrow {}^4I_{9/2}$ emission (866 nm) for YF_3:Nd^{3+}(0.5%).

pete with this non-radiative relaxation process. As a result downconversion from the $^4G_{9/2}$ level is probably not possible. The $^4F_{3/2} \rightarrow {}^4I_J$ emission peaks are also observed for excitation into the higher energy levels, such as the $^4D_{1/2}$, $^4D_{3/2}$ and the $^2P_{3/2}$ levels. This indicates that from the higher energy emitting levels non-radiative relaxation to the $^4F_{3/2}$ level also occurs. This is confirmed by the excitation spectrum of the $^4F_{3/2} \rightarrow {}^4I_{9/2}$ emission around 866 nm (Fig. 6.4) where peaks can be observed corresponding to transitions to all levels above the $^4F_{3/2}$ level of Nd^{3+}.

The Nd^{3+} emission is quenched when the samples are co-doped with Yb^{3+}. At a concentration of 3% Yb^{3+}, the Nd^{3+} emission both in the visible and in the infrared has almost completely disappeared (Fig. 6.5). When the Yb^{3+} concentration is increased to 10% the remaining Nd^{3+} emission intensity is less than 1% of the intensity for the sample without Yb^{3+}. At the same time, the Yb^{3+} emission around 1000 nm starts to increase, and it reaches its maximum for the sample doped with 0.5% Nd^{3+} and 5% Yb^{3+}. Increasing the concentration further does not lead to a higher Yb^{3+} emission intensity. Instead, the emission intensity starts to decrease for the sample with 0.5% Nd^{3+} and 10% Yb^{3+}, which is explained by concentration quenching.

For the highest Yb^{3+} concentration there is also a change in the relative intensities of the Yb^{3+} emission at 986 and at 1028 nm. The peak at 986 nm is higher than

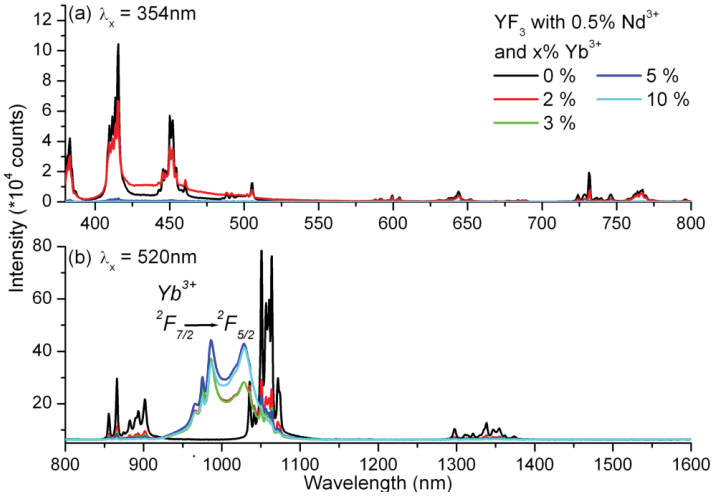

Figure 6.5: Room temperature emission spectra for YF_3:Nd^{3+}(0.5%), Yb^{3+}(0, 2, 3, 5 and 10%). (a) Visible part of the spectrum, excitation wavelength is 354 nm ($^4D_{1/2}$ level). (b) Infrared part of the spectrum, excitation wavelength is 520 nm ($^4G_{11/2}$ level).

the peak at 1028 nm for Yb^{3+} concentrations up to 5%, while the 1028 nm peak is higher for the YF_3:Nd^{3+}(0.5%), Yb^{3+}(10%) sample. For this high concentration, re-absorption of the shorter wavelength emission around 986 nm can occur, thus lowering the relative intensity of this emission component. Furthermore, energy transfer over multiple Yb^{3+}-ions can occur to Yb^{3+}-ions that emit at lower energy values, leading to emission at longer wavelengths.

The emission spectra recorded after excitation in the lower energy levels of Nd^{3+} (below the $^4G_{9/2}$ level), shown for $^4G_{11/2}$ (520 nm) in Fig. 6.5(b), demonstrate that the energy transfer from Nd^{3+} to Yb^{3+} after multi-phonon relaxation is efficient and does lead to emission from Yb^{3+} as desired. This indicates that one-step energy transfer occurs from Nd^{3+} to Yb^{3+}. After non-radiative relaxation to the $^4F_{3/2}$ level, efficient transfer can be expected as the $^4F_{3/2} \rightarrow {}^4I_{11/2}$ transition on Nd^{3+} is resonant with the $^2F_{5/2} \rightarrow {}^2F_{7/2}$ transition on Yb^{3+}.

To determine if downconversion occurs from the higher energy levels via the two-step energy transfer process (yielding two NIR photons) excitation spectra were recorded for emission from the $^4F_{3/2}$ level of Nd^{3+} in YF_3:Nd^{3+}(0.5%) and emission from the $^2F_{5/2}$ level of Yb^{3+} in YF_3:Nd^{3+}(0.5%), Yb^{3+}(2%). If downconversion occurs from a high energy level, the relative intensity of the peak corresponding to the

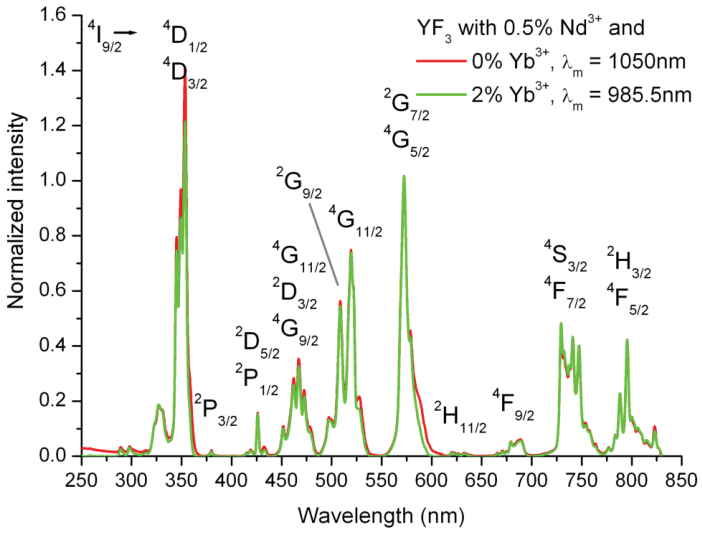

Figure 6.6: Room temperature excitation spectrum of Nd^{3+} emission (1050 nm) in YF_3:Nd^{3+}(0.5%) and Yb^{3+} emission (986 nm) in YF_3:Nd^{3+}(0.5%), Yb^{3+}(2%), both normalized at 572 nm (excitation into Nd^{3+} $^2G_{7/2}$/$^4G_{5/2}$).

transition to this level should increase in the excitation spectrum of the Yb^{3+} emission, as two instead of one NIR photons are generated [17]. The spectra are compared by normalizing to the excitation lines of Nd^{3+} corresponding to the transition to the $^2G_{7/2}$/$^4G_{5/2}$ level around 570 nm (Fig. 6.6). Excitation below the $^2G_{7/2}$/$^4G_{5/2}$ level will be followed by rapid multi-phonon relaxation to the $^4F_{3/2}$ level as is evident from the small energy gaps separating the levels below this level (see Fig. 6.1). In both excitation spectra the peaks for these levels will appear with approximately the same relative intensities. Fig. 6.6 shows that there is no increase in the relative intensity of the peak for excitation into the $^4G_{9/2}$ level (470 nm) for the Yb^{3+} co-doped sample compared to the sample only doped with Nd^{3+}. This indicates that downconversion does not occur from the $^4G_{9/2}$ level. There is, however, an increase in the relative intensity of the peak for excitation into the $^4D_{3/2}$ level at 354 nm. When comparing the excitation peak intensities of the 866 nm Nd^{3+} and the 986 nm Yb^{3+} emission, an increase is observed in all samples co-doped with Yb^{3+} (Fig. 6.7). The ratio of the intensities of the $^4D_{3/2}$ excitation peak relative to the $^2G_{7/2}$/$^4G_{5/2}$ excitation peaks increases from 1.1 to 1.4 when the Yb^{3+} concentration is increased from 2 to 10%. This indicates that downconversion occurs from the Nd^{3+} $^4D_{3/2}$ level, and that the efficiency increases with increasing Yb^{3+}-concentration, as expected. Based on the observed intensity ra-

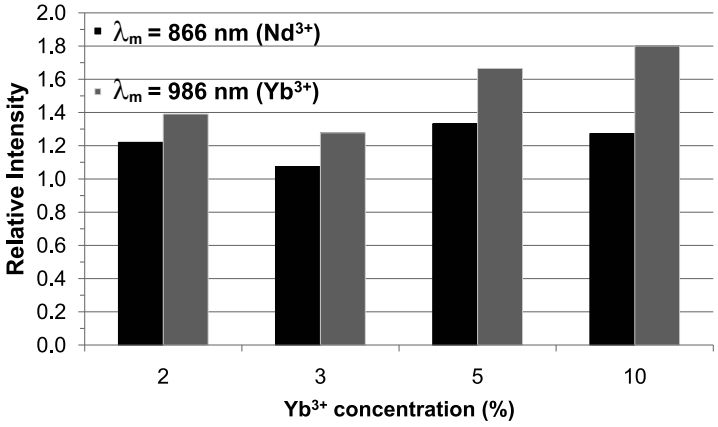

Figure 6.7: Comparison of relative excitation peak intensities of Nd^{3+} and Yb^{3+} emission for YF_3:Nd^{3+}(0.5%), Yb^{3+}(2, 3, 5 and 10%). The excitation spectra were measured at room temperature and normalized at 572 nm (excitation into the Nd^{3+} $^2G_{7/2}$/$^4G_{5/2}$ levels).

tios, it can be concluded that the downconversion efficiency increases up to 140% in the sample with 10% Yb^{3+}.

The absence of downconversion from the $^4G_{9/2}$ level is attributed to multi-phonon relaxation. To further investigate the multi-phonon relaxation process, a high resolution excitation spectrum of the $^4F_{3/2}$ emission in YF_3:Nd^{3+} (0.5%) was recorded to determine the energy gap between the $^4G_{9/2}$ and $^2G_{9/2}$ level (Fig. 6.8). The excitation spectrum shows sharp transitions to the various crystal field (CF) components of the $^4G_{9/2}$ level between 460 and 475 nm and to the $^2G_{9/2}$ components between 495 and 525 nm. The energy gap between the lowest CF of the $^4G_{9/2}$ and the highest CF component of the $^2G_{9/2}$ level is determined to be 1012 cm^{-1}. Since the maximum phonon energy of YF_3 is ~500 cm^{-1}, the energy gap between the $^4G_{9/2}$ and $^2G_{9/2}$ level can be bridged by two to three phonons. Based on the energy gap law and experimental results, a rule of thumb predicts that radiative decay and multi-phonon relaxation can compete when the gap is five times the phonon energy. For a smaller energy-gap, multi-phonon relaxation dominates. Therefore the absence of emission from the Nd^{3+} $^4G_{9/2}$ level is in agreement with present findings: the energy difference between the $^4G_{9/2}$ level and the next lower level ($^2G_{9/2}$) is small enough for non-radiative decay to dominate in this host, making DC from the $^4G_{9/2}$ level inefficient. In hosts with a smaller phonon energy, e.g. chlorides ($\hbar\omega$ ~250 cm^{-1}) or bromides ($\hbar\omega$ ~180 cm^{-1}), DC from the $^4G_{9/2}$ level may compete with non-radiative relaxation, and efficient downconversion could be achieved.

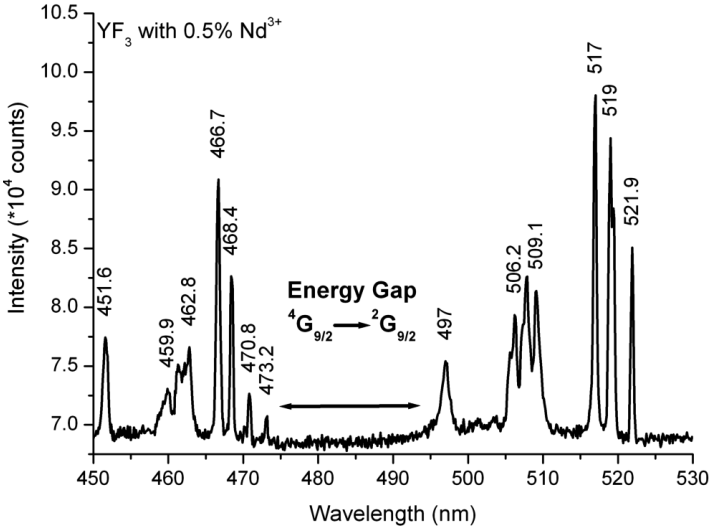

Figure 6.8: High resolution excitation spectrum of 1050 nm emission in YF_3:Nd^{3+}(0.5%) measured at 4 K.

6.3.3 Decay measurements

To gain further insight in the energy transfer processes between Nd^{3+} and Yb^{3+}, luminescence decay curves were recorded for the Nd^{3+} and Yb^{3+} emission upon excitation into the $^4G_{9/2}$ level at 456 nm (Figs. 6.9 and 6.10). The luminescence decay curves of the Nd^{3+} $^4F_{3/2}$ emission (866 nm) in YF_3:Nd^{3+}(0.5%) can be described by a single exponential with a lifetime of 390 μs. When the sample is co-doped with Yb^{3+}, the lifetime decreases and the decay is no longer single exponential (Fig. 6.9). This shows that energy transfer from Nd^{3+} to Yb^{3+} occurs and the transfer rate increases as the Yb^{3+} concentration is raised. The non-exponential character of the decay curves reflects the different distributions of Yb^{3+}-ions around different Nd^{3+}-ions, which gives rise to a wide distribution of transfer rates between Nd^{3+} and Yb^{3+}-ions. The rapid decrease of the decay time upon raising the Yb^{3+} concentration from 2 to 10% shows that energy transfer from Nd^{3+} to Yb^{3+} is efficient, consistent with the rapid drop of the Nd^{3+} emission intensity upon adding Yb^{3+} observed in Fig. 6.5. To analyze the energy transfer more quantitatively, the luminescence decay curves were modeled using Monte Carlo simulations. In a previous paper the basics of the modeling procedure have been outlined and the model was used to distinguish between different possible energy transfer mechanisms (cooperative, accretive or phonon-assisted

single-step) [12]. The present energy transfer process clearly involves a single-step transfer from Nd^{3+} to neighboring Yb^{3+}-ions and only this mechanism is therefore considered. For the single-step energy transfer through dipole-dipole interaction, the transfer rate to all neighbors is given by:

$$\gamma_{tr} = C_{tr} \sum_i \frac{1}{r_i^6} \tag{6.1}$$

where γ_{tr} is the transfer rate for a Nd^{3+}-ion in the excited $^4F_{3/2}$ state to transfer to all neighboring Yb^{3+}-ions at distances r. The constant C_{tr} is a fitting parameter and the summation is over all Yb^{3+} neighbors i. A discrete atom model was used based on the unit cell of YF_3 (orthorhombic with a = 6.353 Å, b = 6.850 Å and c = 4.393 Å) and the coordinates of the Y-atoms in the unit cell [19, 20]. The size of the box considered for energy transfer was 5^3 unit cells which means that all interactions up to 15 Å were taken into account. For larger distances no improvement of the simulations was observed indicating that energy transfer over longer distances does not contribute significantly. The lattice sites were filled randomly with Y^{3+} or Yb^{3+} with a probability specified by the Y^{3+} to Yb^{3+} ratio. Substitution of one of the lanthanides by Nd^{3+} generated a particular configuration. For each configuration the single exponential decay curve is given by:

$$I_t = e^{t(\gamma_{tr}+\gamma_r)} \tag{6.2}$$

where t is time, γ_r is the radiative decay rate of the $^4F_{3/2}$ state of Nd^{3+} in YF_3 and γ_{tr} is the energy transfer rate as calculated with Eq. 6.1. The decay curves recorded result from an ensemble average of configurations. Therefore an ensemble average signal was calculated:

$$< I_t >=< e^{t(\gamma_{tr}+\gamma_r)} > \tag{6.3}$$

where <> denotes ensemble averaging over 10 000 configurations. With this number convergence was reached. The simulations are shown in Fig. 6.9 for the different Yb^{3+} concentrations for $\gamma_r = 2.55 \cdot 10^3$ s^{-1} (τ_r = 390 µs) and $C_{tr} = 7.07 \cdot 10^8$ $Å^6 \cdot s^{-1}$. The agreement is excellent showing that the energy transfer between Nd^{3+} and Yb^{3+} is well described by energy transfer through dipole-dipole interactions. The energy transfer is indeed very efficient. The transfer rate to nearest neighbors at 3.6 Å is $3.25 \cdot 10^5$ s^{-1}, more than 100 times faster than the radiative decay rate of $2.55 \cdot 10^3$ s^{-1}.

In the decay curves of the Yb^{3+} emission, a build-up is observed in the first part of the curve (Fig. 6.10), causing the Yb^{3+} emission to reach a maximum approximately

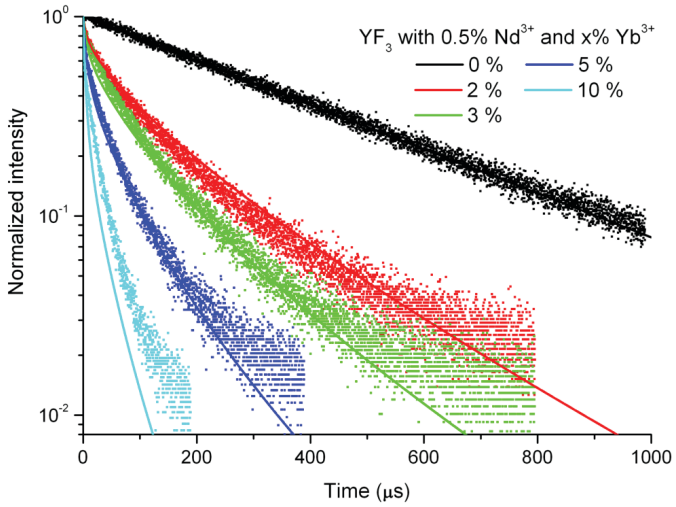

Figure 6.9: Room temperature lifetime measurements (dotted lines) of Nd^{3+} $^4F_{3/2}$ emission (866 nm) in YF_3:Nd^{3+}(0.5%) co-doped with Yb^{3+} (0, 2, 3, 5 and 10%) after excitation into the Nd^{3+} $^4G_{9/2}$ level at 456 nm. The solid lines are simulated curves using a Monte Carlo model for single-step energy transfer through dipole-dipole interaction (Eqs. 6.1-6.3).

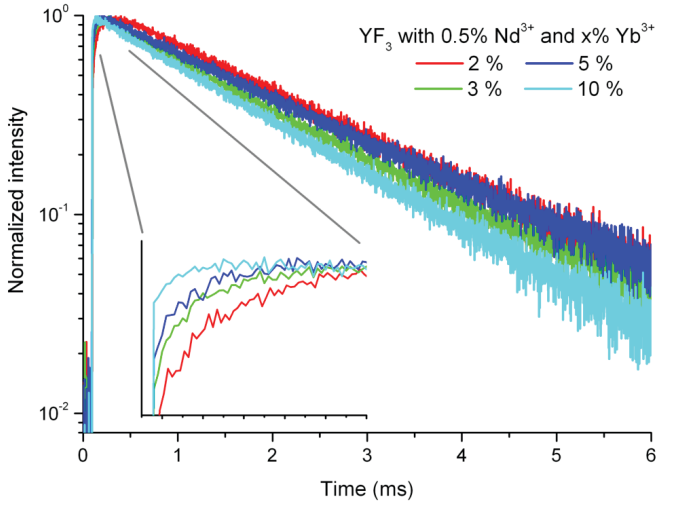

Figure 6.10: Room temperature lifetime measurements of Yb^{3+} $^2F_{5/2}$ emission (986 nm) in YF_3:Nd^{3+}(0.5%), Yb^{3+}(2, 3, 5 and 10%) after excitation into the Nd^{3+} $^4G_{9/2}$ level at 456 nm. The inset shows the build-up in the first 0.2 ms of the curve.

150 μs after the start of the measurement. This build-up time is similar to the decay times of the $^4F_{3/2}$ emission from Nd^{3+}, which confirms that the Yb^{3+} emission is fed by energy transfer from the Nd^{3+} $^4F_{3/2}$ level. The build-up time decreases from 80 μs for YF_3:Nd^{3+}(0.5%), Yb^{3+}(2%) to 13 μs for YF_3:Nd^{3+}(0.5%), Yb^{3+}(10%), confirming that the energy transfer becomes more efficient at higher Yb^{3+} concentrations. The effect of concentration quenching can be seen in the long time part of the decay curve: at low Yb^{3+} concentrations the lifetime is approximately 1900 μs, and as the Yb^{3+} concentration increases to 10%, the lifetime decreases to ~1560 μs. The decrease in lifetime is ascribed to energy migration of the excitation energy over the Yb^{3+}-sublattice, which can result in quenching of the luminescence if the migrating excitation energy encounters a quenching site.

6.3.4 Temperature dependent measurements

To gain further understanding about the energy transfer processes and the concentration quenching in YF_3:Nd^{3+}, Yb^{3+}, temperature dependent measurements were performed. Fig. 6.11 shows typical temperature-dependent spectra for YF_3:Nd^{3+}(0.5%), Yb^{3+}(2%). At 4 K the emission peaks of both Nd^{3+} and Yb^{3+} are very narrow compared to the spectra at room temperature. Thermally induced relaxation processes cause the emission peaks to broaden at higher temperatures (lifetime broadening). Furthermore, additional peaks for emission from higher crystal field components start to appear when the temperature is raised. An example of this effect is the peak for emission from a higher crystal field component of the Yb^{3+} $^2F_{5/2}$ level at 965 nm that appears when the temperature is increased to 50 K.

As seen from the room temperature emission spectra (Fig. 6.5), and the lifetime measurements of the Yb^{3+} emission (Fig. 6.10), Yb^{3+} $^2F_{5/2}$ emission starts to decrease due to concentration quenching for high Yb^{3+} concentrations. At very low temperatures (4 K), concentration quenching is hampered which causes a strong increase in the Yb^{3+} emission intensity. This is explained by the small energy mismatches between the energy levels of neighboring Yb^{3+}-ions, which impose the need for phonon-assisted energy transfer; by freezing out the phonons at low temperatures, the energy migration becomes less efficient and the concentration quenching is reduced.

At low temperatures, an additional peak is visible in the Yb^{3+} emission spectra at 980.5 nm (see the inset of Fig. 6.11), which disappears when the temperature is raised above 50 K. Low-temperature lifetime measurements for the emission peaks between 980 and 1024 nm are compared (Fig. 6.12). The lifetime of the tail of the decay curves is approximately 1500 μs for all curves, and all four decay curves show a build-up in the beginning of the curve. The build-up time is ~50 μs for emission wavelengths

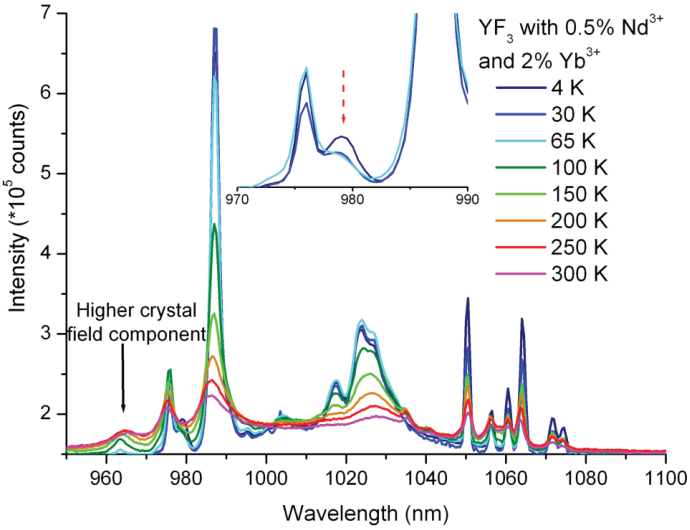

Figure 6.11: Temperature dependent emission spectra for YF_3:Nd^{3+}(0.5%), Yb^{3+}(2%). The inset shows the effect of temperature on the peak at 980 nm.

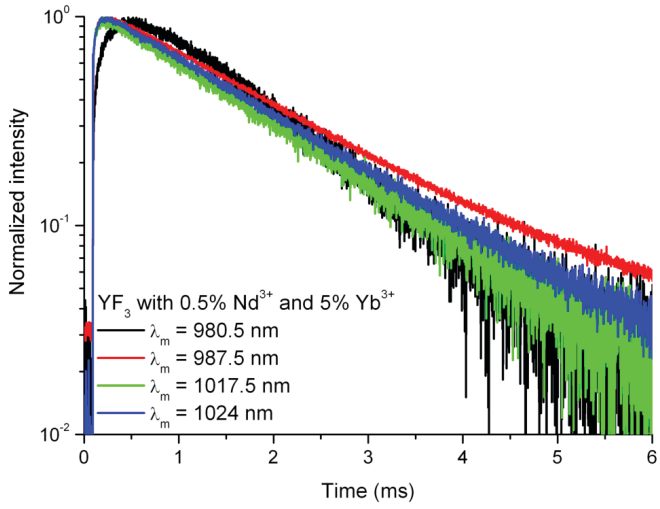

Figure 6.12: Lifetime measurements at 4 K of Yb^{3+} $^2F_{5/2}$ emission at different wavelengths in YF_3:Nd^{3+}(0.5%), Yb^{3+}(5%) after excitation into the Nd^{3+} $^4G_{9/2}$ level at 456 nm.

between 987 and 1024 nm, and is attributed to energy transfer from Nd^{3+} to Yb^{3+} (see also Fig. 6.9). The build-up time for the 980.5 nm emission is approximately 225 μs. The longer build-up time and the observation that this emission peak disappears above 50 K can be explained by the presence of a small amount of oxygen in the sample. For Yb^{3+}-ions situated next to an oxygen impurity, a very common contamination in fluorides, the lowest $^2F_{5/2}$ level is lowered in energy (~47 cm^{-1} based on the position of the emission lines at 976 nm for Yb^{3+} on the dominant site, and 980.5 nm for Yb^{3+} next to an oxygen impurity, which will be indicated by $Yb - O_F^{'}$). At higher temperatures thermal de-trapping occurs, and this explains the observed decrease in the 980.5 nm emission intensity above 50 K. To confirm the presence of $Yb - O_F^{'}$, the excitation spectrum for the 980.5 nm emission was compared to an excitation spectrum of Yb^{3+} emission at 987 nm (Fig. 6.13(a)). In the excitation spectrum for the Yb^{3+} emission (black line) peaks for excitation into the different Nd^{3+} levels are present (compare Fig. 6.6), while for the 980.5 nm emission (red dotted line) a broad band between 250 and 350 nm can be observed. Such a band is typical for oxygen ligand-to-metal charge-transfer (CT) for lanthanides, in this case from O^{2-} to Yb^{3+} [21]. This is further confirmed by the emission spectra for excitation into the CT band which results in an intense Yb^{3+} emission at 980.5 nm, while for excitation into the Nd^{3+} $^4G_{9/2}$ level the intrinsic Yb^{3+} emission lines dominate (Fig. 6.13(b)). The shift of the emission peak indicates that oxygen lowers the position of the Yb^{3+} $^2F_{5/2}$ energy level, which can then act as an energy trap ($Yb - O_F^{'}$) at lower temperatures, resulting in an emission peak at 980 nm below 50 K (Fig. 6.11). The slower build-up in the decay curve of the 980 nm emission is then explained by energy transfer to $Yb - O_F^{'}$ (Fig. 6.12).

The presence of oxygen can also be observed in the absorption spectra as an absorption band around 250 nm (Fig. 6.2). Oxygen and fluoride have a similar ionic radius, making oxide contamination of fluorides a commonly observed problem.

6.4 Results and discussion $CsCdBr_3$

YF_3 has a maximum phonon energy of ~500 cm^{-1} [18]. In the previous section it was concluded that DC was not possible in this host lattice due to fast multi-phonon relaxation from the $^4G_{9/2}$ level, and that a host with a smaller phonon energy was necessary for efficient DC to occur. From the high resolution spectrum in Fig. 6.8 the energy difference between the Nd^{3+} $^4G_{9/2}$ level and the next lower level ($^2G_{9/2}$) was determined to be around 1012 cm^{-1}. $CsCdBr_3$ has a maximum phonon energy of 180 cm^{-1} which means that for the $CsCdBr_3$ host lattice about 6 phonons are needed to

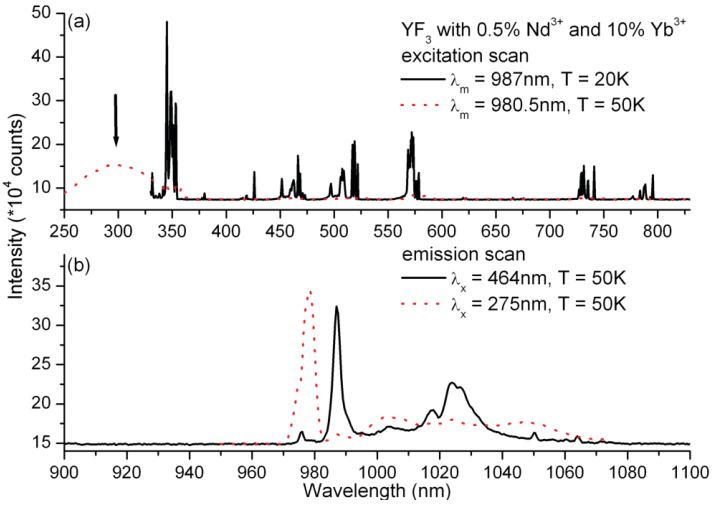

Figure 6.13: Excitation (a) and emission (b) spectra for YF_3:Nd^{3+}(0.5%), Yb^{3+}(10%) showing the O^{2-}-Yb^{3+} CT band and emission from Yb^{3+} affected by the presence of oxygen ($Yb - O'_F$).

bridge the energy gap between the $^4G_{9/2}$ and the $^2G_{9/2}$ level. This makes non-radiative relaxation unlikely and therefore DC with the Nd^{3+}–Yb^{3+} couple should be possible in this host lattice. In this section preliminary results on DC for the Nd^{3+}–Yb^{3+} couple in $CsCdBr_3$ are presented.

Samples of $CsCdBr_3$ doped with 1% Nd^{3+} and 0, 2 and 5 mol% Yb^{3+} were synthesized. X-ray diffraction measurements gave similar results for all three samples and were consistent with the hexagonal structure of $CsCdBr_3$ [22, 23]. Fig. 6.14 shows excitation spectra for $CsCdBr_3$:Nd^{3+}(1%), Yb^{3+}(0, 2, 5%) while observing emission from the Yb^{3+} $^2F_{5/2}$ level around 1011 nm. This emission overlaps with Nd^{3+} $^4F_{3/2} \rightarrow {}^4I_{11/2}$ emission. Peaks can be observed for excitation into the Nd^{3+} ^4G_J levels (~480, 535 and 600 nm), $^2G_{7/2}$ (~600 nm) and ^4F_J levels (~750, 820 and 890 nm). For the sample doped with only Nd^{3+} the peaks are small, indicating that the emission around 1011 nm is not very strong. When Yb^{3+} is present in the samples a band appears for excitation into the the $CsCdBr_3$ host lattice and the intensity of the Nd^{3+} peaks increases. This spectrum shows that energy transfer from Nd^{3+} to Yb^{3+} takes place since Yb^{3+} emission can be observed (in addition to the Nd^{3+} $^4F_{3/2} \rightarrow {}^4I_{11/2}$ emission) after excitation in Nd^{3+} levels.

In Fig. 6.15 the emission spectra for the three samples are shown. The spectra

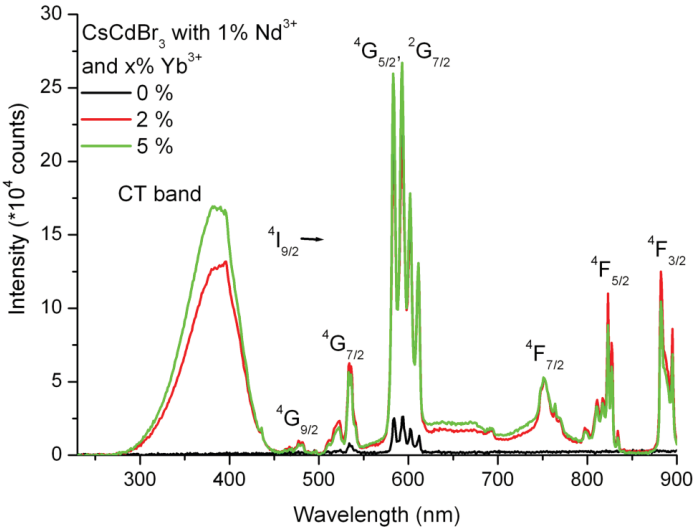

Figure 6.14: Room temperature excitation spectra of $CsCdBr_3$:Nd^{3+}(1%), Yb^{3+}(0, 2, 5%). The emission wavelength is 1011 nm (Yb^{3+} $^2F_{5/2} \rightarrow {}^2F_{7/2}$ transition or the Nd^{3+} $^4F_{3/2} \rightarrow {}^4I_{11/2}$ transition).

are corrected for instrumental response so that the areas of the integrated emission peaks represent the total photon flux and can be compared quantitatively. The spectra show that intense Yb^{3+} emission is observed around 1000 nm, consistent with efficient downconversion from the $^4G_{9/2}$ level.

Decay curves (Fig. 6.16) of Nd^{3+} $^4F_{3/2}$ emission (892 nm) after excitation into the Nd^{3+} $^4G_{11/2}$ level (480 nm) further demonstrate that energy transfer from Nd^{3+} to Yb^{3+} takes place. The decay curves for all three samples show a build-up in the first part of the curve due to relaxation from the Nd^{3+} $^4G_{11/2}$ level to the $^4F_{3/2}$ level. As more Yb^{3+} is added to the samples the build-up becomes faster due to cross-relaxation between Nd^{3+} and Yb^{3+} (the first step in the DC process, see also Fig. 6.1). When Yb^{3+} is present in the samples the $^4F_{3/2}$ level is not only fed by non-radiative relaxation from the $^4G_{11/2}$ to the $^4F_{3/2}$ level of Nd^{3+}, but this can also occur via cross-relaxation (Nd^{3+} $^4G_{9/2} \rightarrow {}^4F_{3/2}$, Yb^{3+} $^2F_{7/2} \rightarrow {}^2F_{5/2}$). For the sample doped with only Nd^{3+} the tail of the decay curve shows a single exponential decay, while for the samples co-doped with Yb^{3+} the decay is faster and non-exponential. The non-exponential character of the decay curves reflects the different distributions of Yb^{3+}-ions around different Nd^{3+}-ions, giving rise to a large variation in the energy transfer

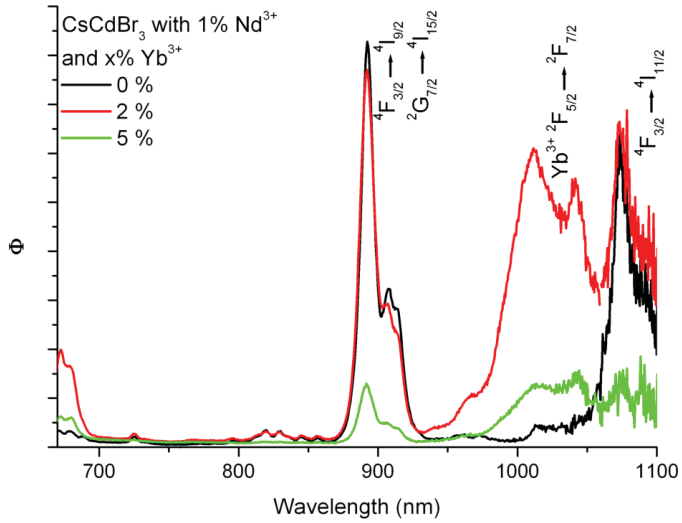

Figure 6.15: Room temperature emission spectra of $CsCdBr_3$:Nd^{3+}(1%), Yb^{3+}(0, 2, 5%), λ_{ex} = 480 nm ($^4G_{9/2}$ level). The spectra are recorded under identical conditions and corrected for instrumental response. Φ gives the photon flux per constant wavelength interval.

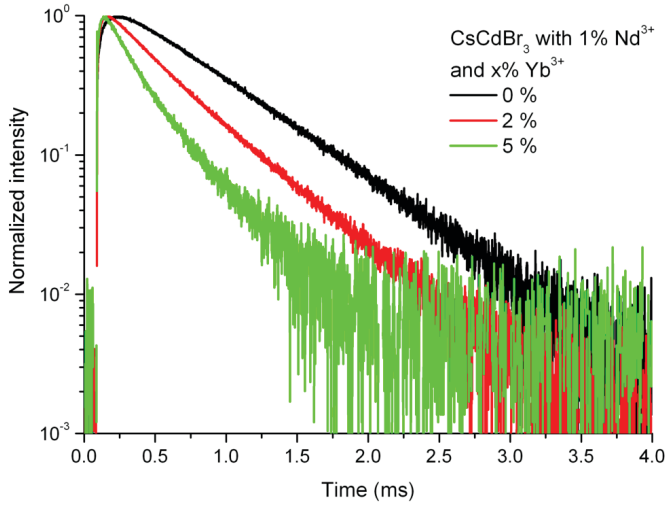

Figure 6.16: Luminescence decay curves for the Nd^{3+} $^4F_{3/2}$ emission in $CsCdBr_3$:Nd^{3+}(1%), co-doped with 0, 2, or 10% Yb^{3+} measured at room temperature. The excitation wavelength is 480 nm (into the $^4G_{11/2}$ level) and the emission wavelength is 892 nm (Nd^{3+} $^4F_{3/2} \rightarrow {}^4I_{9/2}$).

rates between Nd^{3+} and Yb^{3+}-ions.

Further measurements are required to understand the mechanism for energy transfer in the Nd^{3+}–Yb^{3+} downconversion couple in $CsCdBr_3$. Optimization of the synthesis conditions and the Nd^{3+} and Yb^{3+} concentrations may lead to an efficient downconversion material that can be used in combination with c-Si solar cells.

6.5 Conclusions

Downconversion for the Nd^{3+}–Yb^{3+} couple has been investigated in YF_3:Nd^{3+}, Yb^{3+}. Emission and excitation measurements of YF_3:Nd^{3+}(0.5%) show that excitation into energy levels of Nd^{3+} between 28 500 and 17 500 cm^{-1}(350-570 nm), results in non-radiative decay to the $^4F_{3/2}$ level, followed by emission from this level to the ^4I_J levels in the infrared. In co-doped samples downconversion from the Nd^{3+} $^4G_{9/2}$ level via the cross relaxation process Nd^{3+} ($^4G_{9/2} \rightarrow {}^4F_{3/2}$), Yb^{3+} ($^2F_{7/2} \rightarrow {}^2F_{5/2}$), followed by a second energy transfer step from the $^4F_{3/2}$ level of Nd^{3+} to Yb^{3+}, could possibly lead to the emission of two IR photons from Yb^{3+}. However, fast multi-phonon relaxation is found to occur from the $^4G_{9/2}$ level to the lower $^2G_{9/2}$ level and this prevents efficient downconversion from the $^4G_{9/2}$ level, as cross-relaxation is much less efficient than multi-phonon relaxation.

The multi-phonon relaxation from the $^4G_{9/2}$ level and lower energy levels results in population of the $^4F_{3/2}$ level of Nd^{3+}. From here efficient one-step energy transfer to Yb^{3+} occurs through dipole-dipole interaction. The energy difference between the Nd^{3+} $^4G_{9/2}$ and the next lower $^2G_{9/2}$ level is determined to be 1012 cm^{-1} and this small energy difference explains that multi-phonon relaxation dominates in YF_3, where the maximum phonon energy is around 500 cm^{-1}. From the higher energy $^4D_{3/2}$ level of Nd^{3+} downconversion is observed with efficiencies up to 140%. The high energy position of this level (in the UV part of the spectrum) does not make this a promising downconversion route for solar cell applications.

In a low phonon frequency host, $CsCdBr_3$, the Nd^{3+}–Yb^{3+} couple does show efficient downconversion. Multi-phonon relaxation is suppressed and excitation in the $^4G_{9/2}$ level is followed by two-step energy transfer to Yb^{3+} neighbors and a strong emission band around 1000 nm is observed. Based on these initial results, bromides can be considered as promising host lattices for efficient downconversion.

References

[1] W. Shockley and H. Queisser, *Detailed balance limit of efficiency of p-n junction solar cells*, J. Appl. Phys. **32**, 510 (1961).

[2] M. Green, K. Emery, Y. Hishikawa, and W. Warta, *Solar cell efficiency tables (version 33)*, Prog. Photovolt: Res. Appl. **17**, 85 (2009).

[3] F. Auzel, *Upconversion and anti-Stokes processes with f and d ions in solids*, Chem. Rev. **104**, 139 (2004).

[4] R. Wegh, H. Donker, K. Oskam, and A. Meijerink, *Visible quantum cutting in $LiGdF_4:Eu^{3+}$ through downconversion*, Science **283**, 663 (1999).

[5] T. Trupke, M. Green, and P. Würfel, *Improving solar cell efficiency by down-conversion of high-energy photons*, J. Appl. Phys. **92**, 1668 (2002).

[6] T. Trupke, M. Green, and P. Würfel, *Improving solar cell efficiencies by up-conversion of sub-band-gap light*, J. Appl. Phys. **92**, 4117 (2002).

[7] T. Trupke, A. Shalav, B. Richards, P. Würfel, and M. Green, *Efficiency enhancement of solar cells by luminescent up-conversion of sunlight*, Sol. En. Mat. Sol. Cell. **90**, 3327 (2006).

[8] J. Suyver, A. Aebischer, D. Biner, P. Gerner, J. Grimm, S. Heer, K. Krämer, C. Reinhard, and H. Güdel, *Novel materials doped with trivalent lanthanides and transition metal ions showing near-infrared to visible photon conversion*, Opt. Mat. **27**, 1111 (2005).

[9] A. Shalav, B. Richards, T. Trupke, K. Krämer, and H. Güdel, *Application of $NaYF_4:Er^{3+}$ up-converting phophors for enhanced near-infrared silicon solar cell response*, Appl. Phys. Lett. **86**, 013505 (2005).

[10] K. Oskam, R. Wegh, H. Donker, E. van Loef, and A. Meijerink, *Downconversion: a new route to visible quantum cutting*, J. Alloy Comp. **300-301**, 421 (2000).

[11] R. Wegh, E. van Loef, and A. Meijerink, *Visible quantum cutting via downconversion in $LiGdF_4:Er^{3+},Tb^{3+}$ upon Er^{3+} $4f^{11} \rightarrow 4f^{10}5d$ excitation*, J. Lumin. **90**, 111 (2000).

[12] P. Vergeer, T. Vlugt, M. Kox, M. den Hertog, J. van der Eerden, and A. Meijerink, *Quantum cutting by cooperative energy transfer in $Yb_xY_{1-x}PO_4:Tb^{3+}$*, Phys. Rev. B. **71**, 014119 (2005).

[13] Q. Zhang, G. Yang, and Z. Jiang, *Cooperative downconversion in $GdAl_3(BO_3)_4$: RE^{3+},Yb^{3+} (RE=Pr, Tb, and Tm)*, Appl. Phys. Lett. **91**, 051903 (2007).

[14] J. Yuan, X. Zeng, J. Zhao, Z. Zhang, H. Chen, and X. Yang, *Energy transfer mechanisms in Tb^{3+},Yb^{3+} codoped Y_2O_3 downconversion phosphor*, J. Phys. D: Appl. Phys. **41**, 105406 (2008).

[15] G. Lakshminarayana, H. Yang, S. Ye, Y. Liu, and J. Qiu, *Cooperative downconversion luminescence in $Pr^{3+}/Yb^{3+}:SiO_2$-Al_2O_3-BaF_2-GdF_3 glasses*, J. Mater. Res. **23**, 3090 (2008).

[16] G. Lakshminarayana, H. Yang, S. Ye, Y. Liu, and J. Qiu, *Co-operative downconversion luminescence in $Tm^{3+}/Yb^{3+}:SiO_2$-Al_2O_3-LiF-GdF_3 glasses*, J. Phys. D: Appl. Phys. **41**, 175111 (2008).

[17] B. van der Ende, L. Aarts, and A. Meijerink, *Near-infrared quantum cutting for photovoltaics*, Adv. Mat. **21**, 3073 (2009).

[18] H. Rast, H. Caspers, and S. Miller, *Lattice vibrations and infrared properties of yttriumfluoride*, Phys. Rev. **180**, 890 (1969).

[19] R. W. G. Wyckoff, *Crystal structures*, Interscience, New York, 2nd edition edition, 1963.

[20] A. Zalkin and D. Templeton, *The crystal structures of YF_3 and related compounds*, J. Am. Chem. Soc. **75**, 2453 (1953).

[21] L. van Pieterson, M. Heeroma, E. de Heer, and A. Meijerink, *Charge transfer luminescence of Yb^{3+}*, J. Lumin. **91**, 177 (2000).

[22] P. Ren, J. Qin, and C. Chen, *A novel nonlinear optical crystal for the IR region: noncentrosymmetrically crystalline CsCdBr and its properties*, Inorg. Chem. **42**, 8 (2003).

[23] G. McPherson and K. Devany, *Spectroscopic properties of vanadium(II), manganese(II), and nickel(II) in crystals of cesium tribromocadmate*, Inorg. Chem. **16**, 1565 (1977).

7

Downconversion with the Ho^{3+}–Yb^{3+} couple in $LiYF_4$

Abstract

The efficiency of solar cells can be increased by combining a solar cell with a downconverting layer. In a downconversion material *two* low energy NIR photons are emitted for each high energy photon that is absorbed. Luminescence spectra (excitation and emission) and luminescence decays curves have been recorded for $LiYF_4$:Ho^{3+}, Yb^{3+} to investigate the potential for downconversion of this couple. Yb^{3+} emission is observed after excitation into the Ho^{3+} $^5F_1$ level but downconversion from the $^5F_3$ level around 490 nm does not take place due to fast non-radiative relaxation over an energy gap of ~1500 cm^{-1} to the $^5F_4/^5S_2$ levels. In a host lattice with low vibrational energies efficient downconversion may be achieved.

7.1 Introduction

A large part of the energy losses that limit the conversion efficiency of solar cells to 30% is related to the spectral mismatch [1]. Photons with an energy smaller than the band-gap (E_g) will not be absorbed (sub band-gap transmission) and a large part of the energy of photons with an energy larger than the band-gap is lost as heat (thermalization losses). The energy losses related to the spectral mismatch can be reduced by adapting the solar cell to the solar spectrum, for instance by combining multiple semiconductor materials with different bandgaps, each converting a different part of the solar spectrum with high efficiency. This approach has been successfully applied and energy efficiencies over 40% have been reported [2]. An alternative way to reduce the spectral mismatch losses is through adapting the solar spectrum so that the solar cell can use it more efficiently.

A promising option is downconversion (DC): one higher energy photon is split to obtain two photons with a smaller energy. Each of these photons can subsequently be absorbed by the solar cell and generate an electron-hole pair. Because one photon is 'cut' into two smaller energy photons this process is also known as quantum cutting. Lanthanide ions are very well suited to use for DC because they have a rich energy level structure that allows for efficient spectral conversion [3, 4].

It is evident from the Dieke diagram (Fig. 1.3) that the energy level structure of Yb^{3+} is ideally suited for use in downconversion for c-Si solar cells. The Yb^{3+}-ion has a single excited state ($^2F_{5/2}$) approximately 10 000 cm^{-1} above the $^2F_{7/2}$ ground state, corresponding to an emission around 1000 nm. The absence of other energy levels allows Yb^{3+} to exclusively 'pick up' energy packages of 10 000 cm^{-1} from other co-doped lanthanide ions and emit photons at ~1000 nm, which can be absorbed by c-

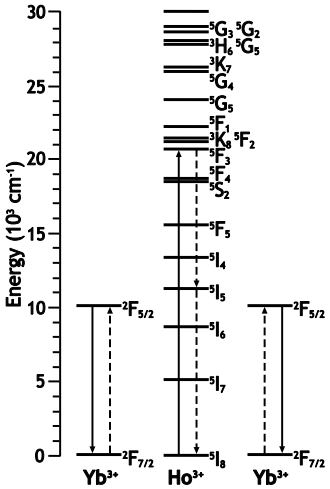

Figure 7.1: Energy level scheme of the Ho^{3+} ($4f^{10}$) and Yb^{3+} ($4f^{13}$) couple showing a mechanism for downconversion via two-step energy transfer. First energy is transferred from Ho^{3+} to one Yb^{3+} neighbor (Ho^{3+} ($^5F_3 \rightarrow {}^5I_5$), Yb^{3+} ($^2F_{7/2} \rightarrow {}^2F_{5/2}$)) followed by emission of an infrared photon by Yb^{3+} ($^2F_{5/2} \rightarrow {}^2F_{7/2}$). The remaining energy can be transferred to a second Yb^{3+} neighbor (Ho^{3+} ($^5I_5 \rightarrow {}^5I_8$), Yb^{3+} ($^2F_{7/2} \rightarrow {}^2F_{5/2}$)), or emitted by Ho^{3+}.

Si. Efficient downconversion using Yb^{3+} via resonant energy transfer requires donor ions with an energy level at about 20 000 cm^{-1} and an intermediate energy level at approximately 10 000 cm^{-1}. In the previous chapters, a variety of downconversion couples (Pr^{3+}–Yb^{3+}, Er^{3+}–Yb^{3+} and Nd^{3+}–Yb^{3+}) have been studied in detail. In this chapter results are reported for Ho^{3+}–Yb^{3+}. Examination of Fig. 1.3 reveals that with the Ho^{3+}–Yb^{3+} couple it may be possible to achieve donwconversion via a two-step energy transfer mechanism (see Fig. 7.1). After excitation of the Ho^{3+}-ion into the $^5F_3$ level energy can be transferred from Ho^{3+} to one Yb^{3+} neighbor (Ho^{3+} ($^5F_3 \rightarrow {}^5I_5$), Yb^{3+} ($^2F_{7/2} \rightarrow {}^2F_{5/2}$)), and the remaining energy can be transferred to a second Yb^{3+} neighbor (Ho^{3+} ($^5I_5 \rightarrow {}^5I_8$), Yb^{3+} ($^2F_{7/2} \rightarrow {}^2F_{5/2}$)). This is then followed by emission of an infrared photon by both Yb^{3+}-ions ($^2F_{5/2} \rightarrow {}^2F_{7/2}$ transition). A fluoride host lattice was chosen because fluorides typically have a small phonon energy (500-600 cm^{-1}), so that the amount of non-radiative decay will be limited.

Preliminary experiments on DC with the Ho^{3+}–Yb^{3+} couple in $LiYF_4$ show an energy transfer efficiency of 94% at the highest Yb^{3+} concentration (30%), but the visible to NIR conversion efficiency is low. Further experiments are necessary to elucidate the downconversion mechanism and to optimize the conversion efficiency.

7.2 Methods

7.2.1 Synthesis

Crystalline powder samples of $LiYF_4$ doped with Ho^{3+} and Yb^{3+} were synthesized via co-precipitation. The samples were prepared by mixing stoichiometric amounts of Y_2O_3, Ho_2O_3 and Yb_2O_3 (purity at least 4N). The powder mixture was dissolved in diluted acid. After adding a solution with an excess of NH_4F (98+%) a precipitate was formed, which was centrifuge-washed and then dried. The dried precipitate was mixed with LiF (5% excess) and NH_4F, placed in an alumina crucible and fired in an oven under a nitrogen flow. The samples were first heated to 300°C for three hours (to remove adsorbed water molecules) and then to 600°C for three hours. After the samples had cooled sufficiently they were crushed with a pestle and mortar and x-ray diffraction measurements were performed to check for phase purity.

7.2.2 Measurements

Diffuse reflectance spectra were measured with a Perkin-Elmer Lambda 950 UV/VIS/IR absorption spectrometer. Emission and excitation spectra were measured with a SPEX DM3000F spectrofluorometer with a 450 W Xe lamp as the excitation source. Excitation and emission wavelengths were selected with a double-grating 0.220 m SPEX 1680 monochromator (1200 l/mm) blazed at 300 nm. Emission spectra were recorded by focusing the emitted light on a fiber guiding the light to a 0.3 m monochromator (Scientific Spectra Pro, Princeton Instruments) where the emission light is dispersed by a 150 l/mm grating or a 1200 l/mm grating, both blazed at 500 nm. The dispersed light was detected with a Princeton Instruments 300i charge coupled device (CCD).The spectra were not corrected for the instrumental response. Emission and excitation measurements were also performed using an Edinburgh Instruments FLS920 fluorescence spectrometer. The 0.3 m excitation double monochromator disperses light from a 450 W Xe lamp which can be tuned with 1200 l/mm gratings blazed at 300, 500 and 1200 nm. UV and visible sample emission is detected with an emission double monochromator employing a 1200 l/mm grating blazed at 500 nm and a Hamamatsu R928 PMT. The NIR emission is detected with another emission double monochromator with a 1200 l/mm grating blazed at 1200 nm and a liquid nitrogen-cooled Hamamatsu R5509-72 PMT. Lifetime measurements were all performed with the use of a Lambda Physik LPD3000 tunable dye laser filled with Coumarin 102 dye solution (tunable between 460-510 nm). The dye-laser is pumped by a Lambda Physik LPX100 excimer (XeCl) laser. The typical pulse width for the

setup is ~20 ns and the repetition rate is 10 Hz. The laser excitation is steered into the sample chamber of the Edinburgh fluorescence spectrometer using a pair of prisms.

7.3 Results and discussion

For the different samples of $LiYF_4$ doped with 1 mol% Ho^{3+} and 0, 5, 10 and 30 mol% Yb^{3+} x-ray diffraction measurements confirmed the formation of single phase crystalline powders with the $LiYF_4$ scheelite crystal structure. In Fig. 7.2 the emission spectra are shown for the four different samples upon excitation at 480 nm in the $^5F_1$ level. From this level fast non-radiative relaxation to the $^5F_3$ level is expected in view of the small energy separations between the levels (see Fig. 7.1). From the $^5F_3$ level the downconversion process depicted in Fig. 7.1 can occur. A competing process is further non-radiative relaxation to the $^5F_4/^5S_2$ levels. The energy gap between the $^5F_3$ level and the $^5F_4$ level, as determined from high resolution low temperature excitation spectra (Fig. 7.3), is ~1500 cm^{-1}. The situation is very similar to the case of the Er^{3+}–Yb^{3+} couple discussed in Chapters 4 and 5 where downconversion from the $^4F_{7/2}$ level had to compete with multi-phonon relaxation to the $^2H_{11/2}/^4S_{3/2}$ level, also some 1500 cm^{-1} lower in energy. In the emission spectrum for the sample doped with 1% Ho^{3+}, it is clear that no emission is observed from the $^5F_3$ level. Only emission from the $^5F_4/^5S_2$ and from the $^5F_5$ level is present. This shows that the $^5F_3 \rightarrow {}^5F_4/^5S_2$ multi-phonon relaxation rate is fast in this fluoride host and radiative decay or downconversion cannot compete. Just as for the Er^{3+}–Yb^{3+} and Nd^{3+}–Yb^{3+} couples, efficient downconversion can only be anticipated for the Ho^{3+}–Yb^{3+} couple in host lattices with low phonon energies (bromides and possibly chlorides).

In the samples co-doped with Ho^{3+} and Yb^{3+} the intensity of the Ho^{3+} emission lines decreases with increasing Yb^{3+} concentration while Yb^{3+} emission is observed around 1000 nm. Clearly, efficient energy transfer occurs from both the $^4F_4/^5S_2$ and $^4F_5$ levels of Ho^{3+} to Yb^{3+}. The energy level diagrams in Fig. 7.1 show that efficient energy transfer can be expected through cross-relaxation (Ho^{3+} ($^5S_2/^4F_4 \rightarrow {}^5I_6$), Yb^{3+} ($^2F_{7/2} \rightarrow {}^2F_{5/2}$) and Ho^{3+} ($^4F_5 \rightarrow {}^5I_7$), Yb^{3+} ($^2F_{7/2} \rightarrow {}^2F_{5/2}$)). Contrary to the situation for Er^{3+} where energy transfer from the $^4S_{3/2}$ level to Yb^{3+} was very inefficient, the Ho^{3+}-ion does efficiently transfer its energy to neighboring Yb^{3+}-ions. The observation that the intensity drop for the $^4F_5$ emission upon co-doping with Yb^{3+} is more pronounced than for the $^4F_4/^5S_2$ emission shows that cross-relaxation from the $^4F_5$ level is more efficient. The energy transfer results in Yb^{3+} emission around 1000 nm. The emission is strongest for the sample co-doped with 30% Yb^{3+}. The efficient cross-relaxation does not result in emission of two NIR photons. The final

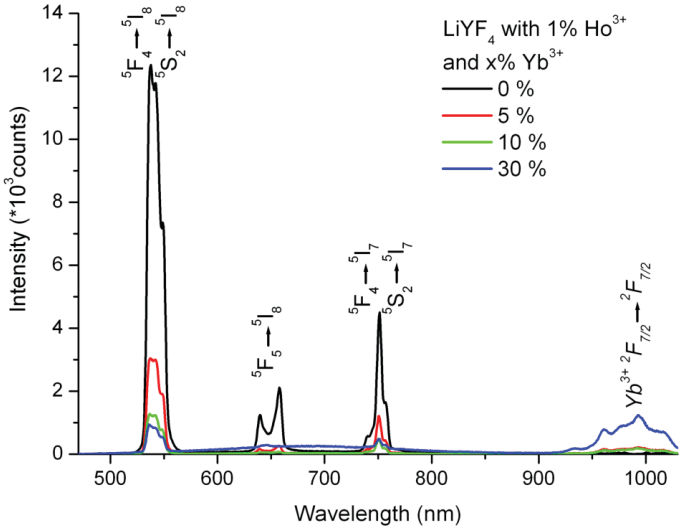

Figure 7.2: Room temperature emission spectra of $LiYF_4$:Ho^{3+}(1%), Yb^{3+}(0, 5, 10, 30%). The excitation wavelength is 480 nm (into the Ho^{3+} $^5F_1$ level).

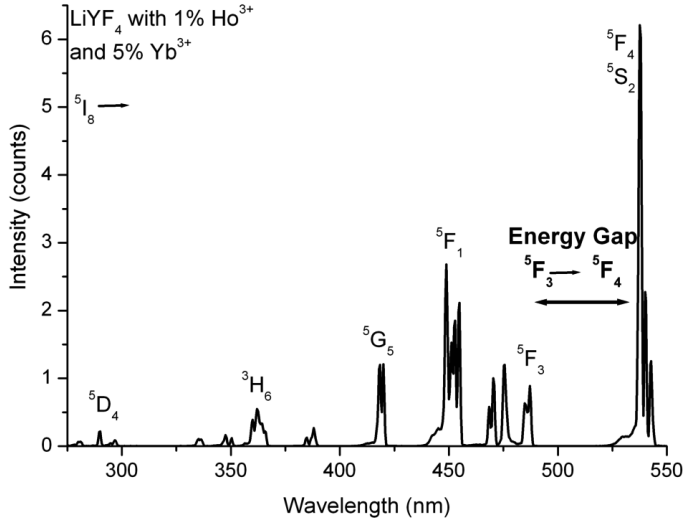

Figure 7.3: High resolution excitation spectrum of $LiYF_4$:Ho^{3+}(1%), Yb^{3+}(5%) for an emission wavelength of 750 nm ($^5I_4 \rightarrow {}^5I_8$ transition) measured at 4 K.

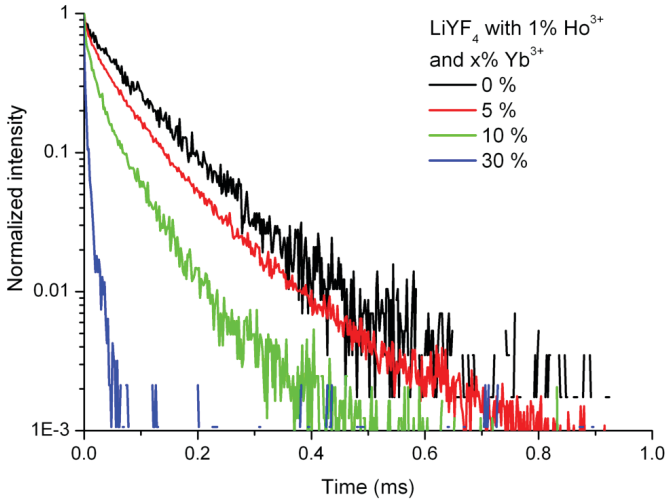

Figure 7.4: Room temperature luminescence decay curves of $LiYF_4$:Ho^{3+}(1%), Yb^{3+}(0, 5, 10, 30%). The excitation wavelength is 490 nm (Ho^{3+} $^5F_3$ level) and the emission wavelength is 540 nm (Ho^{3+} $^5S_2/^5F_4 \rightarrow {}^5I_8$ transition).

levels for the cross-relaxation on Ho^{3+} are the $^5I_6$ and $^5I_7$ levels. From both levels efficient IR emission can be expected but at wavelengths too far in the IR to be absorbed by crystalline-Si (approximately 1200 nm for the $^5I_6$ level and around 2000 nm for the $^5I_7$ level)

Luminescence decay curves recorded for the $^4F_4/^5S_2$ emission are shown in Fig. 7.4. These results confirm the presence of efficient energy transfer from Ho^{3+} to Yb^{3+}: upon raising the Yb^{3+} concentration, the decay curves for the $^4F_4/^5S_2$ emission become faster and non-exponential. The non-exponential character reflects the variety of distributions of Yb^{3+}-ions around the Ho^{3+}-ions, giving rise to different energy transfer rates from Ho^{3+} donors to the Yb^{3+} acceptors. The efficiency of energy transfer can be estimated from the integrated areas under the normalized decay curves [5]. Integration reveals that the transfer efficiency from the $^4F_4/^5S_2$ level is 28, 64 and 94% in the samples co-doped with 5, 10 and 30% Yb^{3+}, respectively.

7.4 Conclusions

Luminescence spectra (excitation and emission) and luminescence decay curves have been recorded for $LiYF_4$:Ho^{3+},Yb^{3+} to investigate the potential of this couple for downconversion. The results show that the desired downconversion process (Ho^{3+} ($^5F_3 \rightarrow {}^5I_5$), Yb^{3+} ($^2F_{7/2} \rightarrow {}^2F_{5/2}$) followed by Ho^{3+} ($^5I_5 \rightarrow {}^5I_8$), Yb^{3+} ($^2F_{7/2} \rightarrow {}^2F_{5/2}$)) does not occur. Fast multi-phonon relaxation from the $^5F_3$ level to the $^4F_4/^5S_2$ levels over an energy gap of about 1500 cm^{-1} is too fast and prevents downconversion. From the $^4F_4/^5S_2$ levels efficient energy transfer to Yb^{3+} is observed. To achieve efficient downconversion the Ho^{3+}–Yb^{3+} couple should be incorporated in a host lattice with low phonon energies.

References

[1] W. Shockley and H. Queisser, *Detailed balance limit of efficiency of p-n junction solar cells*, J. Appl. Phys. **32**, 510 (1961).

[2] M. Green, K. Emery, Y. Hishikawa, and W. Warta, *Solar cell efficiency tables (version 33)*, Prog. Photovolt: Res. Appl. **17**, 85 (2009).

[3] F. Auzel, *Upconversion and anti-Stokes processes with f and d ions in solids*, Chem. Rev. **104**, 139 (2004).

[4] R. Wegh, H. Donker, K. Oskam, and A. Meijerink, *Visible quantum cutting in $LiGdF_4$:Eu^{3+} through downconversion*, Science **283**, 663 (1999).

[5] P. Vergeer, T. Vlugt, M. Kox, M. den Hertog, J. van der Eerden, and A. Meijerink, *Quantum cutting by cooperative energy transfer in $Yb_xY_{1-x}PO_4$:Tb^{3+}*, Phys. Rev. B. **71**, 014119 (2005).

Samenvatting

Deze samenvatting is bedoeld om het onderzoek dat in dit proefschrift beschreven wordt begrijpelijker te maken voor iedereen die geïnteresseerd is, maar niet zo goed thuis is in het onderwerp. Om uit te kunnen leggen wat het doel van het onderzoek is en de resultaten (kort) toe te lichten, wordt eerst een aantal begrippen geïntroduceerd.

Om klein te beginnen: alle stoffen om ons heen zijn opgebouwd uit (verschillende combinaties van) atomen. In de kern van elk atoom bevinden zich positief geladen **protonen**. Daar omheen draaien de negatief geladen **elektronen** in een vaste baan. Elk type atoom heeft een ander aantal protonen en elektronen. Zo heeft bijvoorbeeld het waterstofatoom 1 proton in de kern en daar omheen draait 1 elektron, terwijl een koolstofatoom 6 protonen en 6 elektronen heeft. In het Periodiek Systeem zijn de verschillende atomen die bekend zijn geordend in een tabel zodat helemaal bovenaan de atomen met het kleinste aantal protonen en elektronen staan, en helemaal onderin de atomen die zijn opgebouwd uit de meeste protonen en elektronen. Het kan ook voorkomen dat een atoom één of meer elektronen mist, zodat het een positieve lading heeft, of juist elektronen te veel heeft en een negatieve lading heeft. Atomen met een lading noemen we **ionen**.

Elk elektron heeft een vaste baan om de kern van het atoom, en zal niet zomaar van baan veranderen. Als een atoom energie opneemt kan een elektron naar een baan gaan, die verder van de kern af ligt. Dit noemen we dan een **aangeslagen toestand**. Aangezien er (afhankelijk van het soort atoom) veel verschillende mogelijke banen voor een elektron om de kern zijn, zijn er ok veel verschillende aangeslagen toestanden. Een elektron dat in een hogere baan terecht is gekomen, kan ook weer terugkeren naar zijn oorspronkelijke baan (de **grondtoestand** van het atoom), en daarbij energie verliezen. Er zijn verschillende manieren waarop een atoom energie kan verliezen. Wanneer een atoom energie afstaat in de vorm van licht noemen we dit **luminescentie**.

Laten we iets beter kijken naar de relatie tussen licht, kleur en energie. Licht kan gezien worden als bestaande uit 'pakketjes' energie die we **fotonen** noemen. Hoeveel energie fotonen bij zich dragen, wordt bepaald door de golflengte. De golflengte is

ook bepalend voor de kleur van het licht. Een rood foton met een golflengte van 650 nm (nanometer: één miljardste van een meter of 10^{-9} m) heeft minder energie dan een geel foton met een golflengte van 570 nm, wat weer minder energie heeft dan een blauw foton met een golflengte van 475 nm. De zon geeft een breed **spectrum** van fotonen met verschillende kleuren, wat goed te zien is in een regenboog. Alle kleuren in het zichtbare deel van het zonnespectrum zie je hierin op volgorde van lage naar hoge energie: rood, oranje, geel, groen, blauw, violet. Sommige fotonen kunnen niet worden waargenomen door het menselijk oog, zoals fotonen met een kleinere energie dan rode fotonen (deze noemen we infrarood, golflengte langer dan ongeveer 750 nm) en fotonen met een grotere energie dan de violette fotonen (deze noemen we ultraviolet, golflengte korter dan ongeveer 400 nm).

De energie in licht kunnen we goed gebruiken. Zeker in een tijd waarin de vraag naar energie groeit, maar de voorraden van fossiele brandstoffen opraken en de zorgen over de effecten op het milieu groeien. De zon is een overvloedige bron van (schone) energie: vanaf de zon bereikt meer energie de aarde in één uur (43 EJ, 11.9 biljoen kWh) dan het huidige verbruik van de hele planeet in een jaar (41 EJ, 11.4 biljoen kWh). Om te kunnen voldoen aan de vraag naar energie, maar tegelijkertijd CO_2-emissies te verminderen, moeten we (meer) gebruik gaan maken van alternatieve, schonere energiebronnen. Met behulp van **zonnecellen** kan de energie in het zonlicht direct worden omgezet in elektriciteit. Daarom zijn zonnecellen een goede optie om ons van duurzame energie te voorzien. Helaas is de prijs per kWh van zonne-energie relatief hoog, zodat het belangrijk is om zonnecellen efficiënter en/of goedkoper te maken.

Meestal worden zonnecellen gemaakt van materialen die we halfgeleiders noemen. In halfgeleiders is iets bijzonders aan de hand: in plaats van dat er 'losse' aangeslagen toestanden zijn voor elk atoom in de halfgeleider, vormen de aangeslagen toestanden in de halfgeleider samen een energie**band**. In de grondtoestand is de onderste band, die de **valentieband** genoemd word, helemaal gevuld met elektronen. De volgende energieband, de **geleidingsband**, is leeg. Het energieverschil tussen de bovenkant van de valentieband en de onderkant van de geleidingsband noemen we de energiekloof of **bandgap**. Omdat de valentieband helemaal vol is kan er geen stroom lopen (elektriciteit is immers niets anders dan elektronen die in beweging zijn). Wanneer er licht (fotonen) op een halfgeleider valt, met voldoende energie om een elektron van de valentie- naar de geleidingsband te brengen, kan er een stroom gaan lopen: een zonnecel levert dan energie in de vorm van elektriciteit.

De zonnecellen die op dit moment het meest gebruikt worden kunnen slechts 15% van de energie die door de zon als licht wordt geleverd omzetten in elektrische energie. Ongeveer 60% van het energieverlies heeft te maken met wat de **spectral**

mismatch wordt genoemd. Het spectrum van de zon bestaat uit fotonen met verschillende energie. Wanneer een foton met een energie die kleiner is dan de bandgap van de halfgeleider op de zonnecel valt, kan deze energie helemaal niet gebruikt worden (**transmissieverlies**). Er is immers niet genoeg energie om een elektron naar de geleidingsband te brengen. Er zijn ook fotonen met een energie die (veel) groter is dan de bandgap. De 'extra' energie in deze fotonen die overblijft nadat een elektron van de valentieband naar de geleidingsband is gebracht, kan niet gebruikt worden om elektriciteit op te wekken en raakt verloren als warmte (**thermalisatieverlies**).

Om deze verliezen zo klein mogelijk te maken zijn er twee mogelijkheden. De eerste optie is het aanpassen van de zonnecel aan het zonnespectrum. Dit wordt toegepast bij zogenoemde 'multi-junction' zonnecellen. Hierin worden meerdere zonnecellen, elk van een ander halfgeleider materiaal met een verschillende bandgap, op elkaar gestapeld. Elk van die zonnecellen kan dan een klein stukje van het zonnespectrum zo efficiënt mogelijk omzetten naar elektriciteit. De tweede optie is het zonnespectrum aanpassen (of in andere woorden: de kleur veranderen) voor het wordt gebruikt door de zonnecel. Om dit te bereiken zijn we op zoek gegaan naar "Foton Managers".

Gezocht: Foton Managers (m/v)

Meer dan 90% van de zonnecellen die nu worden toegepast is gemaakt van silicium. In dit halfgeleidermateriaal kan de bandgap tussen de valentie- en de geleidingsband overbrugd worden met de energie van een foton van 1100 nm. Het grootste deel van de energie in het zonnespectrum bestaat uit fotonen met golflengtes tussen de 400 en 2400 nm (Figuur 1.2). Zoals al eerder genoemd hebben silicium zonnecellen een efficiëntie van ongeveer 15%, vooral door de transmissie- en thermalisatie-verliezen. Het transmissie verlies kan worden verminderd door de energie van *twee* fotonen (waarvan de energie te klein was om de bandgap te overbruggen) op te tellen, om zo *één* foton te krijgen met een grotere energie. Er kunnen bijvoorbeeld 2 fotonen met een golflengte van 2000 nm opgeteld worden om 1 foton te krijgen met een golflengte van 1000 nm. Fotonen met een golflengte van 2000 nm kunnen niet gebruikt worden in een zonnecel en leveren dus geen stroom op, terwijl een foton van 1000 nm wel gebruikt kan worden. Het 'optellen' van fotonen noemen we **upconversie**, en hiermee kan in theorie 35% meer energie van het zonnespectrum gebruikt worden door de zonnecel.

Dan zijn er nog de verliezen door fotonen met een energie groter dan de bandgap, de thermalisatieverliezen. Een foton met een golflengte van 500 nm kan door de zonnecel gebruikt worden om één elektron naar de geleidingsband te brengen, de rest van de energie gaat verloren als warmte. Wanneer dit foton wordt 'geknipt' in twee

fotonen van 1000 nm, kunnen beide fotonen gebruikt worden om een elektron naar de geleidingsband te brengen. Er kan nu dus twee keer zoveel stroom gemaakt worden voor dezelfde hoeveelheid energie. Het 'knippen' van fotonen zodat fotonen met een kleinere energie worden verkregen wordt **downconversie** of **kwantumknippen** genoemd. In theorie kan door downconversie 32% meer energie van het zonnespectrum gebruikt worden door de zonnecel.

Om de efficiëntie van zonnecellen groter te maken, hebben we onderzoek gedaan naar stoffen die efficiënt fotonen kunnen knippen. Materialen uit een groep elementen helemaal onderin het Periodiek Systeem, de **lanthaniden**, zijn goede kandidaten voor de functie van "Foton Manager". Ze hebben veel aangeslagen toestanden in het zichtbare en infrarode deel van het spectrum. Eén van de lanthaniden, **Ytterbium**, heeft maar één aangeslagen toestand. Het energieverschil tussen de grondtoestand en aangeslagen toestand van Ytterbium komt goed overeen met de bandgap van de silicium zonnecel. Dit maakt Ytterbium heel geschikt om pakketjes energie van andere lanthaniden te accepteren (we noemen Ytterbium dan ook wel de **acceptor**), en vervolgens als licht met de juiste golflengte (voor de zonnecel) uit te zenden. Ytterbium wordt in dit onderzoek telkens gecombineerd met een ander lanthanide-ion, dat fotonen met een grote energie kan absorberen en die energie in delen aan Ytterbium kan geven (dit wordt de **donor** genoemd). Om ervoor te zorgen dat de donor- en acceptorionen netjes bij elkaar in de buurt zitten, stoppen we ze samen in een kristallijne stof. In een kristal zijn alle atomen netjes geordend volgens een vast patroon, zoals bijvoorbeeld de bakstenen in een gemetselde muur.

Het onderwerp van dit proefschrift is onderzoek naar paren van lanthanide ionen (waarvan er een telkens Ytterbium is) die samen fotonen kunnen knippen. In hoofdstuk 1 wordt een inleiding gegeven en wordt de theorie van up- en downconversie met lanthaniden beschreven.

In hoofdstuk 2 en 3 zijn experimenten beschreven met het **Praseodymium** en **Ytterbium** paar. Wanneer Praseodymium een foton van ongeveer 440 nm absorbeert, geeft het die energie in twee stappen aan twee Ytterbium die zich vlakbij het Praseodymium bevinden. Dan kunnen beide Ytterbium-ionen een foton van ongeveer 1000 nm uitzenden. De lanthaniden zijn in hoofdstuk 2 in een rooster (strontiumfluoride) gestopt waarin ze graag groepjes vormen. Daardoor zullen de lanthaniden vrij dicht bij elkaar zitten. In deze stof is de efficiëntie van het knippen dan ook vrij hoog, namelijk zo'n 200% (elk foton met hoge energie wordt in tweeën geknipt). Helaas is de efficiëntie voor fotonen die ook weer worden uitgezonden, door verliezen, lager: ongeveer 140%. In hoofdstuk 3 zijn dezelfde twee lanthaniden in een ander rooster (yttriumfluoride) gestopt waarin ze willekeurig verdeeld zijn. De lanthaniden zitten dan verder van elkaar af, zodat de uiteindelijke efficiëntie veel lager is.

Een probleem is dat voor het effieciënt knippen van fotonen de Ytterbium concentratie hoog moet zijn zodat ieder Praseodymium-ion twee Ytterbium acceptoren in de buurt heeft. Bij een hoge Ytterbium concentratie treden echter ook verliezen op door een verschijnsel dat **concentratiedoving** genoemd wordt. De energie kan dan van Ytterbium naar Ytterbium worden overgedragen en als de rondlopende energie een defect in het rooster bereikt, gaat de energie verloren.

De volgende twee hoofdstukken (hoofdstuk 4 en 5) gaan over een ander paar lanthaniden, **Erbium** en **Ytterbium**, ingebouwd in verschillende kristallijne roosters. Helaas gaat het knippen bij dit paar in twee van de roosters (natriumyttriumfluoride en kaliumloodchloride) niet zo goed. Dit komt omdat Erbium veel aangeslagen toestanden heeft, die dicht op elkaar liggen. Daardoor is het heel makkelijk om de energie die door Erbium word geabsorbeerd weer te verliezen als warmte. Dit kan voorkomen worden door het Erbium, Ytterbium paar in te bouwen in een rooster met een lage vibratie-energie. In zo'n rooster (cesiumcadmiumbromide) bleek kwantumknippen inderdaad mogenlijk te zijn, maar de efficiëntie is lastig te bepalen.

In hoofdstuk 6 worden experimenten beschreven met **Neodymium** en **Ytterbium** in yttriumfluoride en cesiumcadmiumbromide. Net als bij Erbium en Ytterbium kan er geen downconversie plaatsvinden met Neodymium en Ytterbium in het fluoride rooster, omdat de geabsorbeerde energie deels verloren gaat voordat downconversie kan plaatsvinden. In het bromide kunnen Neodymium en Ytterbium wel heel efficiënt zichtbare fotonen knippen, om twee infrarode fotonen te krijgen.

In het zevende en laatste hoofdstuk staan korte experimenten beschreven met **Holmium** en **Ytterbium**. Holmium geeft heel efficiënt energie door aan Ytterbium, maar de uiteindelijke efficiëntie (de hoeveelheid fotonen die weer door Ytterbium worden uitgestraald) is laag.

Het onderzoek heeft aangetoond dat met behulp van paren van lanthanide-ionen fotonen van zichtbaar licht kunnen worden geknipt, zodat er voor elk blauw/groen foton twee fotonen infrarood verkregen worden. Door te kijken naar downconversie met 4 verschillende paren van lanthanide ionen in verschillende roosters hebben we veel geleerd over de mogelijkheden van het knippen van fotonen. We weten welke paren de beste kandidaten zijn als "Foton Manager", en met wat voor type roosters deze het beste gecombineerd kunnen worden. Met deze informatie kan verder worden gewerkt aan het vinden van het beste materiaal om het zonnespectrum aan te passen aan de zonnecel, om zo uiteindelijk efficiëntere zonnecellen te kunnen maken.

Publications

This thesis is based on the following publications:

- *Near-Infrared Quantum Cutting for Photovoltaics*, Bryan M. van der Ende, Linda Aarts and Andries Meijerink, Advanced Materials, **21**, 3073 (2009). *Chapter 2*
- *Downconversion for solar cells in $NaYF_4$:Er, Yb*, Linda Aarts, Bryan M. van der Ende and Andries Meijerink, Journal of Applied Physics, **106**, 023522 (2009). *Chapter 4*
- *Lanthanide Ions as Spectral Converters for Solar Cells*, Bryan M. van der Ende, Linda Aarts and Andries Meijerink, Physical Chemistry Chemical Physics, 2009, DOI:10.1039/B913877C. *Chapter 1, in press*
- *Downconversion for solar cells in YF_3:Nd^{3+}, Yb^{3+}*, Linda Aarts, Janne-Mieke Meijer, Bryan M. van der Ende and Andries Meijerink, *Chapter 6, submitted*
- *Downconversion for solar cells in YF_3:Pr^{3+},Yb^{3+}*, Linda Aarts, Bryan M. van der Ende and Andries Meijerink, *Chapter 3, submitted*
- *Downconversion for the Er^{3+}, Yb^{3+} couple in KPb_2Cl_5, a low-phonon frequency host*, Linda Aarts, Sander Jaeqx, Bryan M. van der Ende and Andries Meijerink, *Chapter 5, submitted*

Dankwoord

De afgelopen jaren heb ik met plezier veel van mijn tijd doorgebracht op de eerste verdieping van het Ornstein Laboratorium. In dit proefschrift is mijn onderzoek beschreven, waar een aantal mensen direct, en anderen indirect aan hebben bijgedragen. Daarvoor wil ik ze graag op deze plek bedanken.

Als eerste wil ik mijn promotor, Andries Meijerink, bedanken voor zijn begeleiding de afgelopen vier jaar. Zijn bereidheid om mee te kijken deed me goed en zijn enthousiasme maakte me blijer met wat ik had gedaan. Ik wil hem ook bedanken voor zijn stimulans om, waar mogelijk, conferenties, bijeenkomsten en cursussen bij te wonen om zo mezelf verder te ontwikkelen.

Het grootste deel van de afgelopen jaren heb ik met veel plezier samengewerkt met Bryan. We hebben een aantal mooie posters gemaakt en gepresenteerd, onder andere in Veldhoven en Lunteren. Verder hebben we samen met Alek een goede week gehad op de conferentie in Lyon (al waren jullie soms niet echt “een postduif”).

Tijdens het meten komt het natuurlijk voor dat de dingen niet helemaal gaan zoals je graag zou willen. Niet alleen Andries en Bryan kwamen vaak helpen, maar ook Celso was altijd bereid om mee te kijken, ook al had hij het druk. Ik was er altijd blij mee als Celso kwam kijken wat er mis was, meestal betekende het dat het probleem dan opgelost werd. (Ik vind het nog steeds knap dat hem dat hij een vol vat stikstof op 3 van de 4 wieltjes naar boven kreeg, zodat wij weer verder konden meten.)

Wanneer iets gerepareerd of vervangen moest worden, of als we iets moesten bestellen was Hans onmisbaar. Hij kon alles repareren, maar ook zijn gezelligheid heeft er aan bijgedragen dat ik me altijd thuis heb gevoeld op de vakgroep. Ik heb met veel plezier samen het chemisch afval weggebracht, chemicaliën gehaald of gewoon een kopje koffie of thee gedronken. Het was ook erg prettig dat Stephan er was als een computer niet helemaal deed wat ik wilde of als ik advies nodig had over welk programma ik het beste kon gebruiken, en hij was er tijdens de koffiepauzes altijd bij. Nico en Dick wil ik graag bedanken voor het verzorgen van de cryogene vloeistoffen.

In de afgelopen 4 jaar heb ik twee bachelor- en twee masterstudenten mogen begeleiden: Arno, Loes, Janne-Mieke en Sander. Het was een plezier om met jullie samen te werken. Ik vond het leuk om te zien hoe jullie steeds zelfstandiger gingen werken, en uiteindelijk mooie verslagen hebben gemaakt. Een deel van de resultaten is terug te vinden in de voorgaande hoofdstukken, en op basis van het werk van Sander en Janne-Mieke hebben we 2 mooie artikelen kunnen schrijven.

Verder wil ik alle vroegere en huidige collega's en studenten van het CMI bedanken. Van koffiepauzes met pepernoten of paaseitjes tot de Debye sportdag, van een barbecue in de tuin van John tot bowlen, de sfeer was altijd goed. Ik vond het leuk om van gedachten te kunnen wisselen met mensen die net een andere insteek hebben. Een 'domme' vraag kan je soms net op een idee brengen waar je eerder nog niet aan dacht.

Ik wil FOM en het Joint Solar Program (JSP) bedanken voor de financiering van dit onderzoek. De halfjaarlijkse bijeenkomsten waren elke keer weer interessant. De presentaties van de andere JSP onderzoekers waren leuk om te zien.

Dan wil ik nog mijn familie en vrienden bedanken. In het bijzonder mijn vader, moeder en Geertje, mijn zusje Rieneke en broertje Wouter, voor hun belangstelling, en waar nodig afleiding. Als laatste wil ik graag Paul bedanken voor alles. Je hebt me vaak geholpen met praktische zaken, maar het belangrijkste is dat je mijn "rotsje" bent.

In andere woorden:

"Een proefschrift maak je niet alleen."

Curriculum Vitae

The author of this thesis was born on September 16th 1982 in Leiden, The Netherlands. On June 16th 2000 she received her VWO diploma from the Christelijk Gymnasium Utrecht and in September of that year she started her study in Chemistry at Utrecht University. She received her B.Sc. degree in December 2004. During 2003 and 2004 she tutored high school students in Chemistry, Physics and Math at Stuva Studiehuis in Woerden. The research for her Master Thesis was done in the Condensed Matter and Interfaces group at Utrecht University, under the supervision of prof. dr. John Kelly and drs. Floris van Driel. Her internship took place in the Biosensor-project at Philips Research in Eindhoven. In september 2005 she received her M.Sc. degree.

From November 1st 2005 she was employed as a PhD student in the Condensed Matter and Interfaces group of the Debye Institute for Nanomaterials Science at Utrecht University, under the supervision of prof. dr. Andries Meijerink. The research project 'Photon Management for Solar Cells' was part of the Joint Solar Programme, which was co-funded by FOM and Shell. The results of her PhD-project are described in this thesis and were published in scientific journals and presented as posters or oral presentations at several national and international conferences.

Besides her research tasks she supervised two Bachelor and two Master students, assisted in a practical course on Analytical Chemistry and assisted during exercise classes for the first-year Spectroscopy course. She also supervised many first-year students during a three-week research project. Since the start of her studies she has participated in outreach activities like the 'Open Days' of Utrecht University, acting as a guide or giving workshops for potential students.